

**LIBRARY
Michigan State
University**

This is to certify that the
dissertation entitled

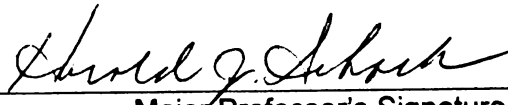
**FLOW MEASUREMENTS AND IN-CYLINDER COMBUSTION
DIAGNOSIS IN AN INTERNAL COMBUSTION ENGINE
ASSEMBLY**

presented by

Mayank Mittal

has been accepted towards fulfillment
of the requirements for the

Doctoral degree in Mechanical Engineering



Major Professor's Signature

12/3/09

Date

PLACE IN RETURN BOX to remove this checkout from your record.
TO AVOID FINES return on or before date due.
MAY BE RECALLED with earlier due date if requested.

DATE DUE	DATE DUE	DATE DUE

**FLOW MEASUREMENTS AND IN-CYLINDER COMBUSTION
DIAGNOSIS IN AN INTERNAL COMBUSTION ENGINE
ASSEMBLY**

By

Mayank Mittal

A DISSERTATION

**Submitted to
Michigan State University
in partial fulfillment of the requirements
for the degree of**

DOCTOR OF PHILOSOPHY

Mechanical Engineering

2009

ABSTRACT

FLOW MEASUREMENTS AND IN-CYLINDER COMBUSTION DIAGNOSIS IN AN INTERNAL COMBUSTION ENGINE ASSEMBLY

By

Mayank Mittal

The flow fields inside the engine cylinder are extremely complex and exhibit large cycle-to-cycle variations. It is the most important factor that controls the combustion process. It governs the fuel-air mixing and burning rates inside the engine cylinder. Therefore, it is desirable to improve the measurement techniques for velocity measurements and scalar properties pertaining to the in-cylinder flows. In this dissertation, molecular tagging velocimetry (MTV) is used to obtain the multiple point measurement of the instantaneous velocity field inside the engine cylinder. MTV is a molecular counterpart of particle-based techniques, and it eliminates the use of seed particles.

In the first part of this work, an experimental study is performed to investigate the effects of charge motion control on in-cylinder flow (using MTV). It is found that the charge motion control has a profound effect on cycle-to-cycle variations during the intake and early compression; however, its influence reduces during the late compression. In-cylinder engine flow measurements are extended to obtain an instantaneous three-component velocity field using stereoscopic molecular tagging velocimetry (SMTV). The image-processing technique, implemented to obtain the three-components of velocity, involves two major steps: (i) calibration process and (ii) data acquisition and reduction. Preliminary results show that the cycle-to-cycle variations are more prominent in the

velocity component perpendicular to the tumble plane, as opposed to the in-plane components. Such new insights will help better understand the details of these flows and further improve CFD models for IC engines.

Experimental measurements provide useful information of the flow fields inside the engine cylinder. However, it is multi-dimensional numerical simulations that offer the potential of significant time and cost savings to design the engine with improved performance. To date, numerical simulations of in-cylinder flows are performed with assumed boundary conditions. Due to this, flow measurements are performed inside the intake manifold of an engine assembly that can provide real-time boundary conditions for more accurate multi-dimensional numerical simulations. The geometry of the intake manifold is simplified for this purpose. A hot-wire anemometer and piezoresistive type absolute pressure transducers are used to measure the velocity and pressure, respectively. In-cylinder flow measurements are also performed (using SMTV) to validate the modeling efforts.

In the second part of this work, in-cylinder combustion diagnosis is performed inside an ethanol-gasoline, dual fueled, single-cylinder spark ignition engine. A dual fuel injection system with both direct-injection (DI) and port-fuel-injection (PFI) is used. The cycle-to-cycle variability is presented using the coefficient of variation of indicated mean effective pressure. Mass fraction burned and burn duration are determined from the analysis of measured in-cylinder pressure data.

To my parents for their unconditional love and support,
to Kanu, the great companion of my life,
and to Mridu, my magnificent daughter.

ACKNOWLEDGEMENTS

First, I would like to thank my advisor, Dr. Harold Schock, for giving me the opportunity to work at the Automotive Research Experiment Station (ARES). It has been an enormous experience working under his supervision, which enabled me to think independently and helped me to rise to the high standards of research. I thank him for providing the financial support during my graduate studies at Michigan State University.

I thank my thesis committee members, Dr. Manoochehr Koochesfahani, Dr. Farhad Jaber and Dr. Tim Hogan for their time to review my manuscript and make valuable suggestions.

I am grateful to Dr. Reza Sadr, who advised me from the early stages of my research on molecular tagging velocimetry. He also helped me to understand the concepts of stereoscopic molecular tagging velocimetry and to develop various image processing algorithms. I extend my thanks to Amir Naqwi for his valuable insights in calibration process. This work would have not been possible without their valuable inputs. I am thankful to Dr. Ahmed Naguib, who made the hot wire available for the velocity measurements inside the intake manifold of the engine assembly. I would also like to thank Dr. Guoming Zhu and Dr. David Hung for the discussions on combustion diagnosis.

I thank my colleagues at ARES, for sharing their valuable time and helping me with their valuable suggestions. I would like to specially thank Andrew Fedewa and Tom Stuecken for their help in experiments. I thank Jeff and Gary for understanding me and providing the necessary help when required.

Finally, special thanks to my family. I would sincerely like to thank my parents for the good things they taught me during my childhood, their unconditional love and support throughout my life. Also, none of this would have been possible without the love, patience and continual encouragement of my wife. She was always with me during the stressful times.

TABLE OF CONTENTS

LIST OF TABLES	ix
LIST OF FIGURES	x
LIST OF SYMBOLS	xv
LIST OF ABBREVIATIONS	xvi
1. Introduction	1
1.1. Background	1
1.2. Literature review	3
1.2.1. Pre-combustion analysis	3
1.2.2. Combustion analysis	13
1.3. Contents of the Present Work	15
2. A study of cycle-to-cycle variations on in-cylinder flow in an IC engine equipped with CMCV using MTV	18
2.1. Introduction	18
2.2. Experimental setup and procedure	20
2.2.1. Experimental setup	20
2.2.2. Charge motion control valve	26
2.2.3. Molecular tagging procedure	26
2.3. Experimental Results	31
2.3.1. Swirl measurement plane, 1500 rpm	31
2.3.2. Swirl measurement plane, 2500 rpm	42
2.3.3. Tumble measurement plane, 1500 rpm	46
2.3.4. Tumble measurement plane, 2500 rpm	49
2.4. Summary	52
3. In-cylinder flow measurement using stereoscopic molecular tagging velocimetry ..	55
3.1. Introduction	55
3.2. Experimental setup	57
3.3. Measurement Procedure	61
3.4. Experimental Results	70
3.4.1. Flow field at 90 CAD	70
3.4.2. Flow field at 180 CAD	73
3.4.3. Flow field at 270 CAD	75
3.5. Summary	77
4. Intake manifold and in-cylinder flow measurements inside an IC engine assembly ..	79
4.1. Introduction	79
4.2. Experimental setup	81

4.3. Experimental Results	88
4.3.1. Flow measurements at 900 rpm engine speed	89
4.3.2. Flow measurements at 1200 rpm engine speed	100
4.4. Summary	105
5. In-cylinder combustion diagnosis in an ethanol-gasoline, dual-fueled, spark ignition engine	106
5.1. Introduction	106
5.2. Experimental setup	109
5.3. Measurement Procedure	111
5.3.1. Mass fraction burned analysis	112
5.3.1.1. Model 1, Rassweiler and Withrow method	112
5.3.1.2. Model 2, Net Pressure method	115
5.4. Experimental Results	116
5.4.1. PFI-E85 and DI-Gasoline system	117
5.4.2. DI-E85 and PFI-Gasoline system	121
5.4.3. PFI-Gasoline and DI-Gasoline system	124
5.5. Improving the MFB calculation using net pressure method	126
5.6. Summary	129
6. Final remarks	132
7. References	135

LIST OF TABLES

Table 2.1: Engine specifications	22
Table 2.2: Properties of biacetyl	28
Table 5.1: Properties of ethanol and gasoline	107
Table 5.2: Test matrix	110

LIST OF FIGURES

Figure 2.1: Optical engine assembly	21
Figure 2.2: Intake and exhaust valves lift	22
Figure 2.3: Tumble and swirl measurement planes inside the IC engine cylinder	23
Figure 2.4: Schematic of MTV optical setup for in-cylinder flow measurement	24
Figure 2.5: Front view of LPX205i	25
Figure 2.6: Rear view of LPX205i	25
Figure 2.7: Charge motion control valve; (a) deactivated, and (b) activated	26
Figure 2.8: Absorption spectrum for biacetyl	28
Figure 2.9: Phosphorescence emission spectrum for biacetyl at four different excitation wavelengths	29
Figure 2.10: Undelayed (left) and delayed (right) images for tumble measurement plane at 138 crank angle degree	30
Figure 2.11: Ensemble-averaged velocity vectors, contours of velocity rms for deactivated (left) and activated (right) CMCV at (a) 121 (top), and (b) 300 (bottom) CADs; swirl measurement plane at 1500 rpm	33
Figure 2.12: Ensemble-averaged velocity vectors with activated CMCV at 121 CAD considering (a) 1-100, (b) 101-200, and (b) 1-500 consecutive undelayed frames; swirl measurement plane at 1500 rpm	34
Figure 2.13: Instantaneous velocity fields from consecutive engine cycles 99 ^a , 100 ^b and 101 ^c , and ensemble-averaged velocity field ^d with activated CMCV at 121 CAD; swirl measurement plane at 1500 rpm	36
Figure 2.14: Instantaneous velocity field ^a and mean subtracted flow field ^b for 101st cycle at 121 CAD with activated CMCV; swirl measurement plane at 1500 rpm	37
Figure 2.15: PDFs of normalized circulation at different CADs for swirl measurement plane with CMCV deactivated at 1500 rpm engine speed	39
Figure 2.16: PDFs of normalized circulation at different CADs for swirl measurement plane with CMCV activated at 1500 rpm engine speed	40

Figure 2.17: Standard deviation of normalized circulation and turbulent kinetic energy at different CADs for swirl measurement plane at 1500 rpm engine speed	42
Figure 2.18: Ensemble-averaged velocity vectors, contours of velocity rms for deactivated (left) and activated (right) CMCV at (a) 171 (top), and (b) 221 (bottom) CADs; swirl measurement plane at 2500 rpm engine speed	44
Figure 2.19: PDFs of normalized circulation at different CADs for swirl measurement plane with CMCV deactivated at 2500 rpm engine speed	45
Figure 2.20: PDFs of normalized circulation at different CADs for swirl measurement plane with CMCV activated at 2500 rpm engine speed	45
Figure 2.21: Standard deviation of normalized circulation and turbulent kinetic energy at different CADs for swirl measurement plane at 2500 rpm engine speed	46
Figure 2.22: PDFs of normalized circulation at different CADs for tumble measurement plane with CMCV deactivated at 1500 rpm engine speed	47
Figure 2.23: PDFs of normalized circulation at different CADs for tumble measurement plane with CMCV activated at 1500 rpm engine speed	48
Figure 2.24: Standard deviation of normalized circulation and turbulent kinetic energy at different CADs for tumble measurement plane at 1500 rpm engine speed	49
Figure 2.25: PDFs of normalized circulation at different CADs for tumble measurement plane with CMCV deactivated at 2500 rpm engine speed	50
Figure 2.26: PDFs of normalized circulation at different CADs for tumble measurement plane with CMCV activated at 2500 rpm engine speed	51
Figure 2.27: Standard deviation of normalized circulation and turbulent kinetic energy at different CADs for tumble measurement plane at 2500 rpm engine speed	52
Figure 3.1: Basic configuration of lens translation method for stereoscopic imaging	57
Figure 3.2: Basic configuration of angular displacement method for stereoscopic imaging	57
Figure 3.3: Tumble measurement plane inside an IC engine cylinder	59
Figure 3.4: Schematic of SMTV optical setup	60
Figure 3.5: Calibration Target	62

Figure 3.6: Undelayed (left) and delayed (right) images at 90 CAD SMTV measurements for right camera, time delay (Δt) = 10 μ s	65
Figure 3.7: Ensemble-averaged velocity (left) and out-of-plane mean vorticity (right) at 90 CAD	71
Figure 3.8: RMS of u , v and w velocity components at 90 CAD	73
Figure 3.9: Ensemble-averaged velocity (left) and out-of-plane mean vorticity (right) at 180 CAD	74
Figure 3.10: RMS of u , v and w velocity components at 180 CAD	75
Figure 3.11: Ensemble-averaged velocity and out-of-plane mean vorticity at 270 CAD	76
Figure 3.12: RMS of u , v and w velocity components at 270 CAD	76
Figure 4.1: Experimental rig showing measurement planes and locations inside the intake manifold for flow measurements	82
Figure 4.2: Intake port geometry	82
Figure 4.3: Combustion analysis system (CAS) used for intake manifold flow measurement	85
Figure 4.4: Experimental rig for in-cylinder flow measurement using stereo MTV	86
Figure 4.5: Tumble measurement plane inside the engine cylinder	86
Figure 4.6: Schematic of SMTV optical setup	88
Figure 4.7: Averaged in-cylinder pressure trace at 900 rpm engine speed	89
Figure 4.8: Averaged pressure trace at the circular section of the intake manifold at 900 rpm engine speed	90
Figure 4.9: Averaged velocity profile at different radial locations in the circular section of the intake manifold at 900 rpm engine speed	91
Figure 4.10: Intake valve lift and its first derivative	92
Figure 4.11: Averaged velocity at different radial locations 2 (0 mm), 3 (3 mm), 4 (21 mm), 5 (24 mm) and at the wall (26 mm) during the intake stroke at various crank angle degrees; 900 rpm engine speed	92

Figure 4.12: Averaged pressure trace at the circular and elliptical sections of the intake manifold at 900 rpm engine speed	93
Figure 4.13: Calibration images of left (left) and right (right) cameras	95
Figure 4.14: Undelayed (left) and delayed (right) images at 120 crank angle degree for left (upper) and right (lower) cameras at 900 rpm engine speed	96
Figure 4.15: Ensemble-averaged velocity filed (left) and velocity rms (right) at 120 crank angle degree and 900 rpm engine speed	97
Figure 4.16: Ensemble-averaged velocity filed (left) and velocity rms (right) at 140 crank angle degree and 900 rpm engine speed	98
Figure 4.17: Ensemble-averaged velocity filed (left) and velocity rms (right) at 260 crank angle degree and 900 rpm engine speed	99
Figure 4.18: Ensemble-averaged velocity filed (left) and velocity rms (right) at 280 crank angle degree and 900 rpm engine speed	100
Figure 4.19: Averaged in-cylinder pressure trace at 1200 rpm engine speed	101
Figure 4.20: Averaged pressure trace at the circular and elliptical sections of the intake manifold at 1200 rpm engine speed	101
Figure 4.21: Averaged velocity profile at different radial locations in circular section of the intake manifold at 1200 rpm engine speed	103
Figure 4.22: Ensemble-averaged velocity filed (left) and velocity rms (right) at 170 crank angle degree and 1200 rpm engine speed	103
Figure 4.23: Ensemble-averaged velocity filed (left) and velocity rms (right) at 210 crank angle degree and 1200 rpm engine speed	104
Figure 5.1: Experimental rig	111
Figure 5.2: Measured pressure data, Test C2 (PFI-gasoline 100 %)	114
Figure 5.3: Indicator diagram in logarithmic scales, Test C2 (PFI-gasoline 100 %)	115
Figure 5.4: Mean IMEP (top) and COV_{imep} (bottom) for PFI-E85 and DI-gasoline, and DI-E85 and PFI-gasoline systems	117
Figure 5.5: Averaged Pressure (top) and MFB curves (bottom) for PFI-E85 and DI-gasoline system at 3.3 bar IMEP and 1500 rpm	119

Figure 5.6: Averaged Pressure (top) and MFB curves (bottom) for PFI-E85 and DI-gasoline system at WOT and 1500 rpm120

Figure 5.7: Averaged Pressure (top) and MFB curves (bottom) for PFI-E85 and DI-gasoline system at WOT and 2500 rpm121

Figure 5.8: Averaged Pressure (top) and MFB curves (bottom) for DI-E85 and PFI-gasoline system at 3.3 bar IMEP and 1500 rpm123

Figure 5.9: Averaged Pressure (top) and MFB curves (bottom) for DI-E85 and PFI-gasoline system at WOT and 1500 rpm124

Figure 5.10: Averaged Pressure (top) and MFB curves (bottom) for PFI and DI-gasoline system at 3.3 bar IMEP and 1500 rpm125

Figure 5.11: Averaged Pressure (top) and MFB curves (bottom) for PFI and DI-gasoline system at WOT and 1500 rpm126

Figure 5.12: MFBs for PFI-gasoline and DI-gasoline system at 3.3 bar IMEP (top) and WOT (bottom)129

LIST OF SYMBOLS

Δt	Time delay
F	Mapping function
ϕ	Fuel-to-air equivalence ratio
k	Turbulent kinetic energy
λ	Air-to-fuel ratio
λ	Wavelength
n	Polytropic index
n_c	Polytropic index of compression
n_e	Polytropic index of expansion
ω	Vorticity
p	In-cylinder pressure
S_p	Mean piston speed
σ	Standard deviation
u, v, w	x, y and z components of velocity
u', v', w'	x, y and z components of fluctuating velocity
$\langle u \rangle, \langle v \rangle, \langle w \rangle$	Ensemble averaged of u, v and w velocity components
V	In-cylinder volume
V_d	Displaced in-cylinder volume
x, y, z	Cartesian coordinates in physical space
X, Y	Cartesian coordinates in image plane

LIST OF ABBREVIATIONS

BDC	Bottom dead center
CAD	Crank angle degree
CAS	Combustion analysis system
CCD	Charge coupled device
CFD	Computational fluid dynamics
CI	Compression-ignition
CMCV	Charge motion control valve
CO	Carbon monoxide
COV	Coefficient of variation
DI	Direct-injection
E85	Blend of 85% ethanol and 15% gasoline by volume
EOC	End of combustion
HWA	Hot-wire anemometry
IC	Internal combustion
IMEP	Indicated mean effective pressure
LDV	Laser doppler velocimetry
MFB	Mass fraction burned
MON	Motor octane number
MPP	Measurement plane pointers
MTV	Molecular tagging velocimetry

NC	Normalized circulation
NO _x	Nitrogen oxides
PDF	Probability density function
PFI	Port-fuel-injection
PIV	Particle image velocimetry
RMS	Root-mean-square
RON	Research octane number
RPM	Revolutions per minute
SCV	Swirl control valve
SI	Spark-ignition
SMTV	Stereoscopic molecular tagging velocimetry
SOC	Start of combustion
SPIV	Stereoscopic particle image velocimetry
TDC	Top dead center
TKE	Turbulent kinetic energy
UV	Ultraviolet
VCT	Variable camshaft timing
WOT	Wide open throttle

CHAPTER-1

INTRODUCTION

1.1 Background

Internal combustion (IC) engines, both spark-ignition (SI) and compression-ignition (CI) types, are distinct from most other power producing and propulsion systems in an important way. The working fluid undergoes the processes essential for the production of power—compression, fuel energy release by combustion, and expansion—within a single chamber, known as the engine's cylinder (Heywood¹, 1987). The majority of internal combustion engines operate on the four-stroke cycle. Each engine cylinder requires these four strokes of its piston—two revolutions of the crank shaft—to complete the sequence of events that produces one power stroke. These four strokes are composed of intake stroke, compression stroke, power stroke, and exhaust stroke:

1. The intake stroke starts with the piston at top dead center (TDC) and ends with the piston at bottom dead center (BDC). During the intake stroke, a fresh mixture is induced into the cylinder through the intake valve(s). The intake valve(s) opens shortly before the stroke starts and closes after it ends to increase the mass inducted.
2. During the compression stroke, both the intake and exhaust valves are closed and the mixture inside the cylinder is compressed by the piston. Combustion process is initiated towards the end of this stroke and the pressure inside the cylinder rises rapidly.

3. The power stroke starts with the piston at TDC and ends with the piston at BDC. During the power stroke, the high-temperature and high-pressure gases push the piston down to do the mechanical work. About five times as much work is done on the piston during the power stroke as the piston had to do during the compression stroke (Heywood², 1988).
4. The exhaust stroke starts with the piston at BDC and ends with the piston at TDC. The exhaust valve opens shortly before the power stroke ends (at BDC) and the burned gases exit the cylinder due to the piston motion towards TDC. The exhaust valve closes shortly after TDC and the cycle starts again.

To increase the work output of a four-stroke IC engine, with higher efficiency and lower emissions, each stroke should be well understood and optimized (Shen³, 2003). Each stroke in an operating engine cycle is affected by several factors. During the intake and compression strokes, the flow field inside the engine cylinder is highly turbulent and affected by several factors including compression ratio; engine speed and load; intake valve timing and lift; geometry of the intake manifold, intake valve and piston head; etc. During the power stroke, the combustion process is primarily affected by the flow field around the spark plug, air-to-fuel ratio, ignition timing, etc. The exhaust stroke is strongly affected by the burned gas motion, exhaust valve timing and lift, geometry of the exhaust manifold, etc.

In general, the flow field inside the engine cylinder is one of the most important factors that control the combustion process. The flame development inside the (SI) engine cylinder and its subsequent propagation vary significantly from cycle-to-cycle because it depends on local mixture composition and motion. Note that these quantities

vary in successive cycles and therefore affect the performance of an engine. A sufficiently turbulent flow field is required to ensure effective fuel-air mixing, rapid flame development and propagation during the combustion process. However, excessive mixture motion and turbulence, beyond that required to achieve the desired burning rate, is undesirable; it results in excessive heat losses to the combustion chamber walls (Heywood¹, 1987). Consequently, the understanding of cycle-to-cycle variation is needed to optimize them for improved engine performance. This requires continuous improvement in measurement techniques for the velocity field and scalar properties pertaining to in-cylinder flows and the methods for in-cylinder combustion diagnosis.

1.2 Literature review

Cycle-to-cycle variations exist in every stroke of an operating cycle of a four-stroke IC engine. Therefore, to optimize the cycle-to-cycle variations, each stroke of an operating cycle should be studied. Based on the time sequence of a four-stroke cycle, the analysis on the cycle-to-cycle variations in an IC engine can be classified into pre-combustion analysis (intake and compression strokes), combustion analysis (late compression and power strokes), and exhaust analysis (exhaust stroke). So far, most of the efforts to optimize the cycle-to-cycle variations have been focused on the pre-combustion and combustion analyses.

1.2.1 Pre-combustion analysis

Since the pre-combustion flow has a strong influence on both spark ignition and compression ignition engines, much insight into these flow fields has been gained using

various measurement techniques, i.e. hot-wire anemometry (HWA), laser doppler velocimetry (LDV), particle image velocimetry (PIV), molecular tagging velocimetry (MTV), etc. However, due to the variety of issues that are affected by in-cylinder flows and the difficult measurement environment, in-cylinder velocity measurement techniques and application details are often selected based on the kind of information required, Farrell⁴ (2007). Therefore, the literature involving in-cylinder velocity measurements is vast and is constantly being updated.

The earlier studies of in-cylinder flow measurements are performed using hot-wire anemometry, [5, 6, and 7]. Hassan and Dent⁵ (1971) used constant temperature HWA to measure the instantaneous gas velocity in a motored IC engine. Bahram et al.⁶ (1986) used HWA to study the effects of inlet configuration, flow rate, valve lift and cylinder bore diameter on the velocity distribution around the intake valve. Their results showed that the flow entering the engine cylinder is fully turbulent. However, the application of a hot-wire anemometer to measure the in-cylinder flow has several limitations, Witze⁷ (1980): (1) its response is strongly influenced by the properties of the fluid being measured. This is crucial for engine applications because of the highly transient nature of the gas pressure and temperature during the compression, (2) it cannot be used in a combusting environment, (3) it does not resolve the flow direction, and (4) it is intrusive, so that it can perturb the in-cylinder flow which is highly transient and three-dimensional. Witze⁷ (1980) mentioned that accurate in-cylinder hot-wire measurements are only possible for the intake and exhaust strokes.

Laser doppler velocimetry overcomes these difficulties and offers a significant advantage over HWA to measure the in-cylinder flows. In the 1980s, '90s, and even recently, laser doppler velocimetry has been used extensively for flow measurements at specific locations inside the engine cylinders [8-16]. Morse and Whitelaw⁸ (1981) presented LDV measurements inside a single-cylinder, four-stroke reciprocating engine. The authors masked the inlet valve over part of its periphery to promote swirl in the air flow during the intake stroke. The mean and root-mean-square (rms) profiles of the swirl velocity component were presented during the intake and compression strokes across the radial location at distances of 10 and 25 mm below the level of the cylinder head. Their results showed high levels of rms velocity fluctuations during the intake stroke; however, a continuous decrease in the levels of the rms fluctuations was reported during the compression stroke. Bicen et al.⁹ (1985) reported LDV measurements of air flow through the intake valve of a motored reciprocating engine. They concluded that the in-cylinder flow characteristics are strongly dependent on the piston interaction and flow unsteadiness. Hall and Bracco¹⁰ (1987) used LDV technique to evaluate the turbulence intensities under both motored and firing conditions in a ported homogeneous charge spark ignition engine. The authors used zirconium oxide seeding particles in their work with a nominal size of 1.5 μm . They found that TDC turbulence intensity was approximately linear with engine speed; however, it was relatively insensitive to the intake flow rate. Kent et al.¹¹ (1987) studied the effects of intake port design and valve lift on swirl and rms velocity fluctuations near TDC of compression using LDV. They concluded that depending on the port geometry, reduced valve lift may result in either

increased or decreased swirl. Their results showed that rms velocity fluctuation was relatively insensitive to the changes in valve lift. Fraser and Bracco¹² (1989) used LDV system in a motored, ported, single-cylinder IC engine to provide both an ensemble and a cycle-resolved analysis of integral length scales. Fluctuation integral length scale in their work was based on the spatial correlation coefficient of the fluctuation velocity (difference between the instantaneous velocity and the ensemble-averaged velocity at the same crank angle) where as turbulence integral length scale was based on the turbulence velocity (difference between the instantaneous velocity and the low-pass filtered velocity at the same crank angle and in the same cycle). Measurements were performed on the mid-plane of the TDC clearance height from 43 crank angle degrees before TDC to 20 crank angle degrees after TDC. Three compression ratios (5.7, 7.6, and 11.4) were considered, which correspond to the TDC clearance heights of 18.1, 12.8, and 8.2 mm, respectively. They found that the trends versus crank angle of the fluctuation length scales are generally different from those of the turbulence length scales. Lee et al.¹³ (1993) studied the effects of four different cylinder head intake port configurations and two piston geometries using a high speed flow visualization technique. Two-component LDV was used to compare the effects of piston geometry on the in-cylinder flow. Their results showed that cylinder head intake port configuration plays a significant role in the generation of initial tumble motion in the early stage of the intake stroke. Yoo et al.¹⁴ (1995) presented simultaneous three-component LDV measurements in a four-valve spark ignition engine. Their results confirmed that the flow field generated in the engine cylinder is complex, turbulent and three-dimensional. Hascher et al.¹⁵ (1997) conducted

three-component LDV measurement to calculate the turbulent kinetic energy (TKE) inside a single-cylinder of a 3.5 L four-valve engine. The TKE is defined by Equation 1.1.

$$k = \frac{1}{2} \left(\langle u'^2 \rangle + \langle v'^2 \rangle + \langle w'^2 \rangle \right) \quad (1.1)$$

The authors found higher levels of TKE where intake flows mix in high shear regions. Their results showed that the TKE decay exponentially with time. LDV measurements are very useful to generate detailed turbulence statistics due to their high temporal resolution, see Miles et al.¹⁶ (2003).

Although LDV data provide excellent temporal resolution, they are limited to a single point or along a line. It is desirable to take simultaneous measurements at multiple points, so properties such as vorticity and strain rate can be deduced easily. Therefore, developments in the more mature single-point systems, either hot-wire anemometry or laser doppler velocimetry, have been less rapid recently in IC engine applications, Farrell⁴ (2007). Particle image velocimetry has become the most widely used technique for velocity field measurements, as it can simultaneously measure two or three components of the velocity vectors at multiple points in a plane [17-27]. Li et al.¹⁹ (2001) used PIV to investigate the tumble and swirl motions in the cylinder of a four-valve SI engine. Tumble motion is defined as the organized rotation of the charge in the vertical plane of the cylinder. Similarly, swirl is the organized rotation about the cylinder axis. These are used to increase the turbulence intensity and hence to speedup the combustion process. A swirl ratio (SR) is normally used to define the swirl in an

operating engine (Heywood², 1988). It is defined as the angular velocity of a solid-body rotating flow, ω_s , which has equal angular momentum to the actual flow, divided by the crankshaft angular rotational speed, ω_c :

$$SR = \frac{\omega_s}{\omega_c} \quad (1.2)$$

Li et al.¹⁹ (2001) expressed the swirl (or tumble) ratio in a planar PIV vector field by

$$SR = \frac{\sum_{i=1}^N m_i \overline{r_i} \times \overline{u_i}}{I \omega_c} \quad (1.3)$$

where I is the angular inertia;

$$I = \sum_{i=1}^N m_i \overline{r_i} \cdot \overline{r_i},$$

$\overline{r_i}$ is the distance of the cell position of i^{th} velocity vector to the vortex center, and m_i is the mass of fluid located in the cell. The authors suggested that the fluid mass may be assumed to be distributed uniformly within the cylinder. Funk et al.²⁰ (2002) also studied the effects of low and high swirl in-cylinder flows using particle image velocimetry. Bevan and Ghandhi²¹ (2004) studied the effects of three intake port geometries on in-cylinder flows using two-component PIV measurements. They showed that in-cylinder flows generated by the three ports were highly complex and three-dimensional. Significant cycle-to-cycle variation was observed in the flow field. The

authors concluded that the orientation of the intake port also had a significant effect on the flow field. High frame rate measurements using particle image velocimetry in a motored engine have been demonstrated by Gandhi et al.²² (2005). Several studies have been reported to measure the in-cylinder cyclic variations using particle image velocimetry; see Towers and Towers²³ (2004), Jarvis et al.²⁴ (2006), Jarvis et al.²⁵ (2006). Recently, Stansfield et al.²⁶ (2007) performed PIV in-cylinder flow measurements over a range of realistic engine speeds, i.e 750, 2000, and 3500 rpm. Calendini et al.²⁷ (2000) reported the in-cylinder engine flow measurements using stereoscopic particle image velocimetry (SPIV).

Application of particle image velocimetry for in-cylinder measurements, however, has some limitations. The presence of particle tracers can cause complications due to their mechanical interference with the moving parts in the IC system. Moreover, the particle tracers may not truly represent the highly turbulent flow field. A molecular tagging approach overcomes these problems and offers an advantage over the particle-based techniques, i.e. particle image velocimetry. The technique nonintrusively maps fluid velocity simultaneously at multiple points over a plane, so properties like vorticity and strain rate can be deduced easily. It works by premixing the flowing medium with molecules having a long-lived luminescence lifetime. Use of molecules as tracers, as opposed to the seed particles, has the advantages of unbiased flow tracking and clean operation, i.e. elimination of the contamination of the engine cylinder by the tracer particles. In addition, MTV measurement of in-plane velocity vectors is quite insensitive to the out-of-plane velocity component. It is to be noticed that the performance and

accuracy of PIV measurement of in-plane velocity vectors may degrade in highly three-dimensional flows due to particle motion in/out of the plane of the laser sheet. Koochesfahani et al.²⁸ (1996) demonstrated this aspect in an application of MTV to the highly three-dimensional flow of a forced wake. Details of various MTV techniques are described previously in literature, for example by Gendrich and Koochesfahani²⁹ (1996), Hill and Klewicki³⁰ (1996), and Sadr and Klewicki³¹ (2003). Koochesfahani³² (1999) discussed different molecular tagging methods and its applications to various flow fields. Bohl et al.³³ (2001) reported the development of stereoscopic molecular tagging velocimetry for measurement of the three-component velocity field generated by a propeller. Koochesfahani and Nocera³⁴ (2001) discussed the details of various molecular complexes suitable for gas and liquid-phase flows in MTV measurements. In gas-phase applications the authors discussed the use of biacetyl's and acetone's phosphorescence. However, in liquid-phase flows water soluble compounds such as caged fluorescent molecules and phosphorescent supramolecules are widely used.

Although the emphasis of this dissertation is on gas-phase flows, it is worth noting liquid-phase developments. Earlier MTV investigations in liquid-phase flows have relied on photochromic molecules, which required experimentalists to use organic solvents such as kerosene as the flowing medium. As discussed by Gendrich et al.³⁵ (1997), in a photochromic process excitation by photons causes a change in the absorption spectrum and therefore a change in the color of the solution (e.g. from clear to dark blue). The color change can persist for several seconds to minutes, although the

tagging process occurs within nanoseconds. The photochromic process is reversible and therefore the chemical is reusable. The use of photochromic chemicals requires two photon sources: typically a pulsed UV source (e.g. $\lambda = 351$ nm from an excimer laser) to induce the color change and a white light source to interrogate the tagged regions. The most significant drawback in using photochromic chemicals is that the image is produced by a change in absorbance, thereby requiring a measurement of the difference between incident and transmitted light. Emitted light (against a black background) is more easily and accurately detected than transmitted light; consequently, images based on luminescence are better suited to MTV applications. The use of caged fluorescein and similar compounds was first reported by Lempert et al.³⁶ (1995). In this compound a chemical group is attached to fluorescein in order to render it non-fluorescent. The caging group is removed upon absorption of UV photons ($\lambda = 350$ nm), thereby creating regular fluorescein which fluoresces with a very high quantum efficiency. Here the long-lifetime tracer is the uncaged fluorescein, which persists for a very long time and can be interrogated at the time of interest through its luminescence upon re-irradiation. Two sources of photons are therefore needed, one to break the cage and the other to excite fluorescence. It is to be noticed that the cage-breaking process is irreversible, so each caged molecule can be tagged only once. The cage-breaking process is not rapid, occurring with a time constant on the order of a few milliseconds. Gendrich et al.³⁵ (1997) reported the development and application of more recent phosphorescent supramolecules. Phosphorescent compound when used for molecular tagging, excitation by photons produces a long-lived excited state which is interrogated through its phosphorescence emission as the molecule radiatively returns to its ground state. The

long-lifetime tracer is the excited-state molecule itself. In this case only one source of photons is needed; the tagging process occurs during the laser pulse; and the excitation/emission process is reversible, which means the chemicals are reusable. The difficulty is that the long-lived excited states suffer from O₂ and H₂O quenching. Lum et al.³⁷ (2001) used phosphorescent supramolecules in the measurements of small-scale flows. Koochesfahani et al.³⁸ (2000) combined MTV with laser induced fluorescence for simultaneous measurement of the velocity and concentration fields using phosphorescent supramolecules.

Stier and Koochesfahani³⁹ (1998) used the molecular tagging velocimetry technique to investigate the flow field inside a steady flow rig model of an IC engine. The geometry used by the authors is common to study the fundamental aspects of the intake flow. Goh⁴⁰ (2001) and Koochesfahani et al.⁴¹ (2004) showed the in-cylinder flow pattern during the late compression of a motored IC engine using two-component MTV.

The flow field inside an engine cylinder is highly transient in nature and exhibits large cycle-to-cycle variations. The high cycle-to-cycle variations affect the fuel-air mixing and therefore it can influence the engine performance. Consequently, the understanding of cycle-to-cycle variation is needed to optimize the engine design. Reuss¹⁸ (2000) introduced the probability density function to characterize the cyclic variations of in-cylinder flows. Towers and Towers²³ (2004), Schock et al.⁴² (2003), and Ismailov et al.⁴³ (2006) investigated the cycle-to-cycle variations inside the engine cylinder. It was found that probability density functions of the normalized circulation

calculated from instantaneous planar velocities are most suitable to characterize in-cylinder cycle-to-cycle variations.

Experimental measurements of in-cylinder flows (either MTV or PIV) provide useful information that can be used to validate the ongoing efforts in the development of multi-dimensional numerical simulations of in-cylinder flows. Note that experimental measurements are limited over a plane and do not provide detailed flow information over the complete volume of the engine cylinder. It is the multi-dimensional numerical simulations that provide this information, and offer the potential of significant time and cost savings to design the engine with improved performance. With the advent of powerful computers, several studies of in-cylinder flows have been reported using multi-dimensional numerical simulations, i.e. Luo et al.⁴⁴ (2003), Shojaeefard and Noorpoor⁴⁵ (2008). However, boundary conditions are assumed in the modeling efforts. Experimental information that can provide the real-time boundary conditions is necessary to perform more accurate multi-dimensional numerical simulations of complex in-cylinder flows.

1.2.2 Combustion analysis

The primary purpose of combustion in a piston engine is to generate the pressure for shifting the expansion process away from the compression process and produce the work cycle. In the analysis of combustion in piston engines, the principal components are considered as hydrocarbon fuel and air. They are first combined into a molecular aggregate, and then transformed by an exothermic reaction to form the products. The process of this exothermic reaction is conventionally referred to as “heat release”. In an internal combustion engine, this transformation is observed as a measurable cylinder

pressure rise manifesting the essential outcome of combustion. Thus, cylinder pressure is frequently utilized as a direct parameter to characterize the combustion process in IC engines; see Shen et al.⁴⁶ (2002), Shen et al.⁴⁷ (2003), and Oppenheim⁴⁸ (2004). Burgdorf and Denbratt⁴⁹ (1997) compared various knock detection methods based on in-cylinder pressure data. Mittal et al.⁵⁰ (2009) used recorded in-cylinder pressure data to study the effects of pre-injection on combustion characteristics of a single-cylinder diesel engine. One important measure of cycle-to-cycle variations, derived from in-cylinder pressure data, is the coefficient of variation (COV) in indicated mean effective pressure (IMEP), COV_{imep} ; Heywood² (1988). It defines the cyclic variability in terms of indicated work per cycle.

In-cylinder pressure is important not only for itself as a quantitative characteristic parameter, but also because some combustion-related parameters, such as mass fraction burned (MFB), can be determined from the recorded pressure data. Mass fraction burned shows how in-cylinder combustion progresses as a function of crank angle. It gives a direct indication of the quality of combustion and quantifies the cycle-to-cycle variations during the combustion process. Several methods have been suggested to evaluate the mass fraction burned in gasoline engines based upon the measured pressure data. The most popular method stems from the classical paper of Rassweiler and Withrow⁵¹ (1938). The authors reported that the percent of pressure rise due to combustion is approximately equal to the percent of charge burned (by weight) at the corresponding instants in the combustion period. Stone and Green-Armytage⁵² (1987) compared the two

methods; (i) two-zone combustion and (ii) Rassweiler and Withrow methods, to evaluate the mass fraction burned as a function of time in a spark ignition engine. Their results of the complex two-zone combustion model showed good agreement with a simpler model presented by Rassweiler and Withrow. Brunt and Emtage⁵³ (1997) compared the performance of five alternative MFB models using simulated and experimental data. They preferred the Rassweiler and Withrow model to produce the best results to determine the mass fraction burned in their comparative tests. Shayler et al.⁵⁴ (1990) investigated the best form to implement the Rassweiler and Withrow method and discussed the effect of uncertainty assumptions. They found that the end of combustion determination, the selection of polytropic index, and the effect of signal noise are important parameters for calculating the mass fraction burned using the Rassweiler and Withrow method.

1.3 Contents of the Present Work

In this dissertation, pre-combustion in-cylinder flow analysis is performed using the molecular tagging velocimetry technique in gas-phase flows. Working fluid in the experiments is nitrogen due to the fact that presence of oxygen quenches the MTV chemicals. Note that MTV is a molecular counterpart of particle-based techniques, and it eliminates the use of seed particles. Biacetyl is used as the tracer molecule. An experimental study is performed to investigate the cycle-to-cycle variations on in-cylinder flow inside an optical internal combustion engine assembly. Both tumble and swirl measurement planes are considered at different engine speeds. Effects of charge motion control valve (CMCV) are presented and compared with the similar cases when

CMCV was deactivated. Probability density functions of the normalized circulation are calculated from the instantaneous planar velocity to quantify the cycle-to-cycle variations of in-cylinder flow. In-cylinder engine flow measurements are then extended to obtain an instantaneous three-component velocity field using stereoscopic molecular tagging velocimetry (SMTV). A novel image processing technique is implemented to obtain the velocity data. The technique has the advantage that it eliminates the geometric details required to obtain the three components of the velocity field. The procedure involves two major steps: (i) calibration process and (ii) data acquisition and reduction. More details of the technique are presented in Chapter 3 of this dissertation. Ensemble-averaged velocity and the rms of three-component velocity field are presented inside the engine cylinder. The three-component planar velocity field confirmed that during the intake stroke in-cylinder flow is highly turbulent, complex and three-dimensional. This work can be utilized as a tool for engine developers where only the logistics of operation need to be described.

Experimental measurements provide useful information of the flow fields inside the engine cylinder; however, it is multi-dimensional numerical simulations that offer the potential of significant time and cost savings to design the engine with improved performance. To date, multi-dimensional numerical simulations of in-cylinder flows are performed with assumed boundary conditions. Real-time boundary conditions are necessary to perform more accurate multi-dimensional numerical simulations of complex in-cylinder flows. Therefore, velocity and pressure measurements are performed inside the intake manifold of an engine assembly that can provide these necessary boundary conditions. The geometry of the intake manifold is simplified for this purpose. A hot-wire

anemometer and piezoresistive type absolute pressure transducers are used to measure the velocity and pressure, respectively. In-cylinder flow measurements are also performed to validate the modeling efforts. Stereoscopic molecular tagging velocimetry is used for this purpose.

In-cylinder combustion diagnosis is performed in a dual fueled, single-cylinder, spark-ignition engine. Cycle-to-cycle variability is presented using the coefficient of variation in indicated mean effective pressure. Mass fraction burned and burn duration are determined from the analysis of measured in-cylinder pressure data. The Rassweiler and Withrow method (Model 1), with a new linear model for the polytropic index, is used to obtain the MFB curves. Start of combustion and end of combustion are determined using a least-square fit algorithm. In addition, results of mass fraction burned using a net pressure method (Model 2) are presented and compared with the results of Model 1, i.e. Rassweiler and Withrow method. Model 2 is of interest as it offers an advantage that the data processing time is short enough to allow for online processing.

CHAPTER-2

A STUDY OF CYCLE-TO-CYCLE VARIATIONS ON IN-CYLINDER FLOW IN AN IC ENGINE EQUIPPED WITH CMCV USING MTV

2.1 Introduction

As discussed in Chapter 1, the flow fields inside the engine cylinder are extremely complex and exhibit large cycle-to-cycle variations. It is to be noticed that the high cycle-to-cycle variations affect the fuel-air mixing and flame propagation during the combustion process, and hence influence the engine performance. Therefore, an understanding of cycle-to-cycle variations is needed to optimize the engine design. Flow inside an engine cylinder is affected by several factors including engine geometry, speed, load, valve timing and lift. In addition to these factors, the intake charge motion control valve is an important factor that affects the flow inside an engine cylinder. It is expected that the CMCV imparts an angular momentum to the charge entering the engine cylinder. Clarke and Stein⁵⁵ (1999) combined the variable valve timing with charge motion control valve. Variable valve timing was obtained using dual equal variable camshaft timing (VCT) strategy. More details about the dual equal VCT can be found in Stein et al.⁵⁶ (1995). The combination of dual equal VCT with a CMCV allows an engine to be operated either at or near stoichiometry or at lean conditions, which allows the use of a NO_x trap for the purpose of further reducing the air pollution. Authors further discussed that the synergy between the CMCV and the dual equal VCT allows the fuel consumption to be less than the fuel consumption during lean operation at standard valve timing. This

is due to the fact that CMCV increases the in-cylinder charge motion and hence improves the combustion and the ability to handle the charge dilution which occurs from increased levels of internal exhaust gas recirculation resulting from valve timing retard. Li et al.⁵⁷ (2000) investigated the effects of swirl control valve (SCV) on in-cylinder flow characteristics using laser doppler anemometry. They found that SCV closed condition produced both swirl and tumble motion in the cylinder and the mean velocity was nearly doubled in comparison to the SCV open condition. Schock et al.⁴² (2003) studied the effects of tumble and swirl port blockers on cyclic variations of flow in a piston cylinder assembly. They found that swirl port blocker strengthens both tumble and swirl motions; however, tumble port blocker only strengthens the tumble motion. Kim et al.⁵⁸ (2005) investigated the effects of injection timing and intake port flow control on fuel wetting inside the engine cylinder. They found that a tumble mixture-motion plate inside the intake port significantly reduced cylinder liner and piston top fuel wetting. This is because the use of tumble mixture-motion plate provided more turbulence, which effectively enhanced the mixing during the intake process. Lee and Heywood⁵⁹ (2006) studied the effects of CMCV on combustion characteristics and hydrocarbon emissions. The authors concluded that CMCV improved mixture preparation due to increased swirl and tumble intensities, which enhanced fuel transport, distribution and evaporation. CMCV in closed condition allowed reduced fuel injection and retarded spark timing strategies that reduced hydrocarbon emissions significantly during cold start due to greater fuel evaporation and faster burning rate.

Overall, previous investigations show that a charge motion control valve is an important factor that controls the combustion process and hence influences the engine performance. However, studies of charge motion control valve on in-cylinder flows are limited. Therefore, an experimental study is performed to investigate the effects of charge motion control on flow measurement inside an internal combustion engine assembly. Molecular Tagging Velocimetry is used to obtain the multiple point measurement of the instantaneous velocity field. A two-component velocity field is obtained at various crank angle degrees for swirl and tumble measurement planes inside the optical engine assembly at 1500 and 2500 rpm engine speeds. Effects of charge motion control are studied considering different cases of: (i) Charge motion control valve deactivated and (ii) CMCV activated. Both the measurement planes are used in each case to study the cycle-to-cycle variability inside the engine cylinder. Probability density functions of the normalized circulation and the turbulent kinetic energy of flow are calculated from the instantaneous planar velocity to quantify the cycle-to-cycle variations of in-cylinder flows. Different geometries of CMCV produce different effects on the in-cylinder flow field. It is found that the CMCV used in this work has a profound effect on fuel-air mixing; however, its influence is not as significant during the late compression. Therefore, it can be assumed that CMCV has less contribution to enhance the flame speed during the combustion process.

2.2 Experimental setup and procedure

2.2.1 Experimental setup

The motored optical engine assembly used for the experiments is a three-valve, two intakes and one exhaust, 0.675 l single-cylinder engine; see Figure 2.1. Specifications are listed in Table 2.1 with a bore diameter of 90 mm and a stroke length of 105.6 mm. Figure 2.2 shows the intake and exhaust valves lifts. As shown in the figure, intake valves open shortly before the top dead center at the start of intake stroke and close after the intake stroke ends. The exhaust valve opens before the power stroke ends (at BDC) and closes shortly after TDC of intake.

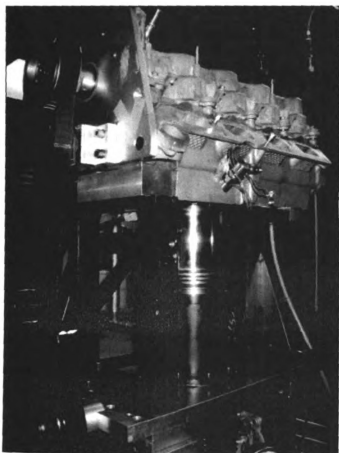


Figure 2-1. Optical engine assembly

Specifications	Measure
Bore (mm)	90
Stroke (mm)	105.6
Compression ratio	10
Stroke/Bore ratio	1.17
Connecting rod length (mm)	169

Table 2-1. Engine specifications

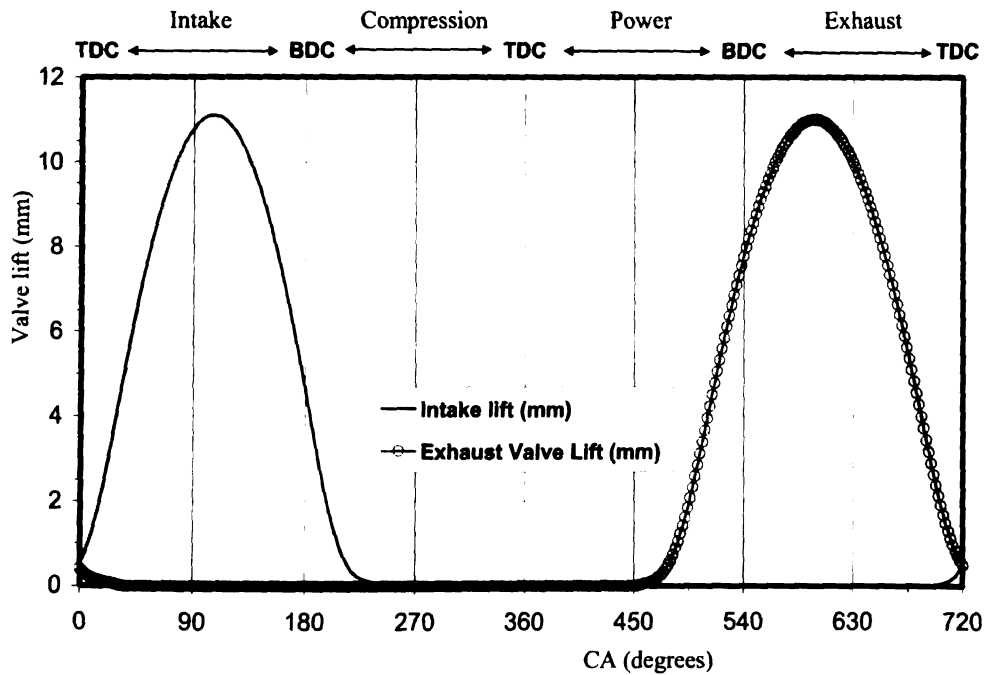


Figure 2-2. Intake and exhaust valves lift

Figure 2.3 shows the locations of the swirl and tumble measurement planes inside the engine cylinder. As shown in the figure, the swirl plane is located 24.5 mm below the head deck level. Measurements with 1500 rpm engine speed are performed at 121 crank

angle degree during the intake stroke and at 192, 257, and 300 crank angle degrees during the compression stroke. Similarly, measurements are performed at 138 and 171 crank angle degrees (CADs) during the intake stroke and at 221 and 253 CADs during the compression stroke at 2500 rpm engine speed. Zero crank angle degree represents the start of the intake stroke, i.e. piston at top dead center of the intake. 180 crank angle degree represents the BDC of the intake stroke. Similarly, 360 CAD represents the TDC of the compression.

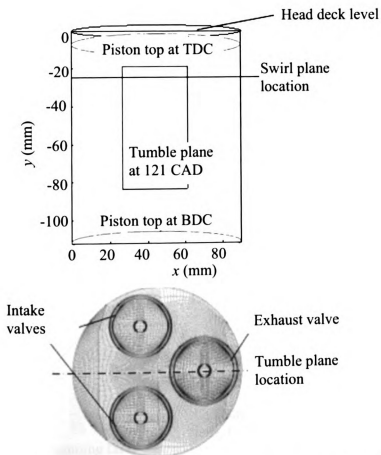


Figure 2-3. Tumble and swirl measurement planes inside the IC engine cylinder

The optical setup used for the molecular tagging velocimetry measurements inside the engine cylinder is shown in Figure 2.4. It consists of a pulsed ultraviolet (UV) laser,

whose light beam is used to create a grid pattern in the cylinder. The UV laser beam used in this work is produced by a Lambda Physik excimer laser device, LPX205i, filled with XeCl. This laser device provides laser pulses at a wavelength, λ , of 308 nm and repetition rates up to 60 Hz. Figures 2.5 and 2.6 shows the front and rear views of the LPX205i. The laser beam passes through numerous optical elements (including mirrors, a beam splitter and cylindrical lenses) that generate two light sheets. Beam blockers are used to transform the light sheets into sets of laser beams that are introduced into the cylinder through the optical cylinder and the optical piston head.

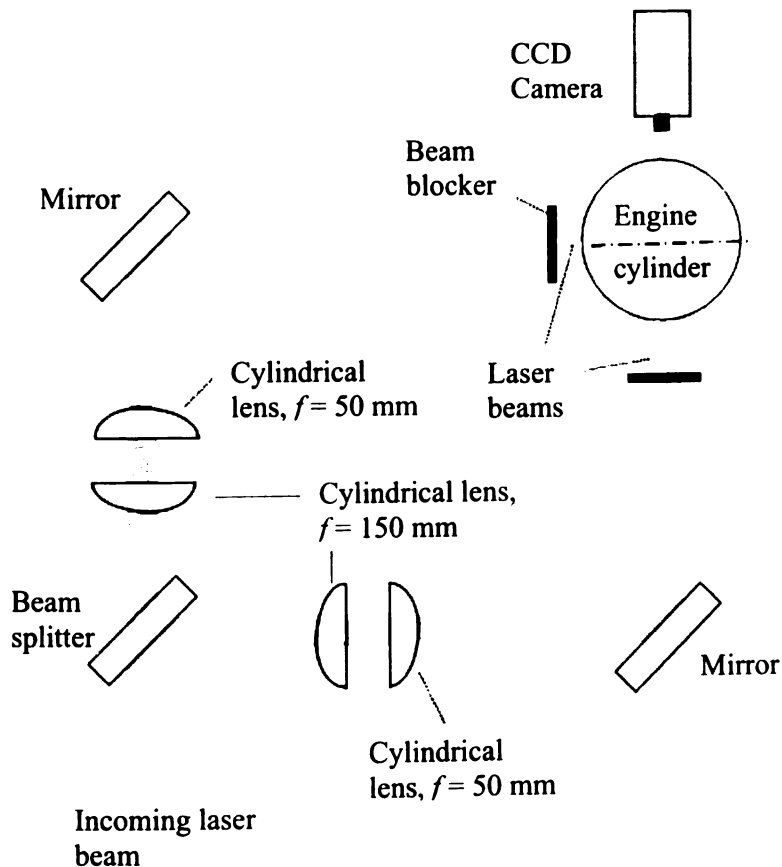


Figure 2-4. Schematic of MTV optical setup for in-cylinder flow measurement

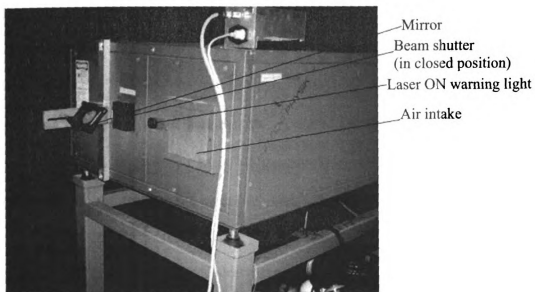


Figure 2-5. Front view of LPX205i

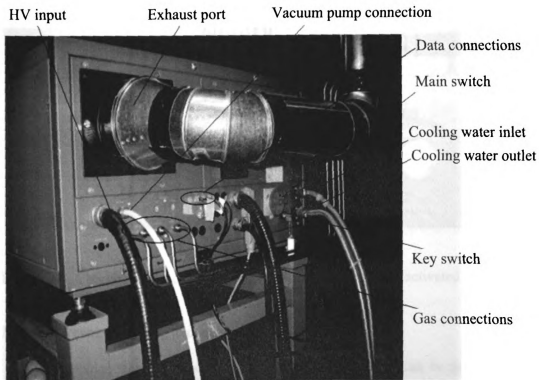


Figure 2-6. Rear view of LPX205i

2.2.2 Charge motion control valve

It is believed that charge motion control valves have a profound influence on the flow field, even to late compression which affects the fuel-air mixing and hence the combustion process, Mittal and Schock⁶⁰ (2009). The nature of CMCV influence depends on its geometry which likely produces different flows with different geometries. Figure 2.7 shows the charge motion control valve device used in this experiment, installed between the intake manifold and the intake port. Experiments are performed with both the conditions: CMCV deactivated and CMCV activated. It is expected that charge motion is enhanced, both in tumble and swirl measurement planes, with the activated CMCV. This work quantifies the magnitude of this enhanced motion at different crank angle degrees.

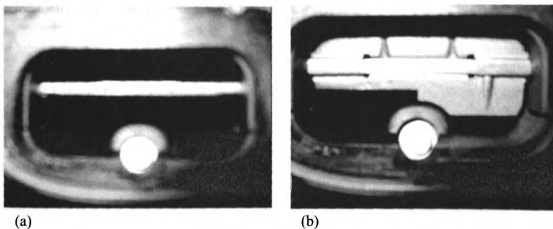


Figure 2-7. Charge motion control valve; (a) deactivated, and (b) activated

2.2.3 Molecular tagging procedure

Molecular tagging velocimetry relies on molecules that can be turned into long lifetime tracers upon excitation by photons of an appropriate wavelength, Koochesfahani

and Nocera⁶¹ (2007). Biacetyl ($\text{CH}_3\text{COCOCH}_3$) is used in this work as a tracer molecule. It is worth noting a brief description of biacetyl properties relevant to this dissertation. Table 2.2 shows the physical properties of biacetyl [62]. Figure 2.8 shows the absorption spectrum of biacetyl, which has a peak at about $\lambda = 420$ nm; Stier and Koochesfahani⁶³ (1999). It is to be noticed that the absorption increases below $\lambda = 330$ nm and has a second peak at about $\lambda = 270$ nm. This shows that the laser device used in this study with $\lambda = 308$ nm is a suitable source of excitation. The working fluid used in this experiment is nitrogen, since the presence of oxygen quenches the phosphorescence of biacetyl. The tracer molecules are premixed into nitrogen gas by an evaporation process in a preparation tank before entering the IC engine. The excitation of biacetyl leads to both fluorescence and phosphorescence emissions; the latter being used for velocimetry. The phosphorescence lifetime of biacetyl is reported to be as high as 1.5 ms; Sidebottom et al.⁶⁴ (1972). Stier and Koochesfahani⁶³ (1999) measured a lifetime of about 0.1 ms in their work using an excimer laser ($\lambda = 308$ nm). The observed lifetime may be lower unless all oxygen is completely purged from the flow system. Stier and Koochesfahani⁶³ (1999) compared the phosphorescence emission spectra of biacetyl at different excitation wavelengths; see Figure 2.9. They found that the wavelength with more absorption leads to more phosphorescence emission. The authors reported that $\lambda = 308$ nm is also a suitable source of excitation for phosphorescence emission.

Parameter	Measure
Molecular formula	C ₄ H ₆ O ₂
Appearance	Liquid with a butter-like odor
Melting point	-2 to -4 C
Boiling point	88 C
Vapor density	3 (air = 1)
Vapor pressure	52 mm Hg at 20 C
Synonyms	diacetyl, 2,3-butanedione

Table 2-2. Properties of biacetyl

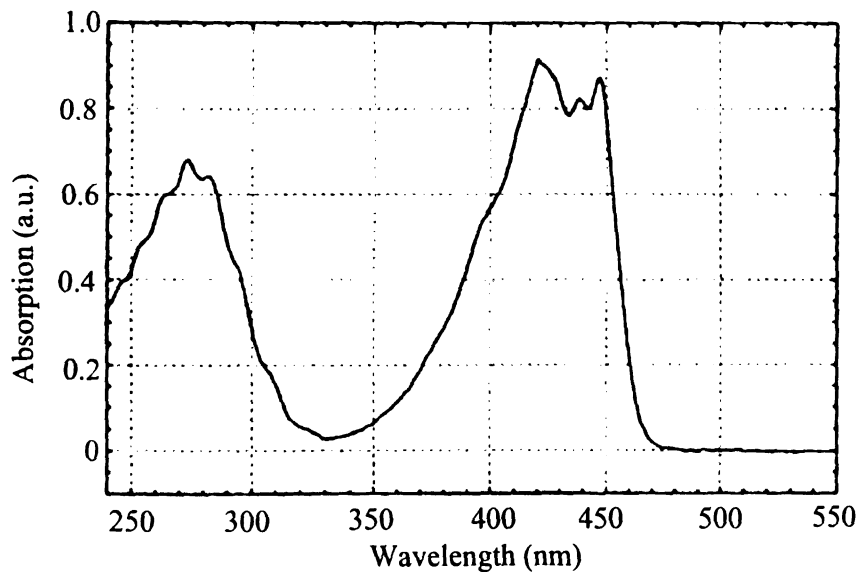


Figure 2-8. Absorption spectrum for biacetyl (Stier and Koochesfahani, 1999)

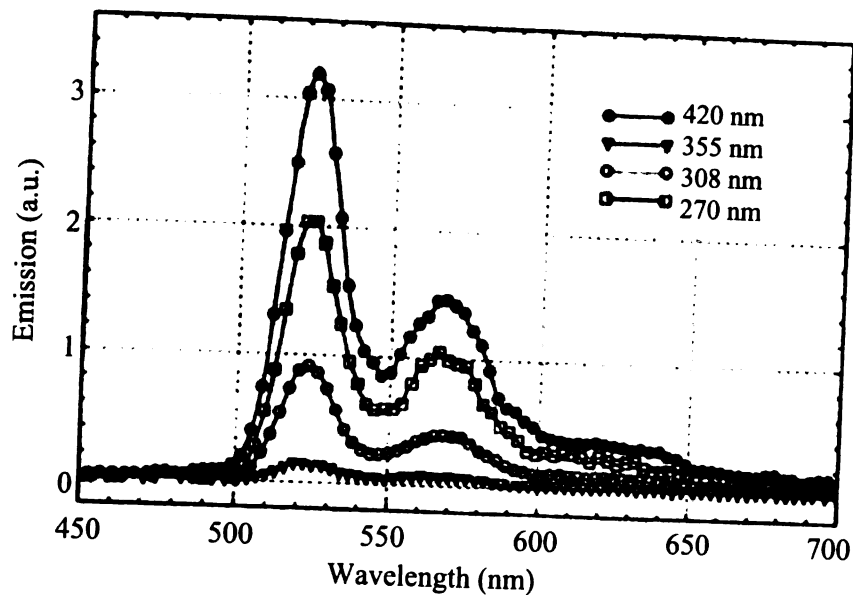


Figure 2-9. Phosphorescence emission spectrum for biacetyl at four different excitation wavelengths (Stier and Koochesfahani, 1999)

The MTV images at two successive time levels are recorded using a Xybion ISG intensified CCD (charge coupled device) camera. Each image is an 8 bit image with the size of 640×480 pixels. The reference (undelayed) image is recorded as soon as the grid pattern is written and the delayed image after a certain delay, 12-35 μ s. Figure 2.10 shows a sample of undelayed (left) and delayed (right) images for the tumble measurement plane at 138 crank angle degree. Similar images are obtained for the swirl measurement plane at various crank angle degrees. The images are processed using a data reduction program to find the displacement at each grid point. At each measured crank angle degree, 200 undelayed frames are recorded to obtain the averaged undelayed image. This is to reduce the noise in undelayed image. Note that the displacement at each grid point is zero when an undelayed image is spatially correlated with the averaged undelayed image. 500 delayed frames are considered at each crank angle measurement to

obtain the instantaneous velocity fields in this work. A spatial image correlation technique is used to obtain the displacement vectors within one pixel for the tagged region, Gendrich and Koochesfahani²⁹ (1996). More details can be found in Section 3.3. Sub-pixel accuracy is obtained using a fourth order polynomial which requires a minimum of 15 data points from the correlation field. The location corresponding to the maximum correlation coefficient is found using a decoupled method as presented by Zheng and Klewicki⁶⁵ (2000). Artificial images, with signal to noise ratio of 5, are used to obtain the accuracy of the data reduction program with a known spatial distribution of displacements. These images are processed using the data reduction program to obtain the displacements. The obtained values are then used to estimate the accuracy of the measurement technique. The uncertainty in determining the displacements is less than 0.05 pixels. Similar results are obtained using a fifth order polynomial; however, a third order polynomial is insufficient to fit the correlation coefficient data.

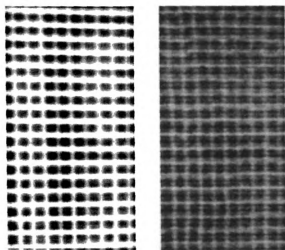


Figure 2-10. Undelayed (left) and delayed (right) images for tumble measurement plane at 138 crank angle degree

2.3 Experimental Results

Measurement results of complex in-cylinder flow are presented at various crank angle degrees during the intake and compression strokes. Both swirl and tumble measurement planes are considered. Influence of charge motion control valve is presented and its results are compared with similar cases when engine was operated with deactivate CMCV. Experiments are performed at 1500 and 2500 rpm engine speeds. 500 delayed frames are considered to obtain the instantaneous velocity field at each crank angle degree measurement, unless specified. Then velocity statistics are calculated.

2.3.1 Swirl measurement plane, 1500 rpm

For the swirl plane at 1500 rpm engine speed, measurements are performed during the intake stroke at 121 crank angle degree and during the compression stroke at 257 and 300 crank angle degrees. Figure 2.11 shows the ensemble-averaged velocity vectors and the contours of rms velocity when engine was operated with deactivated (left) and activated (right) CMCV at 121 (upper graphs) and 300 (lower graphs) CADs, respectively. The vectors in the plots show the magnitude of ensemble-averaged velocity vectors $\langle u \rangle$, Equation 2.1, and $\langle v \rangle$. Note the notation, $\langle \rangle$, used here for ensemble-averaged.

$$\langle u \rangle = \frac{1}{n} \left(\sum_{i=1}^n u_i \right) \quad (2.1)$$

where n is the total number of delayed frames.

As shown in the figure, the velocity magnitudes are higher at 121 CAD during the intake stroke and reduce during the compression stroke. Similarly, the rms values decay during the compression stroke. It is to be noticed that the rms cyclic variations are considerably enhanced with the activated CMCV at 121 CAD, and they are as high as 20 m/s. The higher rms values at 121 CAD show that the flow at this crank angle is highly turbulent in nature with both the intake valves open. The cyclic variations decay during the compression stroke. These results are consistent with the earlier literature; see Jarvis et al.²⁴ (2006). They found high rms values during the intake stroke at 149 CAD. These values reduce as the compression stroke is traversed. There are some counterclockwise rotations that can be observed toward the upper right half of the plane and some clockwise rotations at the lower left half of the plane (at 121 CAD) with activated CMCV.

Figure 2.12 shows the influence of considering different number of consecutive cycles to evaluate the ensemble-averaged velocity vectors, $\langle u \rangle$ and $\langle v \rangle$. The three plots, a, b and c, in the figure are obtained considering 1-100, 101-200 and 1-500 consecutive frames, respectively, with activated CMCV at 121 crank angle degree. The figure shows that the mean field is quite stable when calculated with 100 consecutive frames. In general, more frames are required to calculate the higher order turbulence statistics, for example, the probability density function of the normalized circulation, turbulent kinetic energy, etc. Therefore, 500 delayed frames are considered in our further investigation to obtain the instantaneous velocity field at each crank angle degree and then the velocity statistics are calculated.

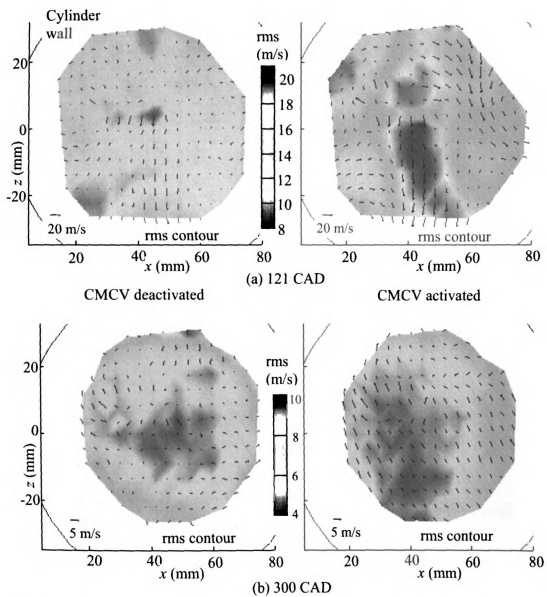


Figure 2-11. Ensemble-averaged velocity vectors, contours of velocity rms for deactivated (left) and activated (right) CMCV at (a) 121 (top), and (b) 300 (bottom) CADs; swirl measurement plane at 1500 rpm

Figure 2-12. Ensemble-averaged velocity vectors with activated CMCV at 121 CAD considering (a) 1-100, (b) 101-200, and (c) 1-500 consecutive undelayed frames; swirl measurement plane at 1500 rpm

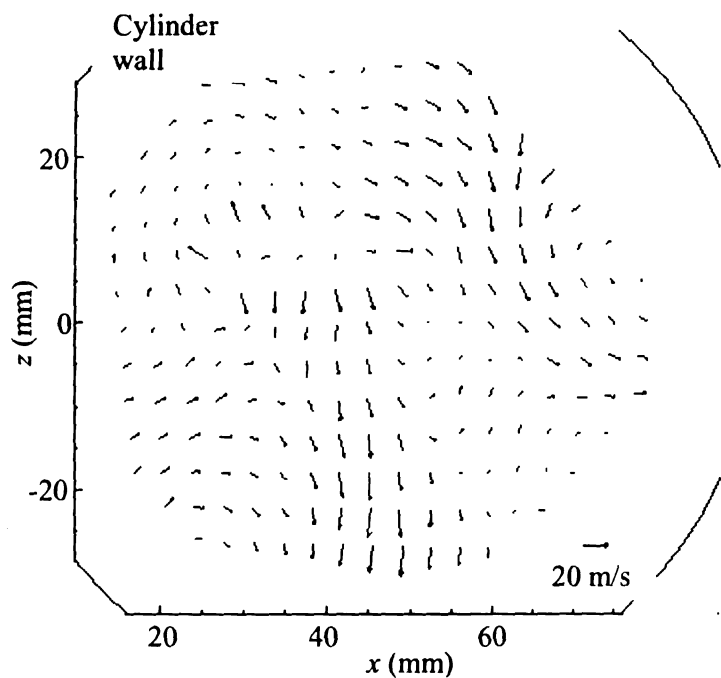


Fig. 2-12 (a)

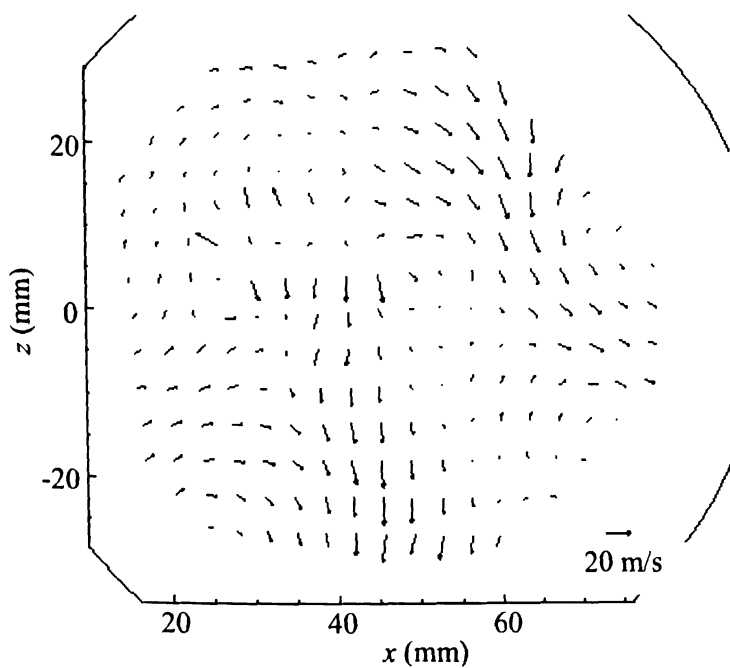


Fig. 2-12 (b)

Figure 2-12, continued

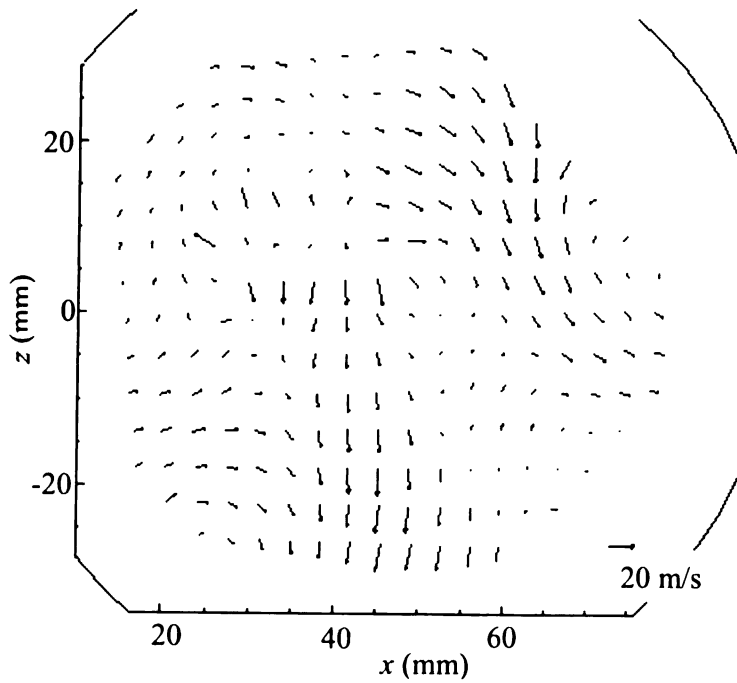


Fig. 2-12 (c)

Figures 2.13 (a), (b) and (c) show the instantaneous velocity vector fields for three consecutive engine cycles, i.e. 99, 100 and 101. Ensemble-averaged velocity field (Fig. 2.13, d) is also presented for the comparison. The instantaneous flow fields show large cycle-to-cycle variations with significant difference from the ensemble-averaged velocity field. Mean subtracted flow field for 101 engine cycle is shown in Figure 2.14 b. The high fluctuations in velocity are evident from the plot.

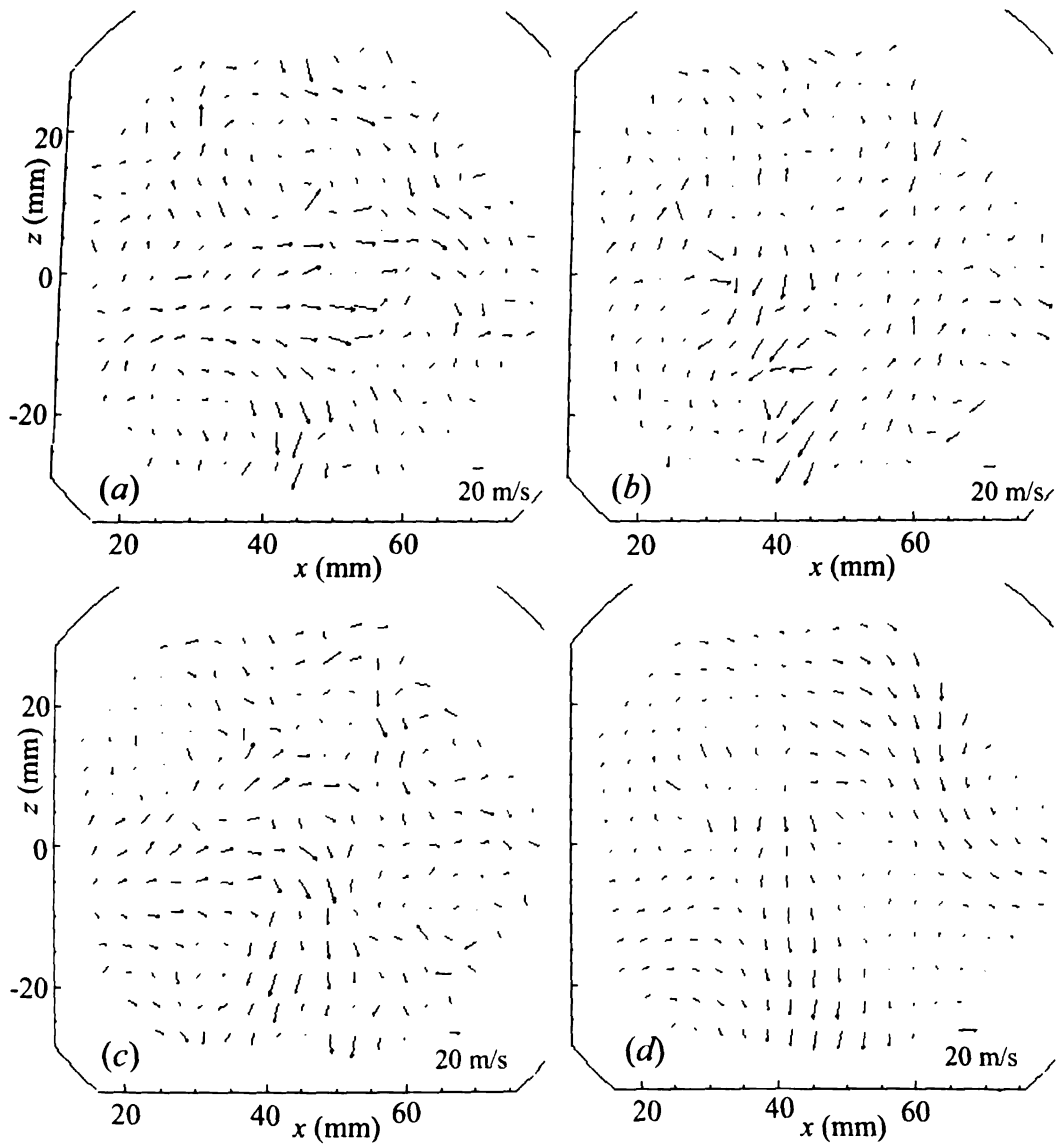


Figure 2-13. Instantaneous velocity fields from consecutive engine cycles 99^a, 100^b and 101^c, and ensemble-averaged velocity field^d with activated CMCV at 121 CAD; swirl measurement plane at 1500 rpm

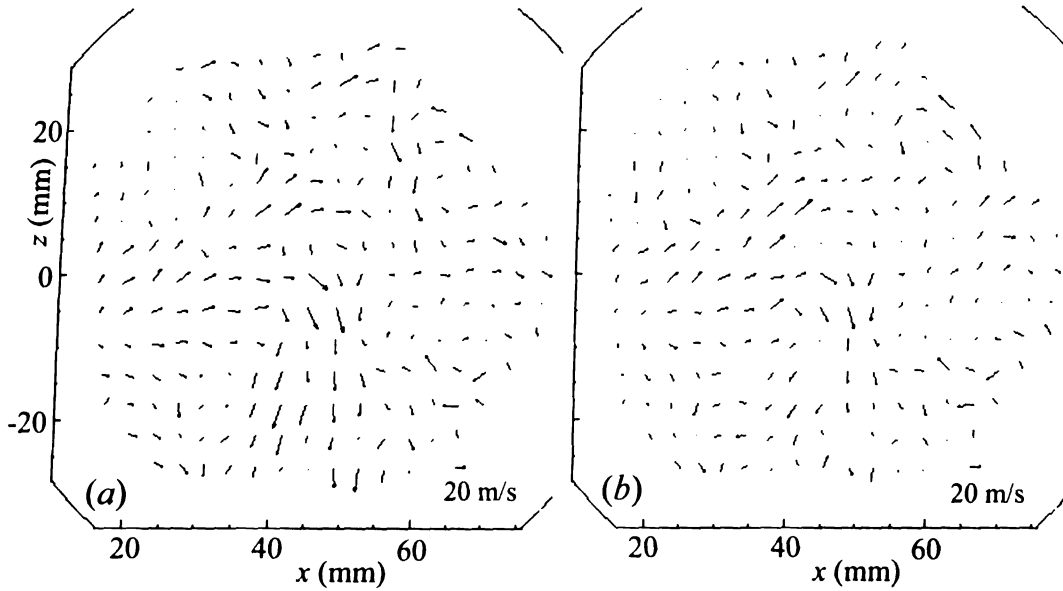


Figure 2-14. Instantaneous velocity field^a and mean subtracted flow field^b for 101st cycle at 121 CAD with activated CMCV; swirl measurement plane at 1500 rpm

The circulation of the flow on a swirl or tumble measurement plane can be used as a primary parameter to characterize the rotational motion of the flow, Schock et al.⁴² (2003). Circulation, Γ , is defined as follows:

$$\Gamma = \oint_C \bar{V} \cdot d\bar{l} = \iint_A \bar{\omega} \cdot d\bar{A} \quad (2.2)$$

where C is a closed curve on a tumble or swirl measurement plane and A is the area enclosed by the curve C .

It is to be noticed that when the flow on swirl or tumble measurement plane is studied at different CADs, the area of each plane is not the same. Therefore, to compare the results, the circulations of flow on different planes have to be normalized by their respective areas, Schock et al.⁴² (2003), which is

$$\Gamma_N = \frac{1}{A_S} \oint_C \bar{V} \cdot d\bar{l} = \frac{1}{A_S} \iint_{A_S} \bar{\omega} \cdot d\bar{A} \quad (2.3)$$

where A_S is the studied area of the swirl or tumble measurement plane. Note that Γ_N , by definition, is the averaged vorticity. To be consistent with the literature, this averaged vorticity over the computational plane is referred as the normalized circulation (NC). In this work, e.g., over the tumble measurement plane, vorticity ω_z , Equation 2.4, for two-component velocity field is computed using a second order accurate finite difference technique (Cohn and Koochesfahani⁶⁶, 2000), and then the spatial mean is calculated to obtain the averaged vorticity (or normalized circulation). Each frame has different NC because of the cyclic variability. 500 frames are considered in this work to obtain the PDF plot of the normalized circulation for each case.

$$\omega_z = \frac{\partial v}{\partial x} - \frac{\partial u}{\partial y} \quad (2.4)$$

Figure 2.15 shows the probability density function (PDF) plot of the normalized circulation at different CADs with deactivated CMCV at 1500 rpm engine speed. The mean value of normalized circulations gives the ensemble-averaged information of the flow inside an engine cylinder. The range of NC variation quantifies the cycle-to-cycle variability of the flow. A more representative measure to quantify the cycle-to-cycle variation inside the engine cylinder is the standard deviation (σ) of NC PDF. Almost all the change in PDF occurs within ± 3 standard deviations. As shown in the figure, standard deviation of NC decreases from 121 CAD ($\sigma=205.33$ Hz) to 257 CAD ($\sigma=96.76$ Hz). The shift in peak shows that the negative circulations are more probable

at the later crank angle. It then increases slightly at 300 CAD ($\sigma=101.18$ Hz). These results show that cycle-to-cycle variation decreases from 121 CAD to 257 CAD, and then increases slightly to CAD 300. Figure 2.16 shows the PDF plot of normalized circulation with activated CMCV. As shown in the figure, standard deviation decreases from 121 CAD ($\sigma=304.37$ Hz) to 300 CAD ($\sigma=109.17$ Hz). It is interesting to note that CMCV effects are not significant on cycle-to-cycle variation at 300 CAD when compared to the results of deactivated CMCV; see Figure 2.15 for comparison. This shows that CMCV has a considerable effect on fuel-air mixing at this engine speed, i.e. 1500 rpm, for the swirl measurement plane; however, it has less contribution to enhance the flame speed for faster combustion.

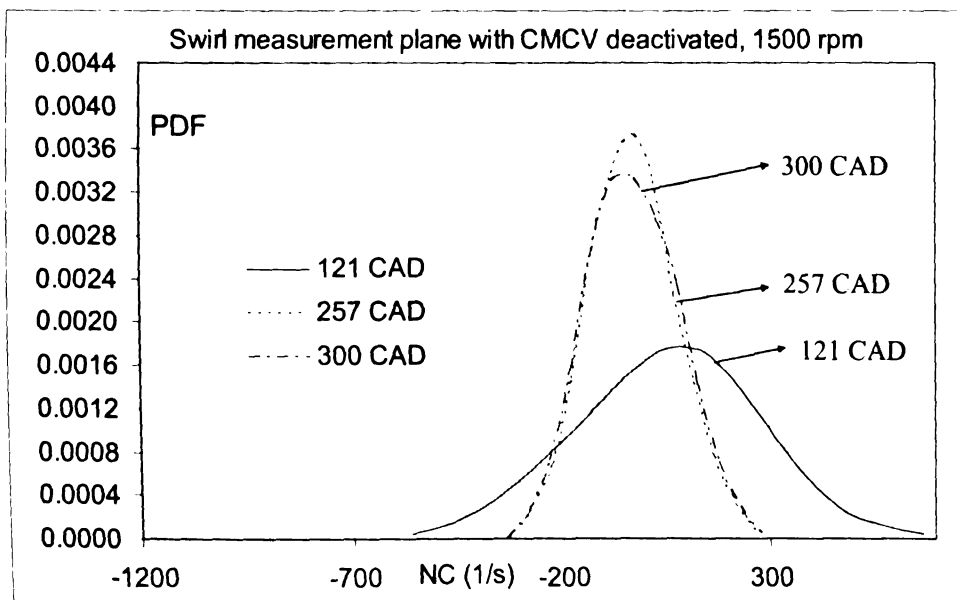


Figure 2-15. PDFs of normalized circulation at different CADs for swirl measurement plane with CMCV deactivated at 1500 rpm engine speed

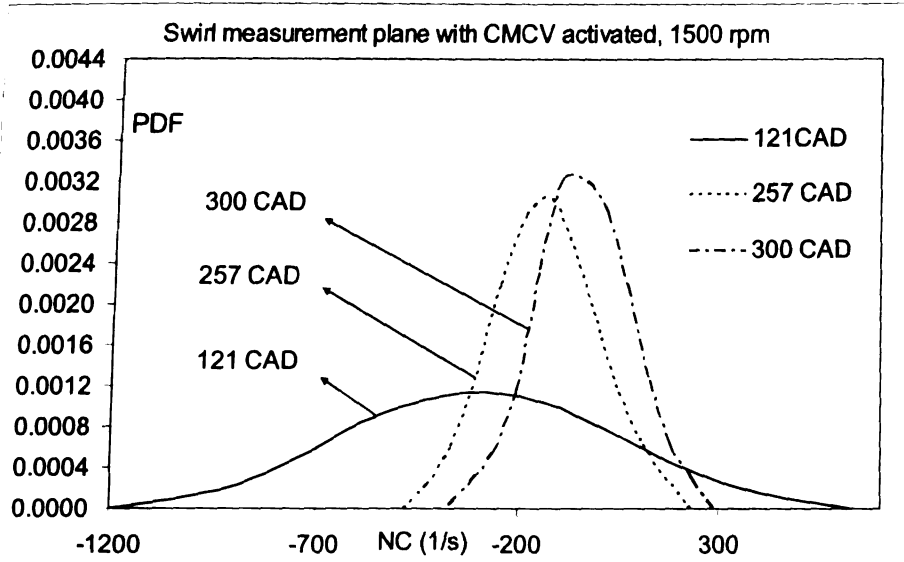


Figure 2-16. PDFs of normalized circulation at different CADs for swirl measurement plane with CMCV activated at 1500 rpm engine speed

The flow field inside an engine cylinder is highly turbulent; and, thus, the flow characteristics at any point are different from cycle-to-cycle. The velocity fields are further processed to evaluate the turbulent kinetic energy. For swirl measurement plane, the turbulent kinetic energy is calculated as follows;

$$k = \frac{1}{2} \left(\langle u'^2 \rangle + \langle v'^2 \rangle + \langle w'^2 \rangle \right) \approx \frac{3}{4} \left(\langle u'^2 \rangle + \langle w'^2 \rangle \right) \quad (2.5)$$

where $\langle v'^2 \rangle$ is estimated as $\left(\langle u'^2 \rangle + \langle w'^2 \rangle \right) / 2$ in equation 2.5, Miles et al.⁶⁷ (2003).

Similarly $\langle w'^2 \rangle$ is estimated as $\left(\langle u'^2 \rangle + \langle v'^2 \rangle \right) / 2$ when the TKE is evaluated for the

tumble measurement plane. The local TKE, at each grid node, is then used to evaluate the

averaged TKE over the studied plane. With N points over the plane and the local TKE, k_i , the averaged TKE, k_{avg} , over the plane is;

$$k_{avg} = \frac{1}{N} \left(\sum_{i=1}^N k_i \right) \quad (2.6)$$

Figure 2.17 shows the change in cycle-to-cycle variability characterized by averaged turbulent kinetic energy over the swirl measurement plane at 1500 rpm engine speed with respect to the crank angle. The values are normalized by s_p^2 where s_p is the mean piston speed, Equation 2.7 (Heywood², 1988),

$$s_p = 2LN \quad (2.7)$$

L is the stroke and N is the rotational speed. Note that the mean piston speeds at 1500 and 2500 rpm of engine speeds in this work are 5.3 and 8.8 m/s, respectively. The results are qualitatively in agreement with the PDF of NC results as shown in Figures 2.15 and 2.16. The CMCV effect on cycle-to-cycle variation is significant during the intake stroke; however, the effect reduces traversing during the compression stroke.

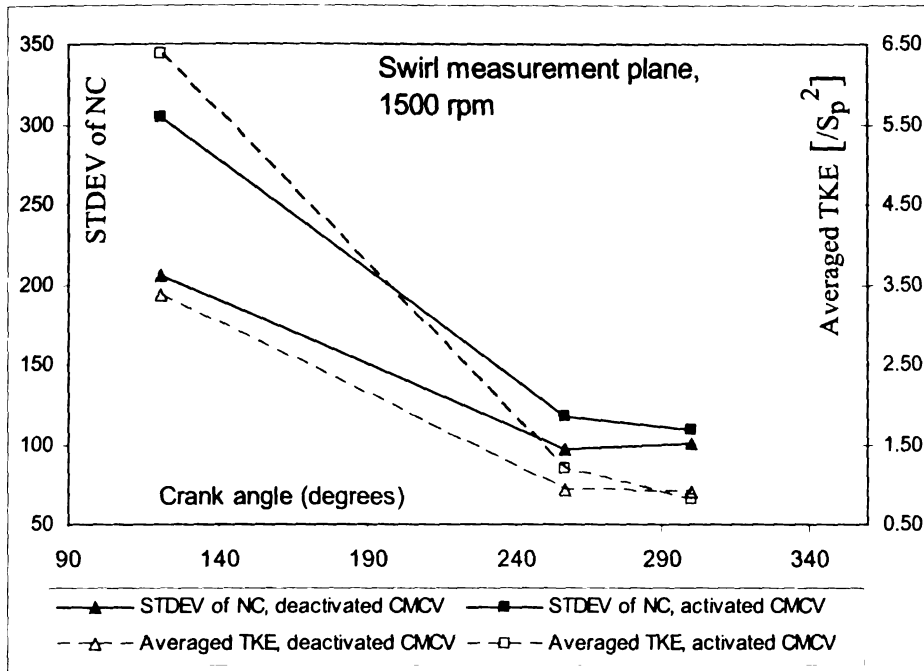


Figure 2-17. Standard deviation of normalized circulation and turbulent kinetic energy at different CADs for swirl measurement plane at 1500 rpm engine speed

2.3.2 Swirl measurement plane, 2500 rpm

For the swirl plane at 2500 rpm engine speed, measurements are performed at 138 and 171 crank angle degrees during the intake stroke and at 221 and 253 CADs during the compression stroke with wide open throttle (WOT). Figure 2.18 shows the ensemble-averaged velocity vectors and the contours of rms velocity when the engine was operated with deactivated (left) and activated (right) CMCV at 171 (top) and 221 (bottom) CADs, respectively. The vectors in the plots show the magnitude of ensemble-averaged velocity vectors $\langle u \rangle$ and $\langle v \rangle$. The velocity magnitudes show that CMCV enhances the flow field at 171 CAD during the intake stroke and its effects relatively decay during the compression stroke at 221 CAD. However, the presence of swirl motion is still evident with activated CMCV; see some counterclockwise and clockwise rotations toward the

right half and lower left half of the plane, respectively, with activated CMCV. The rms values with activated CMCV at 171 CAD are higher than 17 m/s toward the center of the measurement plane. Some clockwise rotations can also be observed at this crank angle toward the lower left half of the plane. It is to be noticed that the rms values decay during the compression stroke for both the cases. However, the rms cyclic variations are still higher with activated CMCV during the compression stroke at 221 CAD (note the maximum value of about 13 m/s).

Figures 2.19 and 2.20 show the PDF plots of normalized circulation at different CADs for swirl plane at 2500 rpm engine speed with deactivated and activated CMCV, respectively. As shown in the figures, the standard deviation of NC decreases from 138 CAD ($\sigma = 305.53$ Hz) to 253 CAD ($\sigma = 117.11$ Hz) for deactivated CMCV. These results show that cycle-to-cycle variation decreases from 138 to 253 CAD with deactivated CMCV. With activated CMCV, the standard deviation decreases from 138 CAD to 221 CAD, and then increases slightly at 253 CAD. The CMCV effect shows significant enhancement in cycle-to-cycle variation at 171 CAD during the intake stroke. However, it is interesting to note that the effect is not significant at 138 CAD at this higher engine speed.

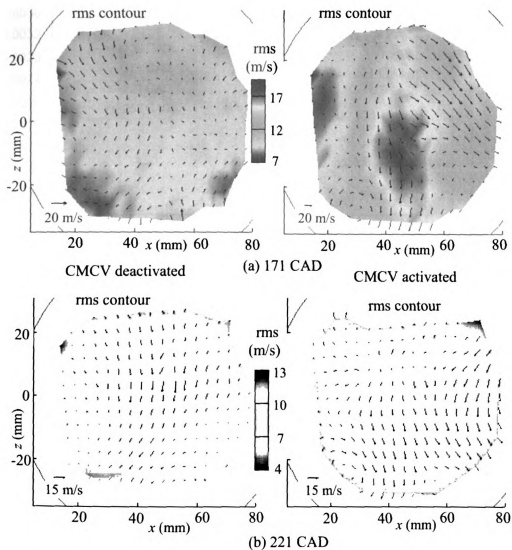


Figure 2-18. Ensemble-averaged velocity vectors, contours of velocity rms for deactivated (left) and activated (right) CMCV at (a) 171 (top), and (b) 221 (bottom) CADs; swirl measurement plane at 2500 rpm engine speed

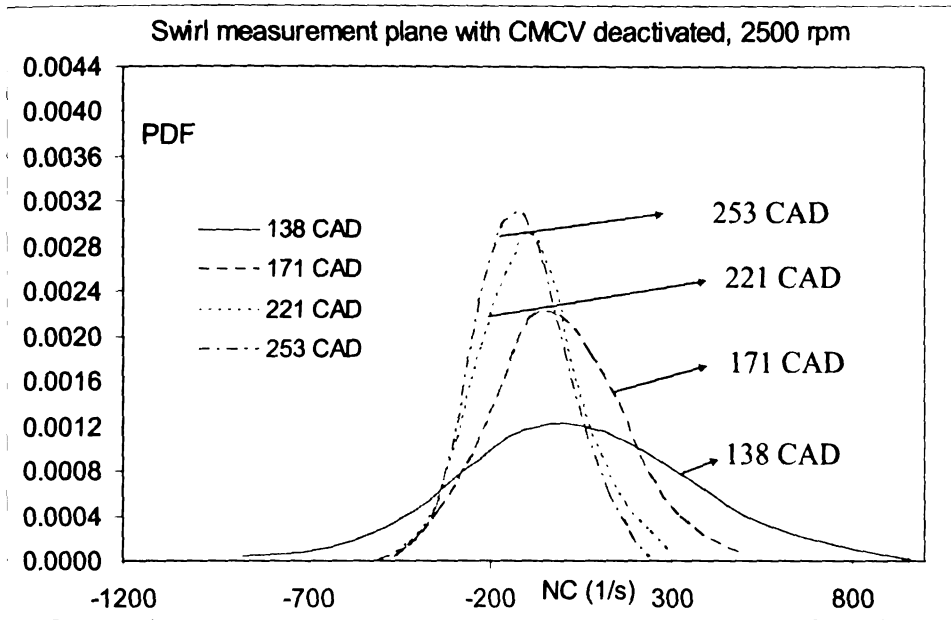


Figure 2-19. PDFs of normalized circulation at different CADs for swirl measurement plane with CMCV deactivated at 2500 rpm engine speed

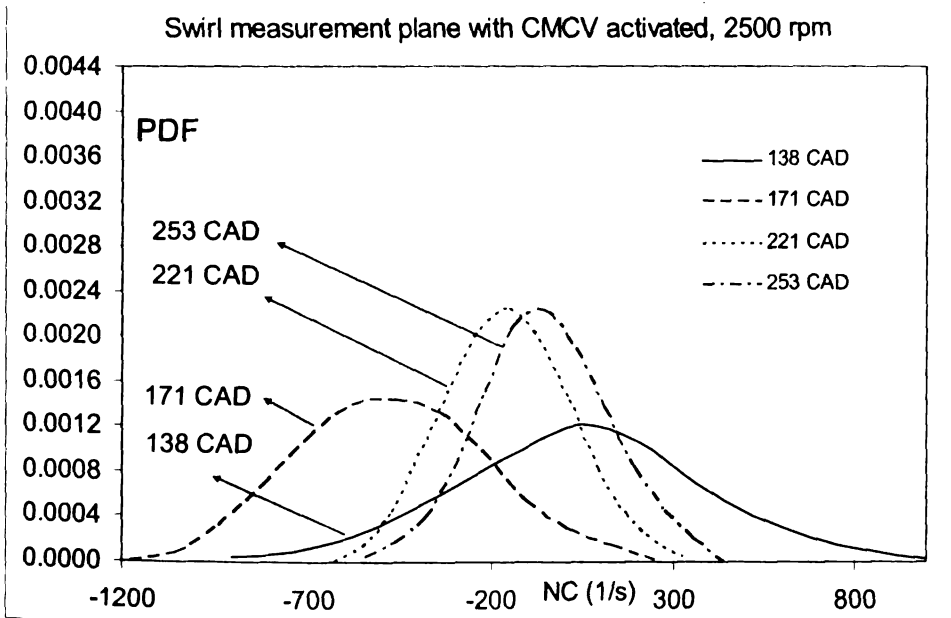


Figure 2-20. PDFs of normalized circulation at different CADs for swirl measurement plane with CMCV activated at 2500 rpm engine speed

Figure 2.21 shows the change in cycle-to-cycle variability characterized by the standard deviation of NC and averaged TKE over the plane with respect to the crank angle. The TKE with activated CMCV is only slightly higher than that of deactivated CMCV at 138 CAD, as also seen in the PDF plots. The cycle-to-cycle variations are higher with activated CMCV at 171 CAD and reduce during the compression stroke.

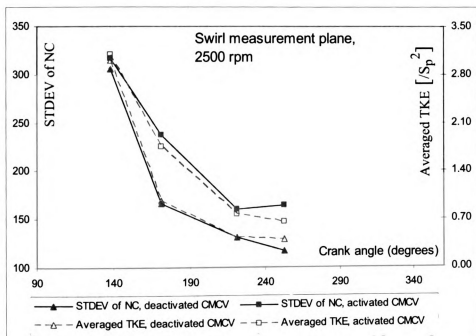


Figure 2-21. Standard deviation of normalized circulation and turbulent kinetic energy at different CADs for swirl measurement plane at 2500 rpm engine speed

2.3.3 Tumble measurement plane, 1500 rpm

Measurements are performed during the intake stroke at 121 crank angle degree and during the compression stroke at 192, 257 and 300 CADs. Similar to the results as observed in swirl measurement plane (at 1500 rpm), the rms values for the tumble plane at this engine speed are higher at 121 CAD and decay during the compression stroke, Mittal et al.⁶⁸ (2008).

Figure 2.22 shows the PDF plots of normalized circulation at different CADs with deactivated CMCV. As shown in the figure, the standard deviation of NC decreases from 121 CAD ($\sigma=219.76$ Hz) to 257 CAD ($\sigma=86.62$ Hz). It then increases to 210.69 Hz at 300 CAD. A similar pattern is observed when measurements are performed with activated CMCV with higher cycle-to-cycle variations compared to the deactivated CMCV; see Figure 2.23. These results show that cycle-to-cycle variation decreases from 121 CAD to 257 CAD, and then increases to CAD 300. Note that the CMCV effect is not significant on cycle-to-cycle variation at 300 CAD. Therefore, similar to the swirl plane measurements, CMCV has a profound effect on flow enhancement during the intake stroke; however, its effect decays during the late compression when compared to the deactivated CMCV.

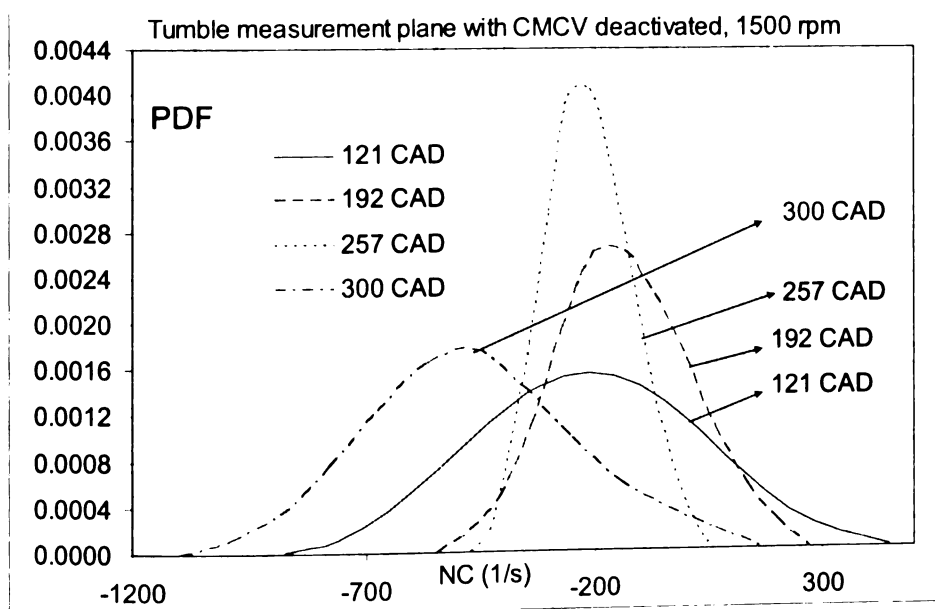


Figure 2-22. PDFs of normalized circulation at different CADs for tumble measurement plane with CMCV deactivated at 1500 rpm engine speed

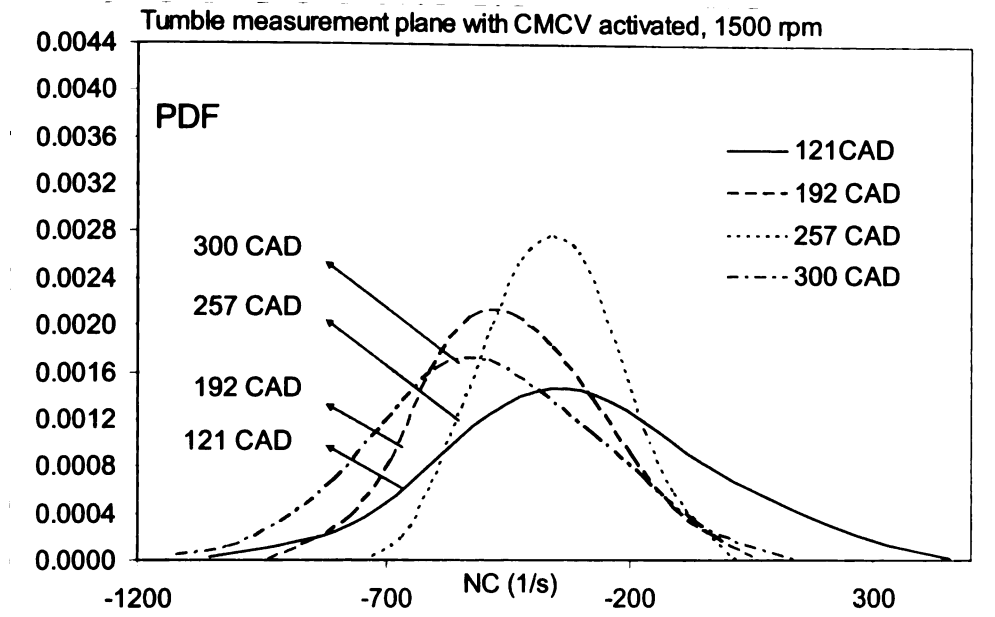


Figure 2-23. PDFs of normalized circulation at different CADs for tumble measurement plane with CMCV activated at 1500 rpm engine speed

Figure 2.24 shows the cycle-to-cycle variations characterized by the standard deviation of NC and averaged TKE for this tumble measurement plane at 1500 rpm engine speed with respect to the crank angle. The TKE decays from 121 to 257 CAD and then increases slightly to 300 CAD for both the cases. Joo et al.⁶⁹ (2004) also investigated the fact that the standard deviation of large- and small-scale variations was greater during the early intake and late compression when compared to the late intake and early compression process.

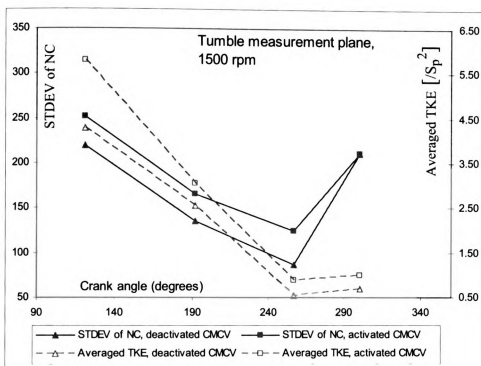


Figure 2-24. Standard deviation of normalized circulation and turbulent kinetic energy at different CADs for tumble measurement plane at 1500 rpm engine speed

2.3.4 Tumble measurement plane, 2500 rpm

Measurements are performed during the intake stroke at 138 and 171 crank angle degrees and during the compression stroke at 221 and 253 CADs with WOT. Figures 2.25 and 2.26 show the PDF plots of normalized circulation at these different crank angle degrees. For deactivated CMCV, the standard deviation of NC decreases from 138 CAD ($\sigma=264$ Hz) to 221 CAD ($\sigma=102.15$ Hz). It then increases to 253 CAD with the value of 139.38 Hz. These results show that cycle-to-cycle variation decreases from 138 to 221 CAD, and then increases to 253 CAD for deactivated CMCV. With activated CMCV, the standard deviation decreases from 138 to 253 CADs. The cycle-to-cycle variations show significant difference at 138, 171 and 221 CADs (higher with activated CMCV); however, it is only slightly higher at 253 CAD with activated CMCV. Therefore it can be

assumed that the CMCV effect reduces during the late compression to enhance the flow field inside an engine cylinder.

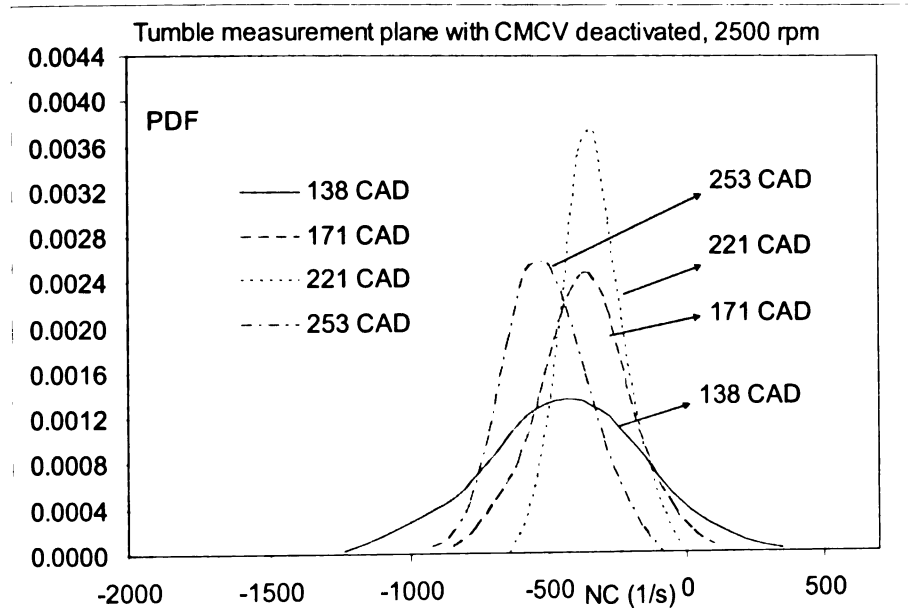


Figure 2-25. PDFs of normalized circulation at different CADs for tumble measurement plane with CMCV deactivated at 2500 rpm engine speed

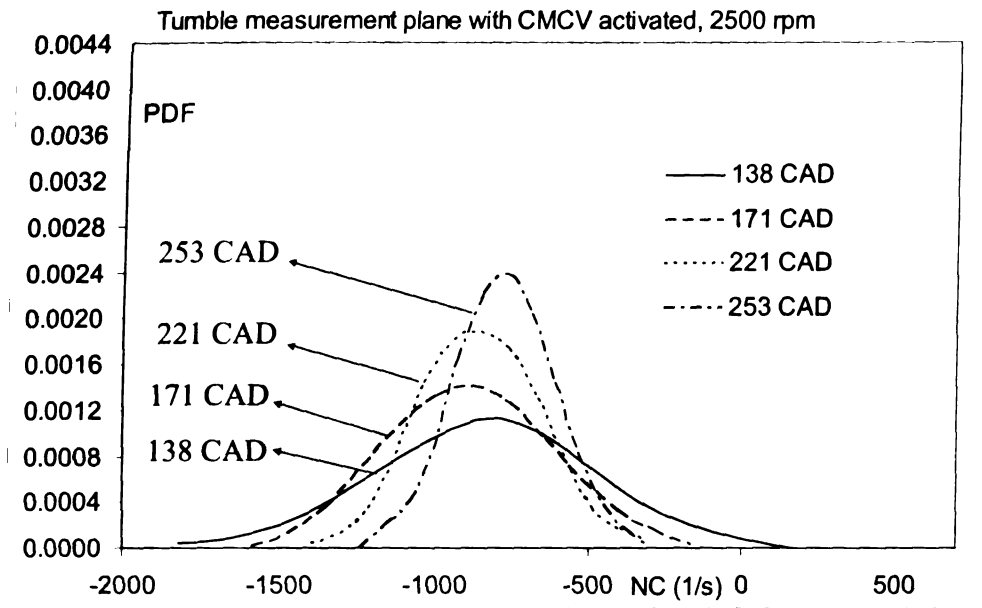


Figure 2-26. PDFs of normalized circulation at different CADs for tumble measurement plane with CMCV activated at 2500 rpm engine speed

Figure 2.27, when characterized by averaged TKE, shows consistently that cycle-to-cycle variations are higher with activated CMCV during the intake stroke and its effect decays during the late compression.

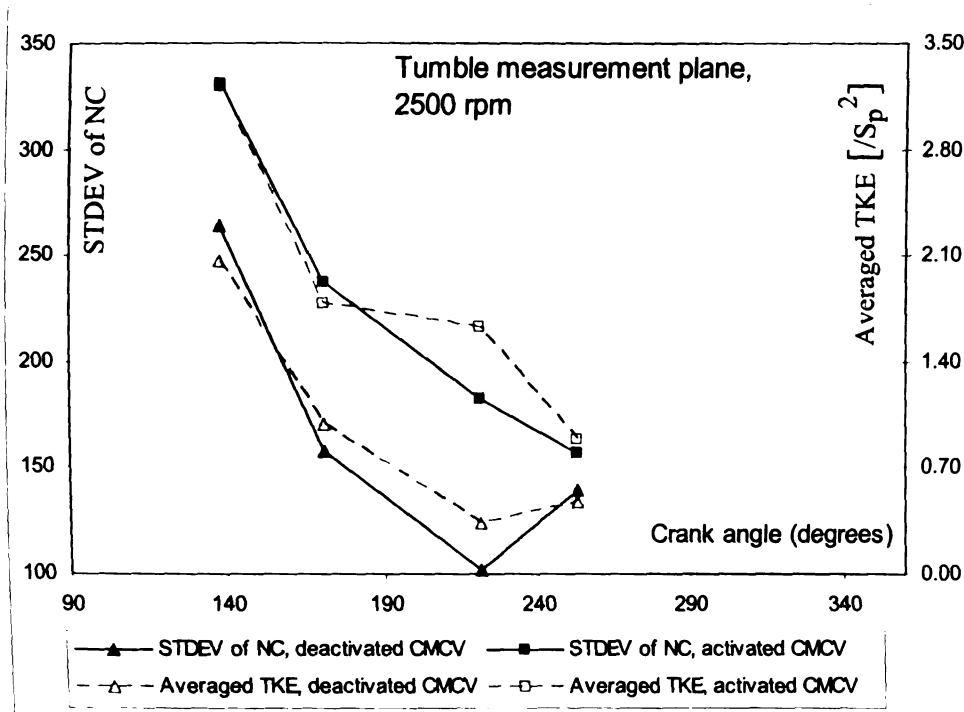


Figure 2-27. Standard deviation of normalized circulation and turbulent kinetic energy at different CADs for tumble measurement plane at 2500 rpm engine speed

2.4 Summary

The effects of charge motion control are presented on flow inside an IC engine cylinder. PDF plots of normalized circulation are computed for both tumble and swirl measurement planes at various CADs to characterize the cycle-to-cycle variations for deactivated and activated CMCVs. The effects of CMCV on in-cylinder flow measurements are summarized below.

- Swirl measurement plane at 1500 rpm: Cycle-to-cycle variation decreases from 121 CAD to 300 CAD with activated CMCV. Results show that CMCV has a considerable effect to enhance the flow field during the intake stroke; however, the effects are not significant during the compression stroke for the swirl measurement plane at 1500 rpm engine speed.
- Swirl measurement plane at 2500 rpm: With activated CMCV, the cycle-to-cycle variation decreases from 138 to 221 CAD, and then increases, only slightly, at 253 CAD.
- Tumble measurement plane at 1500 rpm: Results show that cycle-to-cycle variation decreases from 121 to 257 CADs, and then increases at 300 CAD with both the conditions, CMCV deactivated and CMCV activated. The effects of CMCV are significant to enhance the cycle-to-cycle variations except at 300 CAD.
- Tumble measurement plane at 2500 rpm: Cycle-to-cycle variation decreases from 138 to 221 CADs, and then increases at 253 CAD for deactivated CMCV. With activated CMCV, the cycle-to-cycle variation decreases from 138 CAD to 253 CAD. Similar to the results in the tumble measurement plane at 1500 rpm, it is found that the CMCV effect reduces during late compression to enhance the flow field inside the engine cylinder.

Insight on cycle-to-cycle variation, based on instantaneous measurements, is needed to optimize the engine design. The results of this study have particular significance on fuel-air mixing, and, therefore, on the combustion process. Results show that CMCV considerably enhances the flow field during the intake and compression strokes; however, the effects are not significant during the late compression. Therefore,

for this configuration, it can be assumed that CMCV enhances the fuel-air mixing more than the flame speed.

CHAPTER-3

IN-CYLINDER FLOW MEASUREMENT USING STEREOSCOPIC MOLECULAR TAGGING VELOCIMETRY

3.1 Introduction

The stereoscopic molecular tagging velocimetry technique is used to obtain the multiple point measurement of an instantaneous three-component velocity field inside the optical cylinder of an internal combustion engine assembly. The stereo imaging approach is commonly used earlier in the field of machine vision and also in PIV to obtain the three components of the displacement field, Bohl et al.³³ (2001). Two basic approaches: (i) lens translation and (ii) angular displacement have been utilized for this purpose. In the lens translation method, two detectors are placed side by side with the image planes parallel to the object plane; see Figure 3.1 [70]. More details of this method can be found in Arroyo and Greated⁷¹ (1991). The authors demonstrated the technique in the study of Rayleigh streaming flow in a rectangular tube. Bohl et al.³³ (2001) and Bohl⁷² (2002) used MTV with angular displacement method to measure the three-component velocity field generated by a propeller. The method is capable to provide nearly an entire overlap between the two images. The present work also takes the advantage of angular displacement method to measure an instantaneous three-component velocity field inside the optical engine cylinder. In this approach, the two cameras (left and right) view the same region of interest from different angles (see Figure 3.2 [70]), and the undelayed and

delayed images are captured at different crank angle positions using both the cameras. A new image processing technique is implemented to obtain the velocity data. The new algorithm is computationally less expensive and eliminates the need to specify the geometric details, as in the earlier works, to obtain the three-components of velocity. The geometric distortions are corrected by in-situ calibration. The procedure involves two major steps: (i) calibration process and (ii) data acquisition and reduction. In the calibration process, two images of a calibration target are used to obtain the mapping functions, which define the relationship between the positions in three-dimensional physical space (x, y, z) and the positions in two-dimensional image planes, (X_l, Y_l) and (X_r, Y_r) . The data reduction program finds the displacement of each grid point (laser intersection) between the undelayed and delayed images for each camera. Mapping functions and the two-dimensional image displacements are then used to obtain the three components of the displacement vectors, and hence the three components of the velocity field are obtained in a physical space coordinate system. RMS cyclic variations of the three-component velocity field and out-of-plane mean vorticity are presented inside an engine cylinder. Preliminary results show that cycle-to-cycle variations are more prominent in the velocity component perpendicular to the tumble plane, as opposed to the in-plane components. Such new insights will help better understand the details of these flows and further improve CFD models for IC engines.

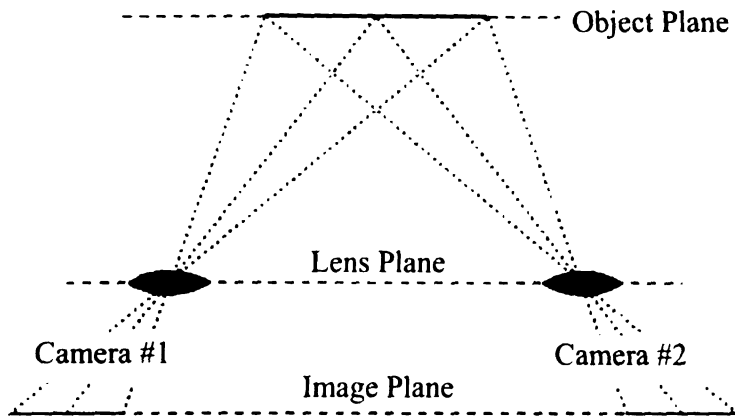


Figure 3-1. Basic configuration of lens translation method for stereoscopic imaging (Raffel et al., 1998)

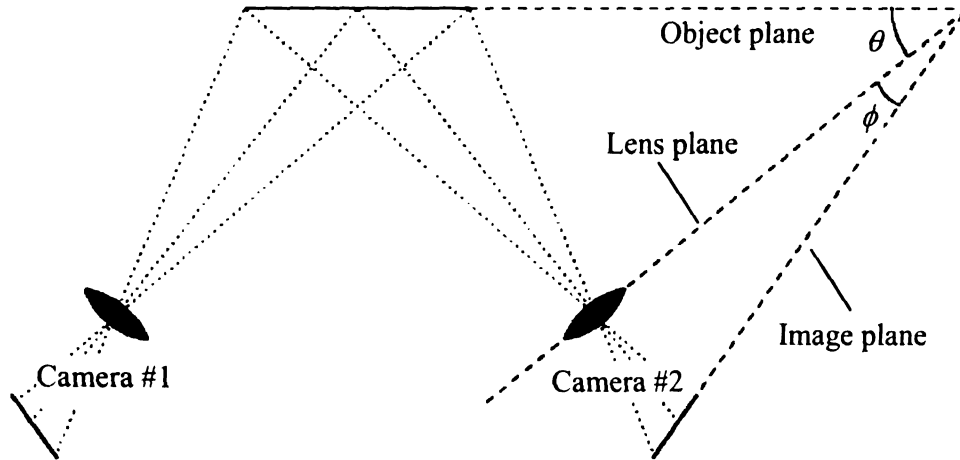


Figure 3-2. Basic configuration of angular displacement method for stereoscopic imaging (Raffel et al., 1998)

3.2 Experimental setup

The optical engine assembly used for the experiments represents a Ford 5.4 l 3-valve engine. It has a 90 mm bore diameter, 105.6 mm stroke, 169 mm rod length, and

two intake and one exhaust valves. Figure 3.3 shows the engine cylinder with the locations of tumble measurement plane and grid nodes, as well as the positions of intake and exhaust valves. As shown in the figure, the measurement plane is located more toward the right half of the engine cylinder. The top edge (of the plane) is located close to the Head Deck level. The grid spacing is about 4.3 mm (~ 64 pixels). The experiments are performed at the engine speed of 600 rpm. Measurements are taken at three different crank angle degrees positions, i.e., 90 CAD, 180 CAD, and 270 CAD. At 90 CAD, the piston is halfway to the stroke length and moving downwards to the BDC position during the intake stroke. 180 CAD represents the piston position at BDC during the intake stroke. Similarly, at 270 CAD the piston is halfway to the stroke length and moving upwards to the TDC position during the compression stroke. The working fluid in this experiment is nitrogen, and it was deoxygenated since the presence of oxygen quenches the phosphorescence of biacetyl.

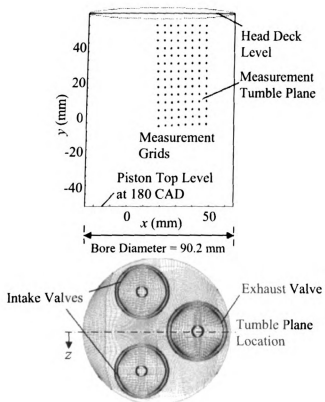


Figure 3-3. Tumble measurement plane inside an IC engine cylinder

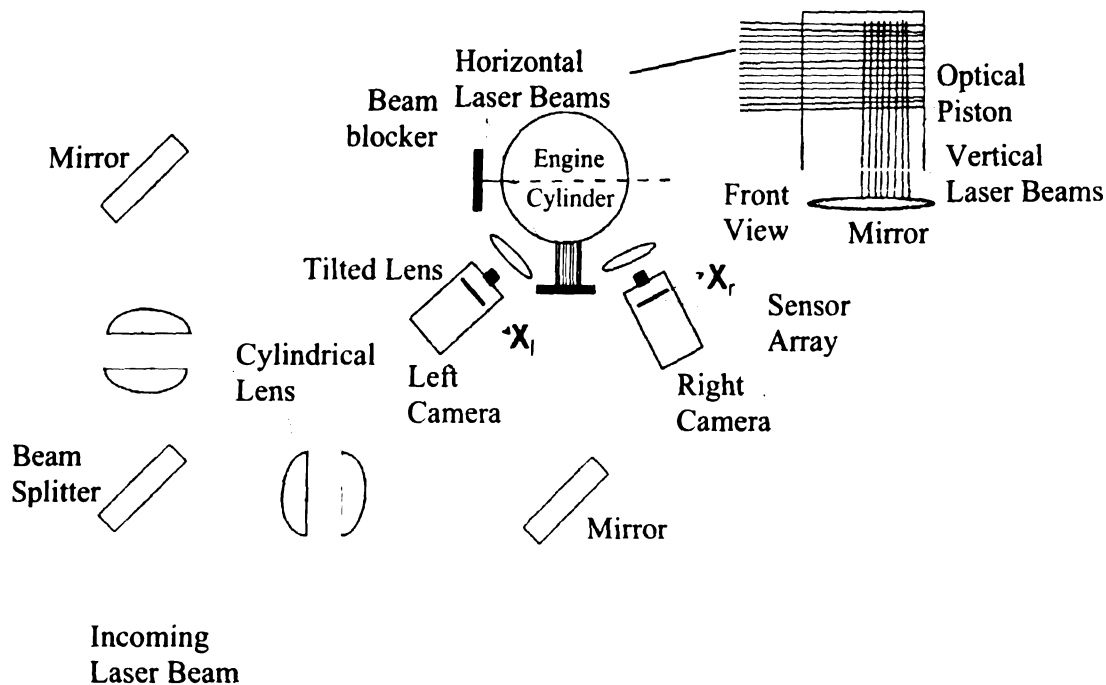


Figure 3-4. Schematic of SMTV optical setup

The optical setup for SMTV measurements inside the engine cylinder is shown in Figure 3.4. It consists of a pulsed ultraviolet laser (wavelength 308 nm, output energy of 250 mJ/pulse) whose light beam is used to create the grid pattern in the cylinder. The laser beam passes through numerous optical elements including a beam splitter and cylindrical lenses, which generate two light sheets propagating in the horizontal and vertical directions. As shown in the figure, the vertical laser beams are obtained using a mirror placed below the optical piston. Therefore, the horizontal laser beams are introduced into the cylinder through the optical cylinder and the vertical beams through the optical piston. Beam perforated blockers are used to transform the light sheets into sets of laser beams. As shown in Figure 3.3, the undelayed laser grid is formed in the x - y

plane and displaced with time because of fluid motion in the three-dimensional (x, y, z) physical space. Coordinate systems (X_l, Y_l) and (X_r, Y_r) are associated with the sensor planes (or image planes) of the left and right cameras (see Figure 3.4), respectively. The images at two successive time stamps are captured using LaVision's SprayMaster and Cooke Corporation's Sensicam camera systems. Each image is an 8-bit image with the size of 1024×1280 pixels. The imaging lens in front of each camera is mounted in a flexible arrangement that allows the lens axis to be tilted relative to the axis of the respective camera. This allows us to meet the Scheimpflug condition for optimal imaging at an oblique angle. For SMTV measurements, in this work, the angle between the two cameras was about 100 degrees and the exposure time was set to $30 \mu\text{s}$. Note that the delayed frame is referenced (in time) with respect to the undelayed frame by delay time.

3.3 Measurement Procedure

Fluid velocity measurements are acquired using stereoscopic molecular tagging velocimetry. Calibration and data reduction algorithms are used to obtain the three components of displacement vectors (Δx , Δy , and Δz) at each grid point in physical space using the recorded images. In the first step, a calibration target (see Figure 3.5) is used to determine the mapping functions. The target has a sufficient number of characteristic marks (typically circular) in all spatial coordinates (x, y, z) for SMTV with the known centroids in physical space. The calibration object is then positioned inside the engine cylinder. Images are taken using the camera system shown in Figure 3.4. The calibration program filters the two calibration images using threshold approach, and then captures the filtered edge data for each bright spot and fits the data into the circle equation to

obtain the actual centroids in the two image planes. A least-square fit algorithm with iterative procedure is used for this purpose, Spath⁷³ (1995).

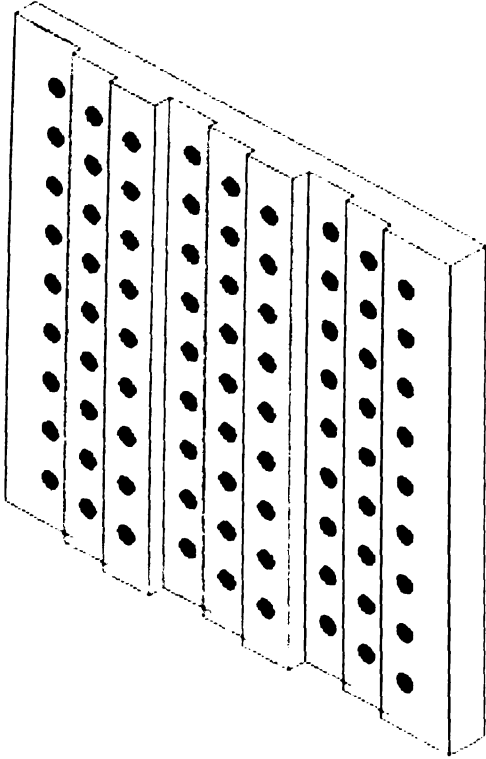


Figure 3-5. Calibration Target

Details of Spath [73] algorithm are presented below for completeness. In this method, the starting values $a^{(0)}$, $b^{(0)}$ and $r^{(0)}$ of the unknown center (a, b) and the unknown radius r are determined for the iterative procedure considering the circle equation in its nonparametric form;

$$(x - a)^2 + (y - b)^2 = r^2 \quad (3.1)$$

where (a, b) is the unknown center and r is the unknown radius of the circle. The objective function considered to be minimized is as follows:

$$\bar{S}(a, b, r) = \sum_{k=1}^n \left(r_k^2 - r^2 \right)^2 \quad (3.2)$$

$$\text{where, } r_k = \sqrt{(x_k - a)^2 + (y_k - b)^2}$$

Note that (x_k, y_k) is the filtered edge data in this work. The necessary conditions for a minimum of Equation 3.2 are,

$$\frac{\partial \bar{S}}{\partial r} = \frac{\partial \bar{S}}{\partial a} = \frac{\partial \bar{S}}{\partial b} = 0 \quad (3.3)$$

result in the following system of equations by setting $c = r^2 - a^2 - b^2$

$$\left(2 \sum_{k=1}^n x_k^2 \right) a + \left(2 \sum_{k=1}^n x_k y_k \right) b + \left(\sum_{k=1}^n x_k \right) c = \sum_{k=1}^n x_k (x_k^2 + y_k^2) \quad (3.4)$$

$$\left(2 \sum_{k=1}^n x_k y_k \right) a + \left(2 \sum_{k=1}^n y_k^2 \right) b + \left(\sum_{k=1}^n y_k \right) c = \sum_{k=1}^n y_k (x_k^2 + y_k^2) \quad (3.5)$$

$$\left(2 \sum_{k=1}^n x_k \right) a + \left(2 \sum_{k=1}^n y_k \right) b + nc = \sum_{k=1}^n (x_k^2 + y_k^2) \quad (3.6)$$

For nontrivial cases the desired starting values are obtained by solving Equations 3.4, 3.5 and 3.6 and hence,

$$a^{(0)} = a, \quad b^{(0)} = b, \quad r^{(0)} = \sqrt{c + a^2 + b^2} \quad (3.7)$$

The iterative solution is obtained by considering the circle in its parametric form; see Spath⁷³ (1995),

$$\begin{aligned} x &= a + r \cos z \\ y &= b + r \sin z \end{aligned} \quad (3.8)$$

and the objective function to be minimized is:

$$S(a, b, r, z_1, \dots, z_n) = \sum_{k=1}^n \left[(y_k - b - r \sin z_k)^2 + (x_k - a - r \cos z_k)^2 \right] \quad (3.9)$$

where z_1, \dots, z_n are the additional unknowns. The first part of the necessary conditions,

$$\frac{\partial S}{\partial a} = \frac{\partial S}{\partial b} = \frac{\partial S}{\partial r} = 0 \quad (3.10)$$

yields,

$$r = \left[n^2 \sum_{k=1}^n (x_k \cos z_k + y_k \sin z_k) - n \left(\sum_{k=1}^n x_k \sum_{k=1}^n \cos z_k + \sum_{k=1}^n y_k \sum_{k=1}^n \sin z_k \right) \right] / d \quad (3.11)$$

$$\text{where } d = n^2 \left[n - \frac{1}{n} \left(\left(\sum_{k=1}^n \cos z_k \right)^2 + \left(\sum_{k=1}^n \sin z_k \right)^2 \right) \right]$$

$$a = \frac{1}{n} \left(\sum_{k=1}^n x_k - r \sum_{k=1}^n \cos z_k \right) \quad (3.12)$$

$$b = \frac{1}{n} \left(\sum_{k=1}^n y_k - r \sum_{k=1}^n \sin z_k \right) \quad (3.13)$$

whereas the second part of the necessary condition, $\frac{\partial S}{\partial z_k} = 0$, gives

$$\tan z_k = \frac{y_k - b}{x_k - a} \quad (3.14)$$

With the known starting values $a^{(0)}$, $b^{(0)}$ and $r^{(0)}$, as described earlier, let $a^{(t)}$, $b^{(t)}$, and $r^{(t)}$, are determined at $t=0, 1, 2, \dots$. Equation 3.14 is used to determine $z_k^{(t)}$ and then $z_k^{(t)}$ is inserted into Equation 3.11 to get $r^{(t+1)}$, and finally $z_k^{(t)}$ and $r^{(t+1)}$ are inserted into Equations 3.12 and 3.13 to get $a^{(t+1)}$ and $b^{(t+1)}$. Once the locations of the characteristic marks in each image are determined, mapping functions are found such that any given point in the object space (x, y, z) is related to its corresponding location X, Y in the image plane of each camera. The obtained mapping functions are then used in a data reduction algorithm to obtain the velocity data.

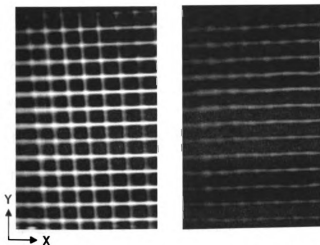


Figure 3-6. Undelayed (left) and delayed (right) images at 90 CAD SMTV measurements for right camera

Figure 3.6 shows the undelayed (averaged of 45 frames) and delayed images for the right camera at 90 CAD SMTV measurements. Similar images are obtained for the

left camera. A spatial correlation technique is used to obtain the grid displacements in the image planes, Gendrich and Koochesfahani²⁹ (1996). In this technique, a small window, referred to as the source window, is selected about a grid point in the tagged region in the undelayed image, and it is spatially correlated with a larger roam window in the delayed image. The two windows are centered at the same spatial location, and the roam window is large enough to encompass the grid displacement. A spatial correlation coefficient, R , is calculated between the two intensity fields of the source window (I_1) and the roam window (I_2) as a function of pixel displacement between them. The location of the peak in $R(X,Y)$ defines the displacement vector within one pixel, and calculated as follows, Gendrich and Koochesfahani²⁹ (1996):

$$R(X, Y) = \frac{\overline{I_s \cdot I_r} - \overline{I_s} \cdot \overline{I_r}}{\sigma_{I_s} \cdot \sigma_{I_r}} \quad (3.15)$$

where over bar refers to the expected value and σ denotes the standard deviation. The two subscripts, s and r , are used for the source and roam windows. The windows are selected to be squared shape. The various terms used in Equation 3.15 are as follows in terms of the pixel values;

$$\overline{I_s \cdot I_r} = \frac{1}{M \cdot N} \sum_{i=1}^M \sum_{j=1}^N I_s(i, j) I_r(i + X, j + Y), \quad (3.16)$$

$$\overline{I_s} = \frac{1}{M \cdot N} \sum_{i=1}^M \sum_{j=1}^N I_s(i, j), \quad (3.17)$$

$$\bar{I}_r = \frac{1}{M.N} \sum_{i=1}^M \sum_{j=1}^N I_r(i+X, j+Y), \quad (3.18)$$

$$\sigma_{I_S} = \sqrt{\frac{1}{M.N} \sum_{i=1}^M \sum_{j=1}^N (I_S(i, j) - \bar{I}_S)^2}, \quad (3.19)$$

$$\sigma_{I_r} = \sqrt{\frac{1}{M.N} \sum_{i=1}^M \sum_{j=1}^N (I_r(i+X, j+Y) - \bar{I}_r)^2} \quad (3.20)$$

Sub-pixel accuracy is obtained by using two-dimensional higher order polynomial fit. The 2-D polynomial function of p^{th} order is as follows;

$$R(X, Y) = \sum_{n=0}^p (a_{n,0} X^n Y^0 + a_{n-1,1} X^{n-1} Y^1 + \dots + a_{n,n} X^0 Y^n) \quad (3.21)$$

where the minimum number of required coefficients are $\frac{1}{2}(p+1)(p+2)$. A fourth order polynomial is used in this work to obtain the sub-pixel accuracy which requires a minimum of 15 data points from the correlation field. Since the sides of the square window have odd numbers of pixels to position the region symmetrically relative to the correlation peak, 5×5 pixels are considered for the fitting window. The location corresponding to the maximum correlation coefficient can be found by setting the first order partial derivatives of Equation 3.21 (with respect to X and Y) to be zero and subsequently solving the two algebraic equations; see Zheng and Klewicki⁶⁵ (2000),

$$\frac{\partial}{\partial X} \sum_{n=0}^p (a_{n,0} X^n Y^0 + a_{n-1,1} X^{n-1} Y^1 + \dots + a_{n,n} X^0 Y^n) = 0 \quad (3.22)$$

$$\frac{\partial}{\partial Y} \sum_{n=0}^p (a_{n,0} X^n Y^0 + a_{n-1,1} X^{n-1} Y^1 + \dots + a_{n,n} X^0 Y^n) = 0 \quad (3.23)$$

The above two equations are highly coupled nonlinear algebraic equations that have to be solved iteratively. This work utilizes a decoupled technique, as presented by Zheng and Klewicki⁶⁵ (2000), to solve Equations 3.22 and 3.23. This decoupled technique is an effort to seek a balance between accuracy and efficiency. As suggested by the authors, this decoupling results in about an order of magnitude decrease in the required CPU time. In this technique, the iterative solution of the maximum correlation point in two-dimensional distribution is replaced by solving two decoupled one-dimensional distributions. The assumption made here is that the maximum correlation point has been determined to within pixel accuracy. This is obtained using spatial correlation technique, as discussed earlier.

Three components of displacement in physical space at each grid node are obtained using the following system of equations, Soloff et al.⁷⁴ (1997).

$$\begin{pmatrix} \Delta X_l \\ \Delta Y_l \\ \Delta X_r \\ \Delta Y_r \end{pmatrix} = \begin{pmatrix} F_{Xl,1} & F_{Xl,2} & F_{Xl,3} \\ F_{Yl,1} & F_{Yl,2} & F_{Yl,3} \\ F_{Xr,1} & F_{Xr,2} & F_{Xr,3} \\ F_{Yr,1} & F_{Yr,2} & F_{Yr,3} \end{pmatrix} \begin{pmatrix} \Delta x \\ \Delta y \\ \Delta z \end{pmatrix} \quad (3.24)$$

where

$$F_{ij,1} = \left(\frac{\partial F_{ij}}{\partial x} \right), F_{ij,2} = \left(\frac{\partial F_{ij}}{\partial y} \right), \text{ and } F_{ij,3} = \left(\frac{\partial F_{ij}}{\partial z} \right)$$

and $i = X, Y; j = l, r$

The mapping functions derivatives need to be evaluated at each grid point (undelayed) in the physical space coordinate system (x, y, z) . The code calculates the laser grids

(undelayed) precisely for the two image planes and transforms the grids in physical space using cubic dependence on X and Y . Three-dimensional displacements are then obtained, solving Equation 3.24, using the concept of measurement plane pointers (MPPs), Naqwi⁷⁵ (2000).

Artificial images are used to obtain the accuracy of the mapping algorithm and data reduction program (Mittal et al.⁷⁶ (2009), Sadr et al.⁷⁷ (2008)). This is a common approach to establish and test the accuracy of the data reduction methods in optical flow velocimetry; for example see Raffel et al.⁷⁰ (1998). Gendrich and Koochesfahani²⁹ (1996), and Zheng and Klewicki⁶⁵ (2000), used this approach with a known spatial distribution of displacements in their MTV work. Initially laser grids (8×13) in physical space (x, y, z) are generated and then transformed through the mapping functions to obtain the corresponding grid nodes in the left and right camera planes. A three-component velocity field is then considered and the initial grid points are transformed by this velocity field to a new set of coordinates ($x+\Delta x, y+\Delta y, z+\Delta z$). These images are processed by calibration and data reduction algorithms to obtain the displacements. The obtained values are then used to estimate the accuracy of the measurement technique. The uncertainty (rms level) in determining the displacements for in-plane measurements is about 0.08 pixels. This is higher than the planar MTV (less than 0.05 pixels) due to the uncertainty associated with the calibration program. The uncertainty in the out-of-plane component is about 0.14 pixels. The errors in estimated mean and rms for 95% confidence bound (Benedict and Gould⁷⁸ (1996)) are about 2 μm and 1 μm for in-plane components, and 4 μm and 2 μm for out-of-plane component, respectively. Note that this

uncertainty (in μm) reduces with the improvement in spatial resolution of the cameras. Bohl et al.³³ (2001) reported the uncertainty (rms level) 0.05 pixels for in-plane measurements, about the same level for planar MTV, and 0.05-0.15 pixels in the out-of-plane component.

3.4 Experimental Results

SMTV tumble plane measurements, inside an internal combustion engine assembly, are presented for three different crank angle positions, i.e. 90 CAD, 180 CAD and 270 CAD. The averaged undelayed image, considered for the correlation to obtain the two-dimensional image displacements, is an average of 45 frames. 47 delayed frames are considered to obtain the instantaneous velocity fields at each crank angle position. Then, velocity statistics are calculated. The delay time between undelayed and delayed images is 10 μs , 15 μs and 30 μs for 90 CAD, 180 CAD and 270 CAD measurements, respectively. A large delay is needed for slower flows and vice versa. The piston is located at $y = -7.7$ mm for 90 and 270 CAD, while the position at 180 CAD is at $y = -52.3$ mm.

3.4.1 Flow field at 90 CAD

At 90 CAD, the piston is halfway to the stroke length and moving downward to the BDC position during the intake stroke. Figure 3.7 shows the ensemble-averaged velocity data (left), $\langle u \rangle$, $\langle v \rangle$ and $\langle w \rangle$, and out-of-plane mean vorticity (right) at 90 CAD. The velocity vectors in the plot represent the magnitude of $\langle u \rangle$ and $\langle v \rangle$ components, while color contours show the magnitude of the $\langle w \rangle$ component. The values of velocity magnitude vary from 6.7 to 53.1 m/s. They show the flow dominance in positive x

direction due to the fact that both the intake valves are positioned toward the left side of the cylinder and are open at 90 CAD. Also, it is to be noticed that the measurement plane is located more toward the right half of the cylinder. At 90 CAD, the piston is at its maximum speed, and because the piston area is substantially larger than the valve's open area, the velocity magnitudes are higher toward the upper section of the measurement plane. The out-of-plane velocity component changes the direction at several nodes, as expected. The out-of-plane mean vorticity at each grid node is calculated from the ensemble-averaged velocity field data. As shown in the figure, there are no significant rotations observed at 90 CAD measurements.

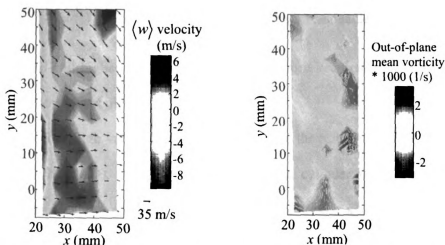


Figure 3-7. Ensemble-averaged velocity (left) and out-of-plane mean vorticity (right) at 90 CAD

The rms of u , v and w velocity components are shown in Figure 3.8. High variations are depicted for the out-of- plane velocity component due to the change in direction between several consecutive frames. Cycle-to-cycle variations are less for the v velocity component. In general, over the entire plane, the rms values in x direction are about a factor of 1-2 higher when compared to the rms values in y direction except

toward the right edge of the bottom half of the measurement plane. The slightly higher (rms) values in x direction are due to the higher velocity magnitudes observed in x direction. It is found that toward the right edge of the plane the velocity component, in the x direction, changes direction between several consecutive frames due to proximity to the cylinder wall. The flow is more uniform, temporally, in the y direction, and the velocity magnitude decreases from top to bottom due to reduced suction effects through the intake valves. This leads to higher rms values in the x direction compared to the rms values in the y direction toward the right edge of the bottom half of the plane. The rms plots of u , v and w velocity components also show that the estimation of $\langle v'^2 \rangle$ as $\left(\langle u'^2 \rangle + \langle w'^2 \rangle \right) / 2$ in equation 2.5 may not be a reasonable assumption. However, more detailed and higher order statistical information is required to obtain further insights on the nature of turbulence in this flow.

The high values of rms velocities show the turbulent nature of flow at this crank angle (90 CAD). The flow inside an engine cylinder is affected by several factors including engine geometry, speed, load, valve timing and lift. The obtained high rms values inside an IC engine cylinder are consistent with the work of Ismailov et al.⁴³ (2006) for both swirl and tumble measurement planes using well established two-component molecular tagging velocimetry technique. Zhang et al.⁷⁹ (1995) presented the high rms values under with/without swirl conditions. Jarvis et al.²⁴ (2006) reported the high values of rms cyclic variation during the intake stroke at 149 crank angle degree using digital particle image velocimetry technique. They showed relative decay in the

cyclic variations at further crank angle degrees during the intake stroke. Their results showed that the cyclic variations are less during the compression stroke (compared to the intake stroke). Bicen et al. ⁹ (1985) found high level of fluctuations in a reciprocating engine at several locations using the laser doppler velocimetry technique.

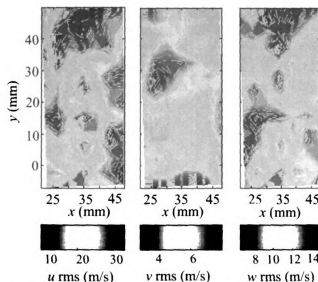


Figure 3-8. RMS of u , v and w velocity components at 90 CAD

3.4.2 Flow field at 180 CAD

180 CAD represents the piston location at BDC position during the intake stroke. Figure 3.9 shows the ensemble-averaged velocity field (left) and out-of-plane vorticity (right) data at 180 CAD measurements. The vectors in the ensemble-averaged velocity plot represent the magnitude of $\langle u \rangle$ and $\langle v \rangle$ components, while color contours show the magnitude of $\langle w \rangle$ component. The velocity magnitudes at this crank angle are smaller compared to the 90 CAD measurements and vary from 3 to 18 m/s. The smaller velocity magnitudes are due to reduced piston speed, momentarily at rest, at this crank angle (180

CAD). The mean values of $\langle u \rangle$, $\langle v \rangle$ and $\langle w \rangle$ velocity components over the plane are 8.2 m/s, -2.1 m/s and -0.5 m/s, respectively. The out-of-plane mean vorticity shows smaller magnitudes compared to 90 CAD measurements, as expected.

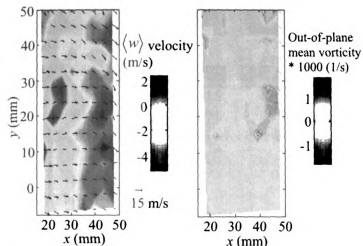


Figure 3-9. Ensemble-averaged velocity (left) and out-of-plane mean vorticity (right) at 180 CAD

Figure 3.10 shows the cycle-to-cycle variations for u , v and w rms velocity components. The values of u velocity rms vary from 3.6 to 16.2 m/s. Similar to 90 CAD measurements; high variations are observed for w velocity component and least for v velocity component. Results show that over the intake phase the relative cyclic variation decays. This is in agreement with the results of Jarvis et al.²⁴ (2006).

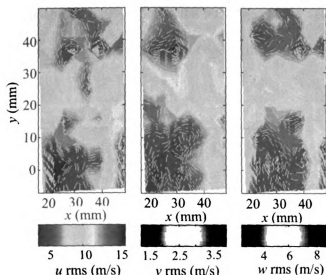


Figure 3-10. RMS of u , v and w velocity components at 180 CAD

3.4.3 Flow field at 270 CAD

At 270 CAD, the piston is halfway to the stroke length and moving upward to the TDC position during the compression stroke. Figure 3.11 shows the ensemble-averaged velocity field (left) and out-of-plane mean vorticity (right) data. The vectors in the ensemble-averaged velocity plot represent the magnitude of $\langle u \rangle$ and $\langle v \rangle$ components, while color contours show the magnitude of the $\langle w \rangle$ component. The mean velocity magnitudes vary from 2.9 to 9.9 m/s and are much smaller than the 90 CAD and 180 CAD measurements. The mean values of $\langle u \rangle$, $\langle v \rangle$ and $\langle w \rangle$ velocity components over the plane are 6.2 m/s, 1.3 m/s and -0.8 m/s, respectively. There are some rotations observed in the bottom half of the plane, centered toward the bottom-right corner. Figure 3.12, the rms plots of the three velocity components, shows that at this stage flow is less turbulent. The values of u velocity rms vary from about 2 to 4 m/s except at the right edge of the plane. Similarly, the rms of v velocity varies from about 0.6 to 1.6 m/s and shows more

cycle-to-cycle variations at the left edge. The w velocity rms varies from about 1.5 to 2.5 m/s except at the bottom right of the plane.

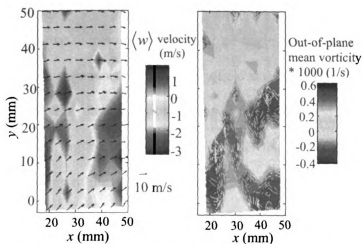


Figure 3-11. Ensemble-averaged velocity and out-of-plane mean vorticity at 270 CAD

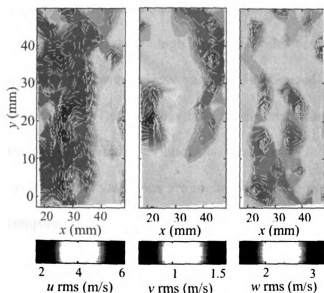


Figure 3-12. RMS of u , v and w velocity components at 270 CAD

3.5 Summary

The application of the Stereoscopic Molecular Tagging Velocimetry technique for the measurements in highly transient, three-dimensional flows inside an internal combustion engine is presented. In this technique images of a tagged region obtained from two cameras, positioned at an angle relative to each other, are used to obtain the three components of the velocity field at each image instance. The images are analyzed to obtain the three components of the velocity field inside an IC engine cylinder. The present implementation of SMTV has the advantage that it does not require detailed modeling of the system geometry. The uncertainties in determining the displacements for in-plane components and the out-of-plane component are about 0.08 pixels and 0.14 pixels, respectively. The three-component velocity field, out-of-plane vorticity and cycle-to-cycle variations are presented for tumble plane measurements at three different crank angle positions (90, 180 and 270 CAD).

Results show high cycle-to-cycle variations in the out-of-plane velocity component; however, less variation is observed in the velocity component along the cylinder axis. The flow has fully three-dimensional unsteady behavior during the intake stroke; however the variations are less during the compression stroke. At 90 CAD the cycle-to-cycle variations are higher for all the three velocity components (u , v and w), compared to the measurements at 180 CAD when the piston is at BDC position during the intake stroke. In this work, the SMTV images are captured using LaVision's SprayMaster and Cooke Corporation's Sencam camera systems. Each image is an 8-bit resolution image with the size of 1024×1280 pixels. In order to meet strict exhaust

emissions and fuel efficiency standards, improved numerical simulations, supported by this type of spatially and temporally resolved experimental studies, are desirable.

CHAPTER-4

INTAKE MANIFOLD AND IN-CYLINDER FLOW MEASUREMENTS INSIDE AN INTERNAL COMBUSTION ENGINE ASSEMBLY

4.1 Introduction

It has been acknowledged for a long time that the flow field inside an IC engine cylinder is highly complex, turbulent, and three-dimensional. It is the most important factor controlling the combustion process, Heywood¹ (1987). Therefore a thorough understanding of the highly unsteady in-cylinder flow is necessary to optimize the engine design. In general, there are two approaches to investigate the in-cylinder flows in an IC engine assembly: (i) laser diagnostic methods and (ii) multi-dimensional numerical simulations.

The studies of laser diagnostic in-cylinder flow measurements are performed using laser doppler velocimetry, particle image velocimetry and molecular tagging velocimetry. Recently, Mittal et al.⁷⁶ (2009) used a stereoscopic molecular tagging velocimetry technique to obtain the three-component velocity field inside an IC engine cylinder. However, it is to be noticed that the experimental techniques (either PIV or MTV) of in-cylinder flow analysis are limited to velocity field measurements over a plane and do not provide detailed flow information over the complete volume of the engine cylinder. It is the multi-dimensional numerical simulations that provide this information, and offer significant time and cost savings to design the engine with improved performance. With the advent of powerful computers, several studies of in-

cylinder flow have been reported using multi-dimensional numerical simulations, i.e. Luo et al.⁴⁴ (2003), Shojaeefard and Noorpoor⁴⁵ (2008). However, boundary conditions are assumed in the modeling efforts. Experimental information that can provide the real-time boundary conditions is necessary to perform more accurate multi-dimensional numerical simulations of complex in-cylinder flows. This may also require a validation with experimental results, i.e. PIV or MTV/SMTV in-cylinder flow measurements.

In this work, an experimental study is performed to measure the velocity and pressure inside the intake manifold of a motored internal combustion engine assembly. The aim of this work is to provide the data of real-time boundary conditions for more accurate multi-dimensional numerical simulations of in-cylinder flows in an IC engine. The geometry of the intake manifold is simplified for this purpose. A hot-wire anemometer and a piezoresistive absolute pressure transducer are used to measure the velocity and pressure, respectively, over a plane inside the circular section of the intake manifold. In addition, pressure measurements are performed at two locations over an elliptical plane near the intake port. In-cylinder pressure is measured using a piezoelectric type pressure transducer. Experiments are performed at 900 and 1200 rpm engine speeds. Phase-averaged velocity and pressure profiles are then calculated from the instantaneous measurements. Results of velocity and pressure measurements show the oscillatory nature of flow inside the intake manifold. In addition, in-cylinder flow measurements are performed to validate the modeling efforts. The stereoscopic molecular tagging velocimetry technique is used for this purpose to obtain the multiple point measurement of an instantaneous three-component velocity field inside the engine cylinder.

4.2 Experimental setup

The internal combustion engine assembly used for the experiments is a three-valve, two intake and one exhaust, 0.675 l single-cylinder engine. It has a 90 mm bore diameter, 105.6 mm stroke length and 169 mm rod length. Figure 4.1 shows the experimental setup, which is used to measure the instantaneous velocity and pressure profiles inside the intake manifold. Experiments are performed at 900 and 1200 rpm engine speeds. This work is aimed to provide the necessary boundary conditions for multi-dimensional numerical simulations of in-cylinder flows. Due to this, the geometry of the intake manifold is simplified, i.e. intake plenum is removed and the circular geometry is considered. However, near the intake port, there is a gradual transition from elliptical to circular section; see Fig. 4.1. Surface models of this elliptical part and the intake port section are under development using 3D laser scanning. Figure 4.2 shows the geometry of the intake port with two intake valves.

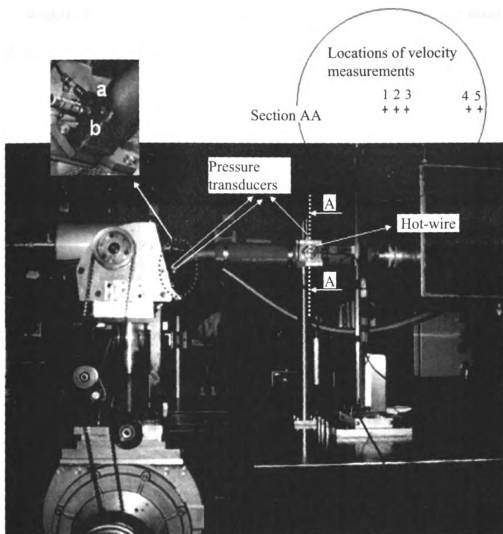


Figure 4-1. Experimental rig showing measurement planes and locations inside the intake manifold for flow measurements

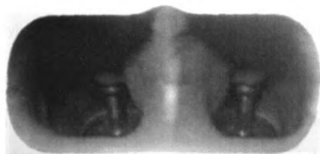


Figure 4-2. Intake port geometry

Velocity measurements inside the intake manifold may be performed using two broad approaches: (i) methods involving the use of a sensor within the flow under investigation and (ii) optical methods. An earlier approach is considered in this work. A constant temperature hot-wire anemometer is used for this purpose to measure the axial-velocity profiles. Note that the hot-wire anemometer is a purely analog device and offers a very high frequency response compared to the optical methods. Due to this, it can provide a continuous boundary condition data for numerical simulations of complex in-cylinder flows. Also, it is simple to use and inexpensive compared to the optical methods. Measurements are performed over a plane in circular section (radius 26 mm) at few radial locations; see Fig. 4.1. As shown in the figure, location 2 is at the center of the plane. Locations 1 and 3 are each 3 mm apart from the center. Similarly, locations 4 and 5 are at 21 and 24 mm from the center, respectively. A honey comb section is placed between the intake manifold and the tank which can be used to premix the MTV molecules into the working fluid. This is to make the flow more uniform and one-dimensional (inside the intake manifold). Working fluid in this experiment is nitrogen due to the fact that similar setup is used for the in-cylinder flow measurements (using stereo MTV). Note that the presence of oxygen quenches the MTV chemicals and hence nitrogen is used.

Hot-wire anemometer is extensively used by several researchers in earlier in-cylinder flow studies; see Hassan and Dent⁵ (1971) and Parsi and Daneshyar⁸⁰ (1989). Witze⁷ (1980) compared the in-cylinder flow measurement results of HWA and LDV in a motored reciprocating engine. The author mentioned that accurate in-cylinder hot-wire measurements are only possible for the intake and exhaust strokes. Therefore, inside the intake manifold, HWA can be used more comfortably and accurately where the property

variations are even less significant. One of the limitations using a hot-wire anemometer is that it does not resolve the flow direction. However, it can often be resolved by intuition and geometric considerations. Fortunately, in engine intake manifold, the direction of flow during the intake stroke is known. It is then reversed when velocity magnitude reaches to zero and so on.

The calibration of hot-wire used in this work is performed in air due to unavailability of calibration facility in nitrogen. Note that the fluid mechanic properties of air are in close agreement with nitrogen. Fluid velocity is determined using King's law which states that

$$e^2 = A + Bu^{0.45} \quad (4.1)$$

where A and B are the calibration constants, e is the hot-wire response and u is the fluid velocity.

Pressure measurements over the same plane (which is considered for velocity measurements) are performed using a Kistler piezoresistive type absolute pressure transducer. In addition, pressure measurements over an elliptical plane near the intake port are also performed at couple of locations (centers of major and minor axes; locations a and b , respectively); see Fig. 4.1. This is due to the complex transition of intake manifold geometry from elliptical to circular section near the intake port and hence to verify the pressure profiles in numerical simulations where boundary conditions will be provided at the circular measurement plane. Data acquisition is performed using a high speed combustion analysis system (CAS) with two crank angle degree resolution; see Fig. 4.3 for CAS setup. Sampling was triggered by a TTL pulse generated by the engine encoder.

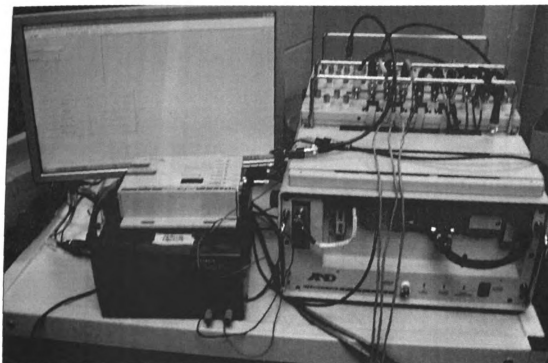


Figure 4-3. Combustion analysis system (CAS) used for intake manifold flow measurement

Fluid velocity measurements inside the engine cylinder are performed using stereoscopic molecular tagging velocimetry. The experimental setup is shown in Fig. 4.4. Figure 4.5 shows the schematic of the engine cylinder with the locations of tumble measurement plane and laser grids. The measurement plane symmetrically bisects the two intake valves. The grid spacing is about 9 mm in the x direction and 5.7 mm in the y direction. Experiments are performed at 900 and 1200 rpm engine speeds with similar conditions used for the intake manifold flow measurements. As discussed earlier, the working fluid in this experiment is nitrogen.

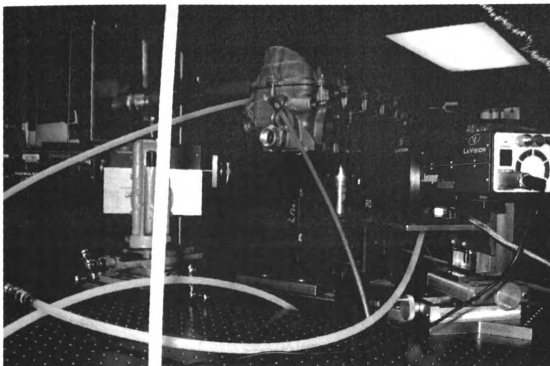


Figure 4-4. Experimental rig for in-cylinder flow measurement using stereo MTV

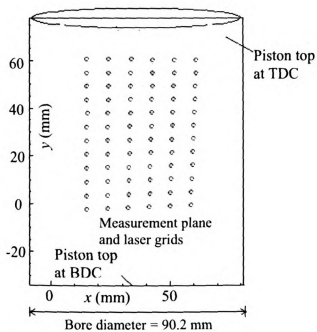


Figure 4-5. Tumble measurement plane inside the engine cylinder

The optical setup used for the SMTV measurements inside the engine cylinder is shown in Figure 4.6. As discussed in Chapter 3, it consists of a pulsed ultraviolet laser with wavelength 308 nm and output energy 300 mJ/pulse whose light beam is used to create the grid pattern in the cylinder. The laser beam passes through numerous optical elements including a beam splitter and cylindrical lenses, which generate two light sheets propagating in the horizontal and vertical directions. Beam perforated blockers are used to transform the light sheets into sets of laser beams. The undelayed laser grid is formed in the x - y plane and displaced with time because of fluid motion in the three-dimensional (x, y, z) physical space. Coordinate systems (X_l, Y_l) and (X_r, Y_r) are associated with the sensor planes of the left and right cameras (see Figure 4.6), respectively. The images at two successive time stamps are captured using LaVision's Imager Intense CCD cameras (both for the left and right cameras) with intensified relay optics. Each image is a 12-bit resolution image with the size of 1376×1040 pixels. The imaging lens in front of each camera is mounted in a flexible arrangement that allows the lens axis to be tilted relative to the axis of the respective camera. This allows us to meet the Scheimpflug condition for optimal imaging at an oblique angle. The angle between the two cameras was set to 90 degrees.

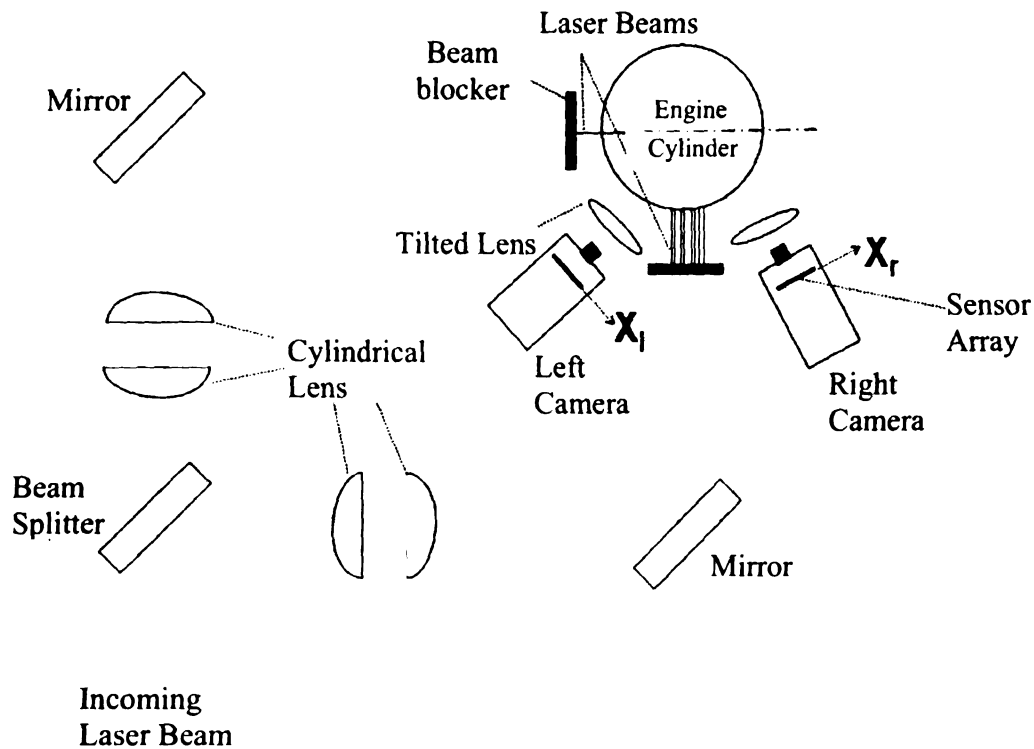


Figure 4-6. Schematic of SMTV optical setup

4.3 Experimental Results

Velocity and pressure measurements are presented inside the intake manifold of a motored internal combustion engine assembly at 900 and 1200 rpm engine speeds. 150 consecutive cycles are recorded; then, velocity and pressure statistics are calculated. In all the figures, zero crank angle degree represents the start of the intake stroke, i.e. piston at the top dead center of the intake. At 180 CAD piston is at the bottom dead center during the intake stroke. Similarly, 360 CAD represents the TDC of the compression stroke. SMTV in-cylinder flow measurements are presented at various crank angle degrees during the intake and compression strokes at 900 and 1200 rpm engine speeds. The

averaged undelayed image, considered for the correlation to obtain the two-dimensional image displacements, is an average of 50 frames. 100 delayed frames are considered to obtain the instantaneous velocity fields at each crank angle position. Then, velocity statistics are calculated. The delay time between undelayed and delayed images vary between 12-26 μ s. A large delay is needed for slower flows and vice versa.

4.3.1 Flow measurements at 900 rpm engine speed

Flow measurements are presented at 900 rpm engine speed. Figure 4.7 shows the averaged in-cylinder pressure trace considering 150 consecutive cycles. The peak in-cylinder pressure is about 21.2 bars and located at the top dead center of the compression stroke due to the fact that engine is operated under motoring conditions, i.e. without combustion.

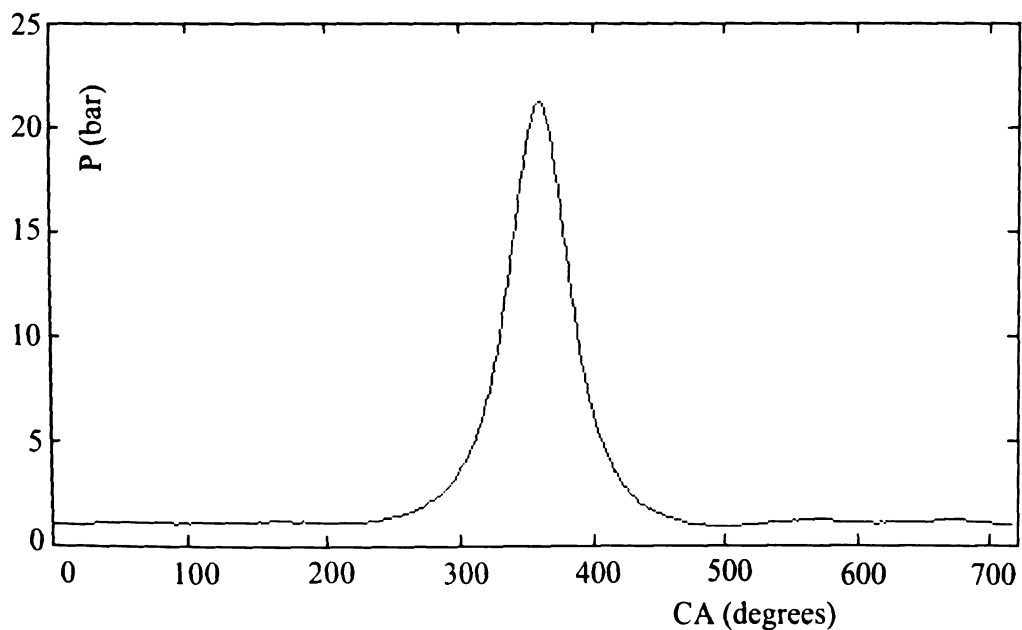


Figure 4-7. Averaged in-cylinder pressure trace at 900 rpm engine speed

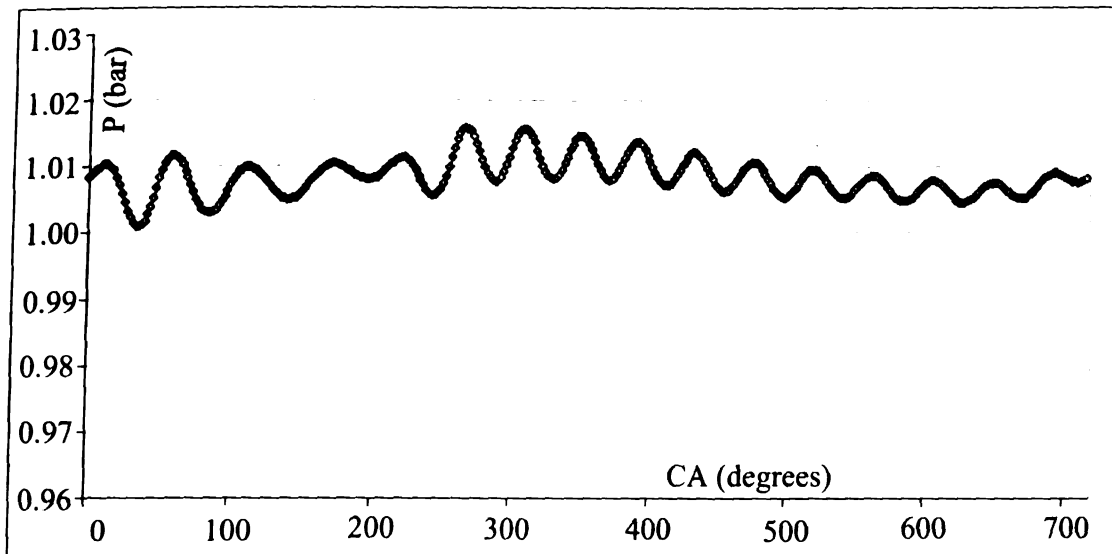


Figure 4-8. Averaged pressure trace at the circular section of the intake manifold at 900 rpm engine speed

Figure 4.8 shows the averaged pressure profile at the circular section (as discussed earlier) inside the intake manifold of the engine assembly. The pressure profile clearly shows the oscillatory nature of flow inside the intake manifold. The minimum pressure is about 100 kPa and it is observed during the intake stroke, as expected. The peak pressure during the cycle is about 101.6 kPa.

Figure 4.9 shows the velocity profiles over the circular section at radial locations 2, 3, 4 and 5 inside the intake manifold. The peak velocity is about 9 m/s during the intake stroke at 50 crank angle degrees, and then decreases to 5.6 m/s at 70 CAD. Due to maximum piston speed at 90 CAD, it then increases again to 9 m/s at this crank angle. Note that the velocity magnitudes are higher at the center of the plane during the forward flow; however, during the back flow magnitudes are relatively higher near the wall. This shows that the flow characteristics inside the intake manifold are strongly depend on piston motion and intake valve timing and lift; see Figure 4.10 for intake valve lift profile

and its first derivative. During the complete engine cycle, oscillating peak of the velocity magnitude decreases traversing from intake to exhaust stroke and it is close to zero at the end of the exhaust stroke. In addition, Figure 4.11 shows the averaged velocity data during the intake stroke (at various CADs) with respect to the radial distance from the center of the plane. Note that the radial positions in the figure at 0, 3, 21 and 24 mm represent the measurement locations 2, 3, 4, and 5, respectively. The velocity at the wall (26 mm from the center), which is assumed to be zero due to no-slip condition, is also plotted in the figure.

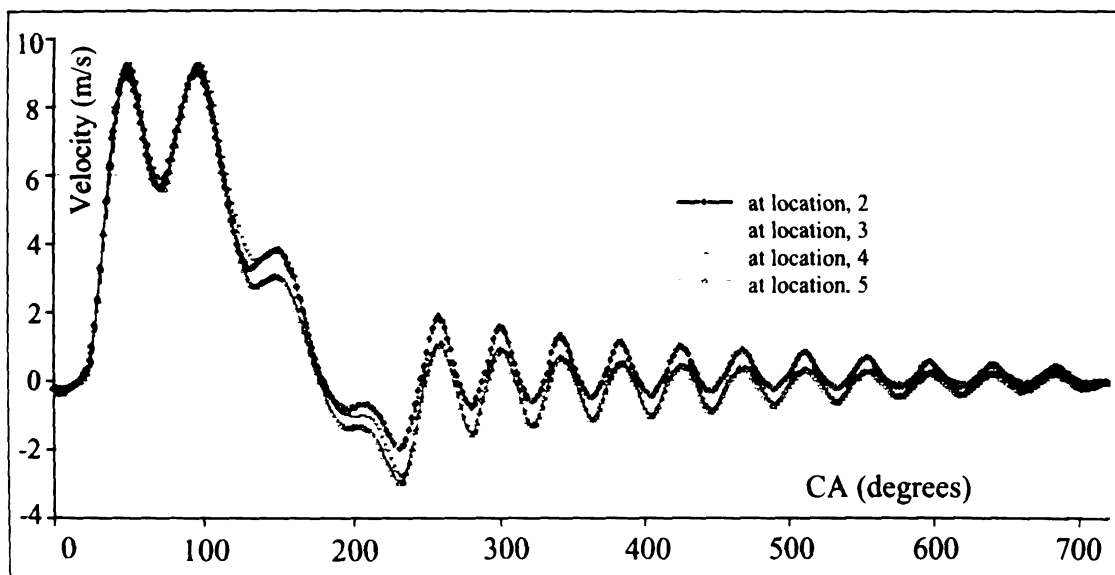


Figure 4-9. Averaged velocity profile at different radial locations in the circular section of the intake manifold at 900 rpm engine speed

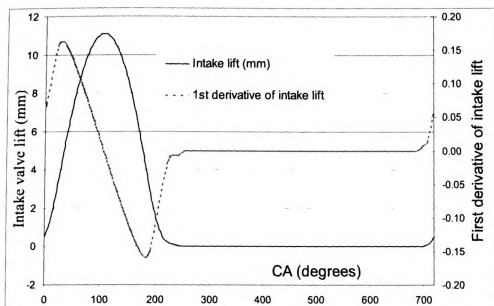


Figure 4-10. Intake valve lift and its first derivative

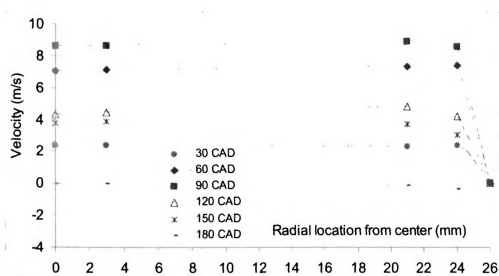
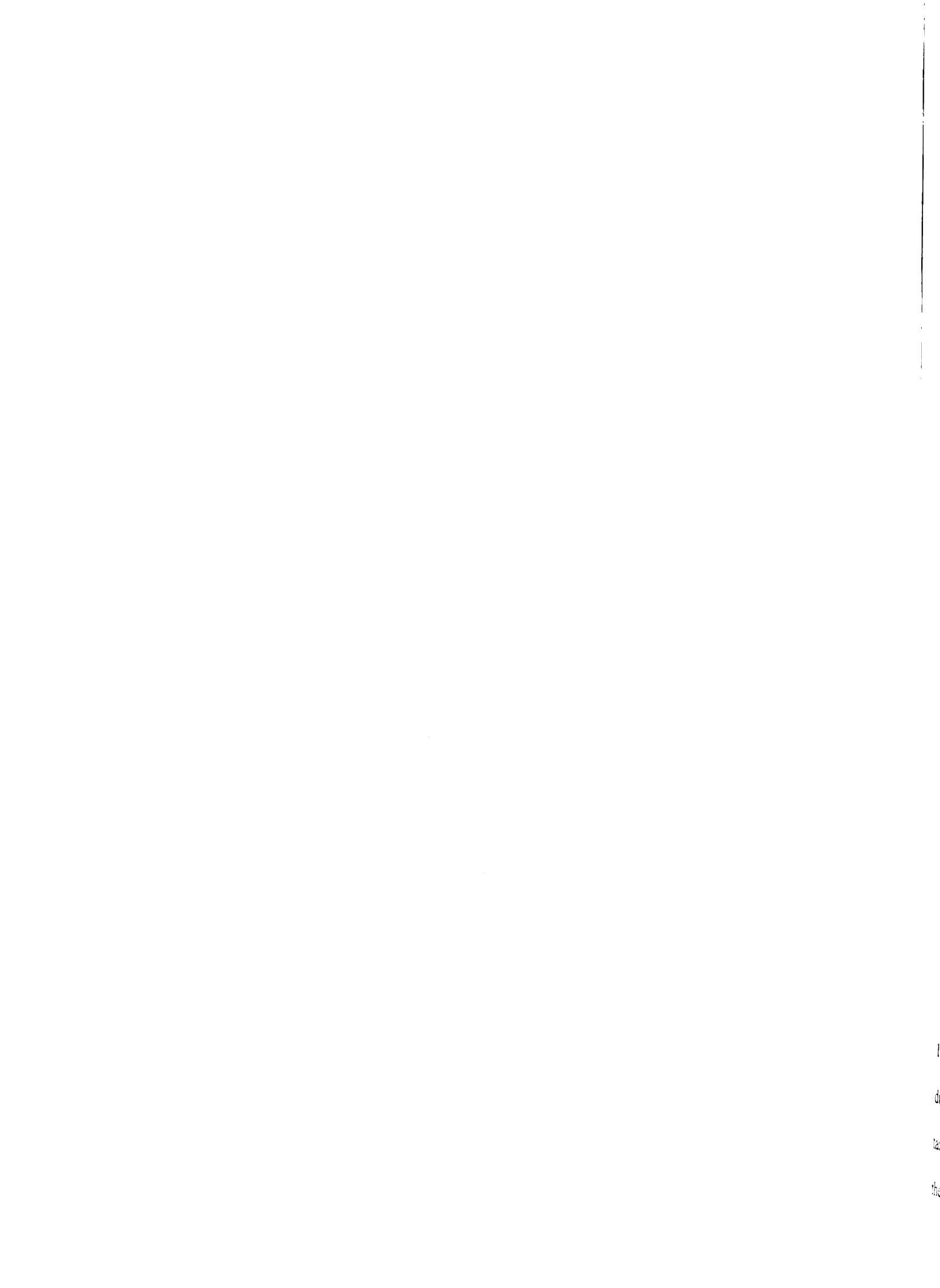


Figure 4-11. Averaged velocity at different radial locations 2 (0 mm), 3 (3 mm), 4 (21 mm), 5 (24 mm) and at the wall (26 mm) during the intake stroke at various crank angle degrees; 900 rpm engine speed

Figure 4.12 shows the averaged pressure profiles over the elliptical section, near the intake port, at locations *a* and *b*. Averaged pressure profile over the circular plane is



also shown in the figure for comparison. As expected, during the forward flow, pressure is relatively higher at the circular plane compared to the locations *a* and *b* over the elliptical plane near the intake port. However, it is to be noticed that pressure is slightly higher at location *a* compared to location *b*. This may be due to the intake port geometry (see Fig. 4.2) which shows that flow is relatively stagnant at location *a* compared to location *b*. Similarly, during the backflow, due to the reversal of flow direction, pressure magnitudes are higher at elliptical plane locations (*a* and *b*) compared to the values at circular plane.

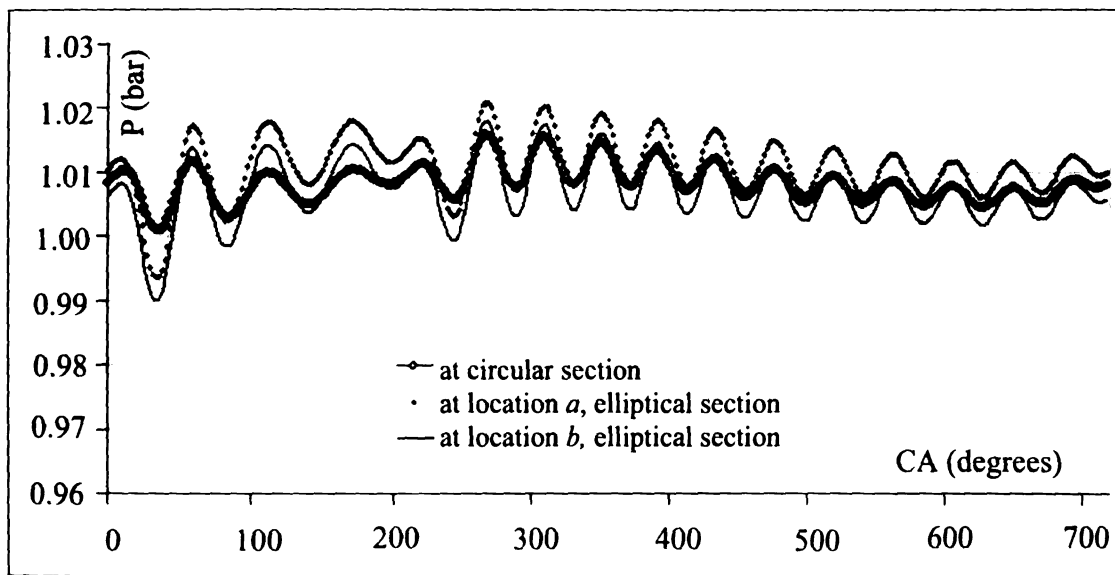


Figure 4-12. Averaged pressure trace at the circular and elliptical sections of the intake manifold at 900 rpm engine speed

In-cylinder flow measurement at 900 rpm engine speed are performed at 120 and 140 crank angle degrees during the intake stroke and 260 and 280 crank angle degrees during the compression stroke. In the first step, calibration images of the calibration target are obtained using both left and right cameras. 150 images are recorded and then the averaged calibration images are obtained; see Figure 4.13 for the left and right

calibration images, respectively. The centroids of each bright spot are determined using a least-square fit algorithm with an iterative procedure, and then the mapping functions are obtained such that any given point x in the object space is related to its corresponding location X, Y in the image plane. In the second step, undelayed and delayed MTV images are captured at different crank angle positions inside the optical engine assembly. 50 undelayed frames are considered to obtain the averaged undelayed image at each crank angle position for both the cameras. 100 delayed frames are recorded to obtain the instantaneous velocity fields at each crank angle position. The delay time between undelayed and delayed images vary between 12-26 μs for the measurements at 900 rpm engine speed. Figure 4.14 shows the averaged undelayed and a delayed frame for both the cameras at 120 crank angle degree. The two-dimensional image displacements are then calculated and thus the three-components of velocity (or displacement) are obtained in physical space; see Chapter 3 for more details about the technique. Then the velocity statistics are calculated.

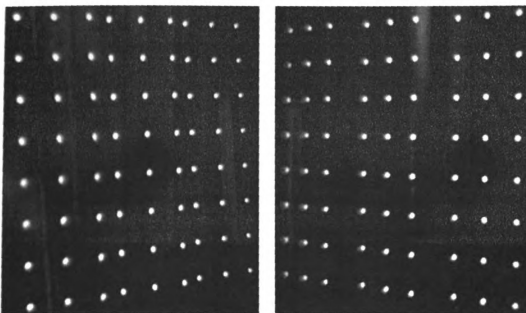


Figure 4-13. Calibration images of left (left) and right (right) cameras

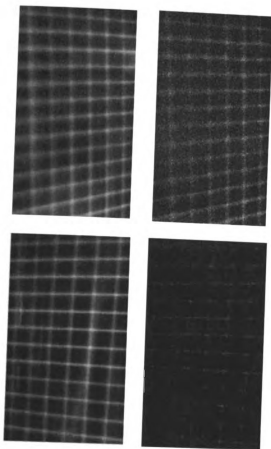


Figure 4-14. Undelayed (left) and delayed (right) images at 120 crank angle degree for left (upper) and right (lower) cameras at 900 rpm engine speed

Figure 4.15 shows the ensemble-averaged velocity data (left), $\langle u \rangle$, $\langle v \rangle$ and $\langle w \rangle$, and rms of velocity (right) at 120 crank angle degree during the intake stroke at 900 rpm. The velocity vectors in the ensemble-averaged plot represent the magnitude of $\langle u \rangle$ and $\langle v \rangle$ components, while color contours show the magnitude of the $\langle w \rangle$ component. Due to the fact that both the intake valves are open, the velocity magnitudes are higher toward the upper section of the measurement plane. The axial component of velocity, $\langle v \rangle$, show the flow dominance in negative y direction due to the downward piston motion at this crank angle. The high rms values show that the flow is highly turbulent at this crank angle

during the intake stroke. It is as high as 26 m/s toward the upper right section of the measurement plane.

Figure 4.16 shows the ensemble-averaged velocity data (left), $\langle u \rangle$, $\langle v \rangle$ and $\langle w \rangle$, and rms of velocity (right) at 140 crank angle degree during the intake stroke. Similar to the measurements at 120 CAD, the axial component of velocity shows the flow dominance in negative y direction and its magnitude decays traversing from upper to lower section of the measurement plane. The rms values are higher than 18 m/s toward the upper section of the plane. However, note that it decreases compared to the measurements at 120 CAD. This shows that the cycle-to-cycle variations decay during the intake stroke.

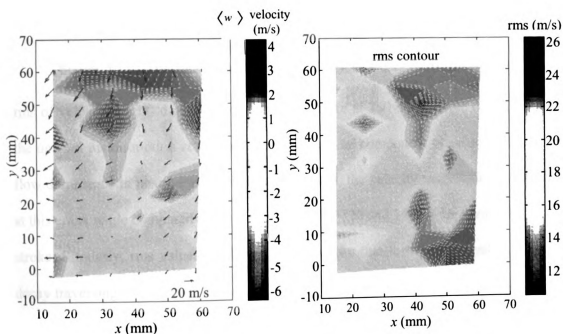


Figure 4-15. Ensemble-averaged velocity field (left) and velocity rms (right) at 120 crank angle degree and 900 rpm engine speed

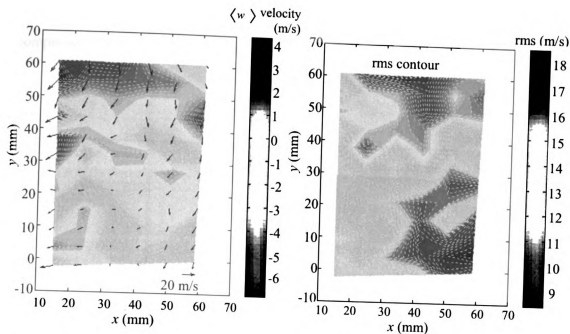


Figure 4-16. Ensemble-averaged velocity field (left) and velocity rms (right) at 140 crank angle degree and 900 rpm engine speed

Figure 4.17 shows the ensemble-averaged velocity data (left), $\langle u \rangle$, $\langle v \rangle$ and $\langle w \rangle$, and rms of velocity (right) during the compression stroke at 260 crank angle degree. Due to the upward piston motion at this crank angle, the axial component of velocity shows the flow dominance in positive y direction. As expected, the velocity magnitudes are smaller at this crank angle compared to the measurements at 120 and 140 CADs during the intake stroke. Similarly, rms values are lower, which shows that the cycle-to-cycle variations decay traversing from intake to compression stroke. The peak of rms values is about 4.5 m/s at this crank angle. The ensemble-averaged velocity (left), $\langle u \rangle$, $\langle v \rangle$ and $\langle w \rangle$, and rms of velocity (right) during the late compression at 280 CAD are shown in Figure 4.18. It is to be noticed that the rms values increases during the late compression. It is as high as 5.5 m/s at this CAD. Joo et al.⁶⁹ (2004) also investigated the fact that the standard deviation

of large- and small-scale variations was greater during the early intake and late compression compared to the late intake and early compression.

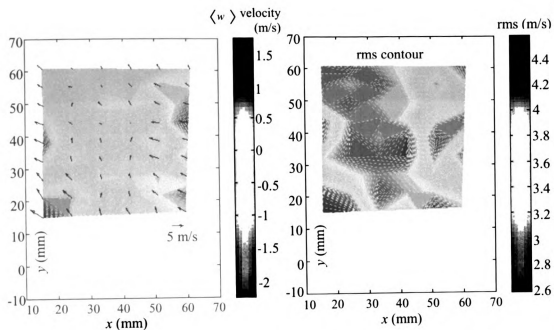


Figure 4-17. Ensemble-averaged velocity field (left) and velocity rms (right) at 260 crank angle degree and 900 rpm engine speed

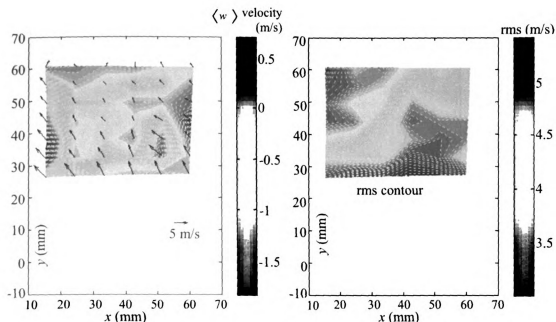


Figure 4-18. Ensemble-averaged velocity field (left) and velocity rms (right) at 280 crank angle degree and 900 rpm engine speed

4.3.2 Flow measurements at 1200 rpm engine speed

Velocity and pressure measurements are presented at 1200 rpm engine speed. Figure 4.19 shows the averaged in-cylinder pressure trace. 150 consecutive cycles are considered to obtain this averaged pressure profile. The peak pressure is about 21.5 bars and located at TDC of compression. No significant difference can be observed in pressure values compared to the in-cylinder pressure values recorded at the lower engine speed of 900 rpm due to motoring conditions; see Fig. 4.7 for comparison.

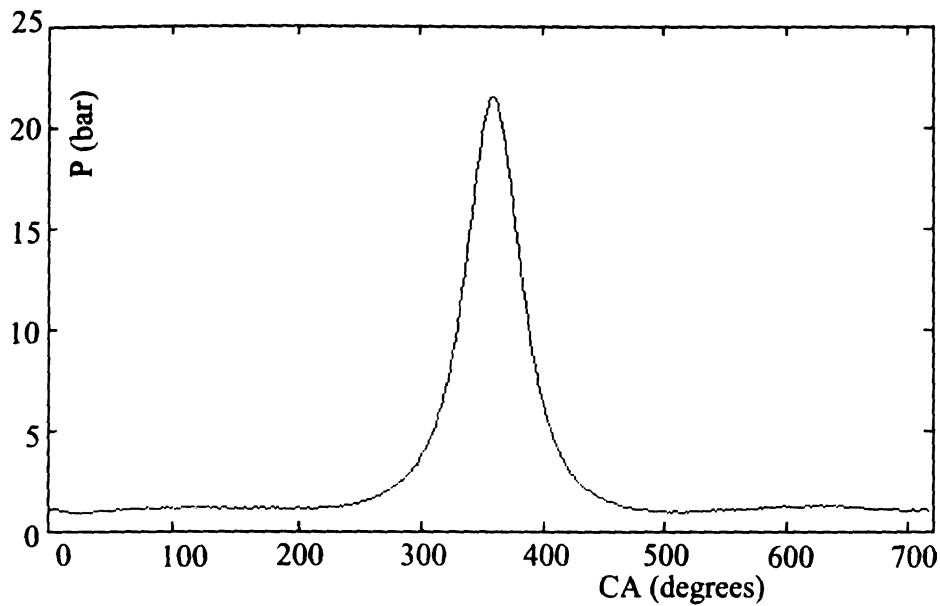


Figure 4-19. Averaged in-cylinder pressure trace at 1200 rpm engine speed

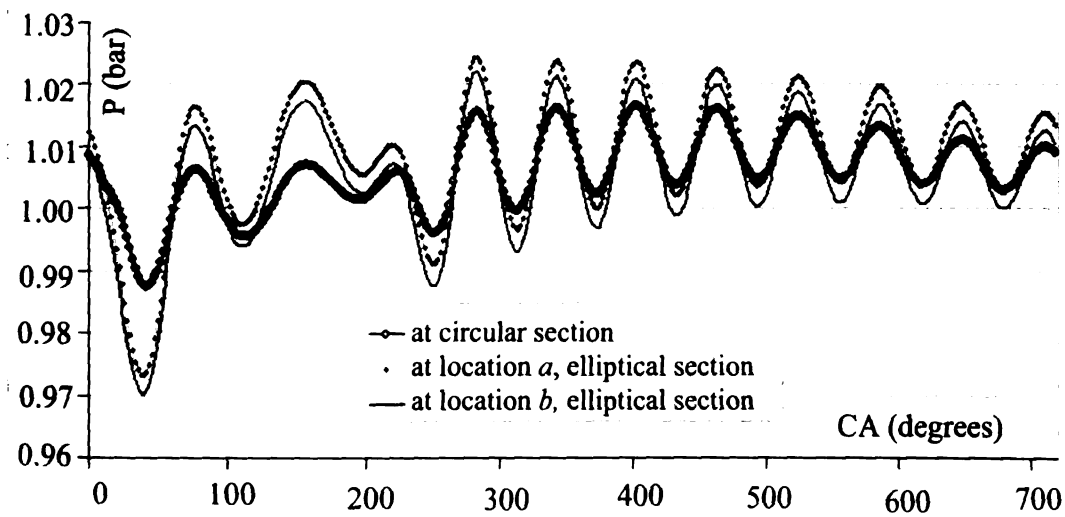


Figure 4-20. Averaged pressure trace at the circular and elliptical sections of the intake manifold at 1200 rpm engine speed

Figure 4.20 shows the averaged pressure profiles over the circular section and at locations, *a* and *b*, over the elliptical plane near the intake port. The minimum pressure at the circular section is about 98.7 kPa, and it is observed during the intake stroke, as expected. The peak pressure during the cycle is slightly less than 102 kPa. Similar to the measurements at 900 rpm, during the forward flow, pressure is higher at the circular plane compared to the locations over the elliptical plane. Similarly, during the backflow, due to the reversal of flow direction, pressure magnitudes are higher at elliptical plane locations compared to the values at circular plane.

Figure 4.21 shows the velocity profiles at various radial locations. The peak velocity magnitude is about 15 m/s during the intake stroke at 60 crank angle degrees. This may be due to high piston acceleration at this point. It then diminishes and increases again at about 120 CAD. Also, as shown in the figure, the velocity magnitudes are higher at the center of the plane during the forward flow when compared to the velocity magnitudes near the wall; however, during the back flow, magnitudes are relatively higher near the wall. Also, note that the velocity magnitudes at locations 1 and 3 are in close agreement with each other. This shows the axis symmetry nature of flow for the geometry considered in this work. As expected, the oscillating peak of velocity magnitude decreases traversing from intake to exhaust stroke during the cycle.

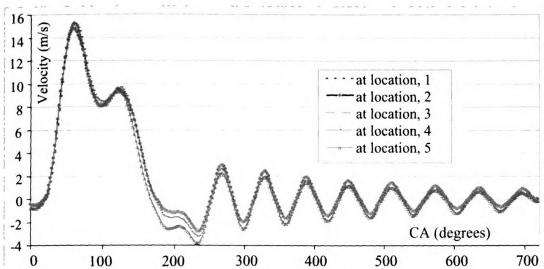


Figure 4-21. Averaged velocity profile at different radial locations in circular section of the intake manifold at 1200 rpm engine speed

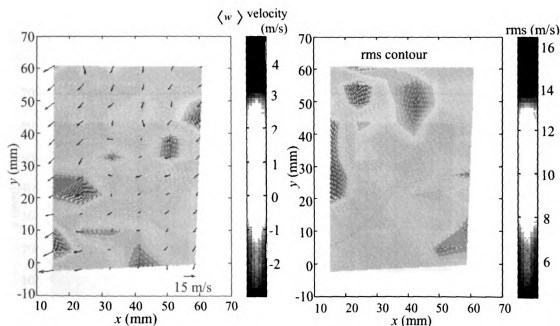


Figure 4-22. Ensemble-averaged velocity field (left) and velocity rms (right) at 170 crank angle degree and 1200 rpm engine speed

Figure 4.22 shows the ensemble-averaged velocity data (left), $\langle u \rangle$, $\langle v \rangle$ and $\langle w \rangle$, and rms of velocity (right) at 170 crank angle degree during the intake stroke at 1200 rpm

engine speed. The velocity vectors in the ensemble-averaged plot represent the magnitude of $\langle u \rangle$ and $\langle v \rangle$ components, while color contours show the magnitude of the $\langle w \rangle$ component. As expected, the axial component of velocity, $\langle v \rangle$, has higher magnitudes toward the upper section of the plane and it diminishes toward the lower section of the plane. The rms values are as high as 16 m/s toward the central upper right section of the measurement plane.

Figure 4.23 shows the ensemble-averaged velocity, $\langle u \rangle$, $\langle v \rangle$ and $\langle w \rangle$, and rms of velocity at 210 CAD during the compression stroke. Due to upward piston motion at this crank angle, the flow is dominant in positive y direction. The rms values are as high as 11 m/s, however, lower than the rms values observed during the intake stroke at 170 CAD.

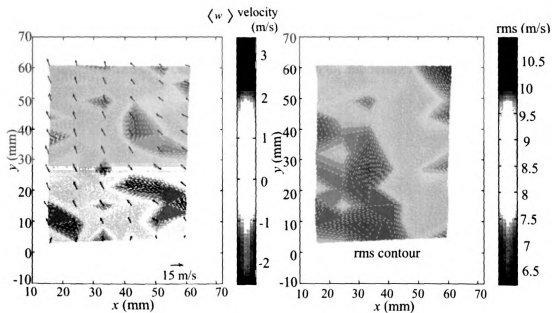


Figure 4-23. Ensemble-averaged velocity field (left) and velocity rms (right) at 210 crank angle degree and 1200 rpm engine speed

4.4 Summary

Experiments are performed to measure the velocity and pressure inside the intake manifold of a motored internal combustion engine assembly. A hot-wire anemometer and piezoresistive absolute pressure transducers are used to measure the instantaneous velocity and pressure, respectively. Measurements are performed at 900 and 1200 rpm engine speeds. Results showed the oscillatory nature of flow inside the intake manifold. The peak velocities, inside the intake manifold, are about 9 and 15 m/s during the intake stroke at 900 and 1200 rpm engine speeds, respectively. In-cylinder flow measurements are also performed to validate the modeling efforts, under development. Stereoscopic molecular tagging velocimetry is used for this purpose.

Results of this study have particular significance on the development of more accurate multi-dimensional numerical simulations of in-cylinder flows. This study provides the necessary boundary conditions for numerical simulations. Also, in-cylinder velocity and pressure data can be used to validation the modeling efforts.

CHAPTER-5

IN-CYLINDER COMBUSTION DIAGNOSIS IN AN ETHANOL-GASOLINE, DUAL-FUELED, SPARK IGNITION ENGINE

5.1 Introduction

Improvement in fuel efficiency and reduction in exhaust emissions are the two main driving forces behind the new developments in internal combustion engines. In addition, the increasing interest in using renewable energy sources as alternative fuels has prompted research into the nature of combustion when these fuels are utilized. Ethanol is one of these fuels. Ethanol has a higher octane number than gasoline and thus the potential for higher efficiency, by increasing compression ratio, exists, Mittal et al.⁸¹ (2008). However, its lower heating value leads to fewer driving miles per gallon when it is used as a direct replacement in current gasoline engines. Also, vehicle modifications are required to operate the gasoline vehicles on high ethanol content blended fuels due to its poor startability in cold weather and the requirement of ethanol corrosion-resistant materials for the fuel system. Therefore, the blend of ethanol (in gasoline) is more widely used in the vehicles that are designed to operate on gasoline fuel. This reduces the consumption of fossil fuels. Also, due to the high latent heat of evaporation of ethanol, combustion temperature decreases compared to vehicles operating on pure gasoline. This enables higher torque and higher thermal efficiency due to reduced cooling heat loss, Nakata et al.⁸² (2006). In the United States, 10 percent ethanol in gasoline is widely used in many fuel blends. In Brazil, the ethanol percentage is even higher and this has been in

use for several years, Brinkman⁸³ (1981). Ethanol can be produced from renewable energy sources such as corn, wheat, and sugar cane. Table 5.1 shows the physical properties of ethanol and gasoline for comparison, Srivastava et al.⁸⁴ (2009). Note the higher octane rating of ethanol than gasoline. This overcomes the disadvantage of a lower heating value of ethanol compared to gasoline.

Parameter	Ethanol	Gasoline
Molecular weight (g/mol)	46.070	113.228
Average octane number (RON+MON)/2	104	91
Lower heating value (MJ/Kg)	28	43
Latent heat of vaporization at 300 K (KJ/Kg)	1025	317
Heat of formation (KJ/mole)	-217	-221
Liquid density at 293 K and 1 atm (Kg/m ³)	789	751
Boiling point (K)	351	411
Ignition temperature (K)	695	553

Table 5-1. Properties of ethanol and gasoline

Several studies have been performed to investigate the effect of ethanol fuel in internal combustion engines. Starkman et al.⁸⁵ (1964) provided the comparison between various alcohol and hydrocarbon fuels. Brinkman⁸³ (1981) studied the effect of equivalence ratio and compression ratio on efficiency and exhaust emissions of an IC

engine operating on ethanol fuel. Salih and Andrews⁸⁶ (1992) studied the influence of gasoline-ethanol blends on emissions and fuel economy in a spark ignition engine. Their results showed significant reduction in nitrogen oxides (NO_x) and carbon monoxide (CO) emissions using ethanol-blended fuels. The unburned hydrocarbon emissions with ethanol blends were found to be higher than for 100 % gasoline. Nakata et al.⁸² (2006) also investigated the influence of ethanol fuel on SI engine performance, thermal efficiency, and emissions. Bromberg et al.⁸⁷ (2006) studied the case with Direct-Injection (DI) ethanol and Port-Fuel-Injection (PFI) gasoline where ethanol was only used to reduce the engine knock; however, the study of ethanol fuel in IC engines was not extended to optimize the combination of both PFI and DI fuel injection systems.

The objective of this work is to investigate the combustion characteristics of an ethanol-gasoline, dual fueled, single cylinder spark ignition engine. A dual fuel injection system with both direct-injection and port-fuel-injection is used in this work. The performance of PFI-E85 and DI-gasoline, and PFI-gasoline and DI-E85 systems is presented. E85 is a blend of 85 % ethanol and 15 % gasoline by volume. In each test, the percentage of E85 is varied from 100 (0 % gasoline) to 0 (100 % gasoline) to compare the various cases. PFI-gasoline and DI-gasoline (PFI and DI-gasoline) results are also presented to provide a baseline for comparison. The cycle-to-cycle variability is presented using coefficient of variation in indicated mean effective pressure. Mass fraction burned and burn duration are determined from the analysis of measured in-cylinder pressure data. The well-known Rassweiler and Withrow method (Model 1), with a new linear model for the polytropic index, is used to obtain the MFB curves. The

differences are presented for the net pressure method (Model 2) to evaluate the burn rates. It is found that combustion is faster with the increase in PFI percentage for all the three setups with dual fuel injection. The PFI-E85 and DI-gasoline system showed that the burn duration decreases significantly with the increase in PFI percentage; however, the PFI-gasoline and DI-E85 system showed only slight differences with the increase in PFI percentage. Model 2 showed good agreement with Model 1 at high load conditions; however, it predicts slower combustion at light load conditions. Model 2 has an advantage that the data processing time is short enough to allow for online processing. Therefore further investigation is performed to improve Model 2 calculations to evaluate the mass fraction burned at light load conditions.

5.2 Experimental setup

Figure 5.1 shows the experimental setup of the dual fueled spark ignition engine used for this study. The engine used for the experiments is a single cylinder Ford 5.4 l 3-valve engine with two intake and one exhaust valves. Both port-fuel-injection and direct-injection are used for each test measurement. Details of seven different tests performed for PFI-E85 and DI-gasoline, PFI-gasoline and DI-E85, and PFI and DI-gasoline systems are shown in Table 5.2. Experiments are performed at different loads, 3.3 bar IMEP and wide open throttle; and engine speeds of 1500 and 2500 rpm. For each test measurement, five different cases are considered with PFI percentages of 100, 70, 50, 30, and 0. The percentage of DI is correspondingly increased to maintain a constant relative air-to-fuel ratio (λ), inverse of fuel-to-air equivalence ratio (ϕ). For each case, the experiments started at zero DI fuel injection, and then the DI fuel injection was increased to the

desired percentage while maintaining a constant relative air-to-fuel ratio. Note that when a certain percentage of E85 is used, the air-to-fuel ratio λ , which is to be constant, is measured by the oxygen sensor. The uncertainties due to environmental variations are minimized by taking measurements for different tests in a single day with constant engine coolant temperature. Pressure measurements inside the engine cylinder are performed using a piezoelectric pressure transducer. 300 consecutive cycles are recorded for each case with one degree of crank angle resolution. The measurement range for the pressure transducer was from 0 to 250 bars. Data acquisition is performed using a high speed combustion analysis system of A&D technologies.

A. PFI - E85 and DI - gasoline		
Test No.	Load	Engine Speed (rpm)
A1.	3.3 bar IMEP	1500
A2.	WOT	1500
A3.	WOT	2500
B. PFI - gasoline and DI - E85		
B1.	3.3 bar IMEP	1500
B2.	WOT	1500
C. PFI and DI - gasoline		
C1.	3.3 bar IMEP	1500
C2.	WOT	1500

Table 5-2. Test matrix

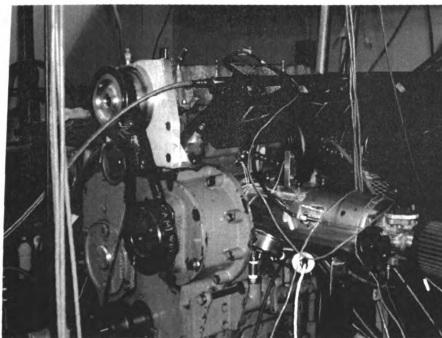


Figure 5-1. Experimental rig

5.3 Measurement Procedure

The primary purpose of combustion in a piston engine is to generate the pressure for shifting the expansion process away from the compression process and produce the work cycle. IMEP is an important parameter to measure the performance of this work-producing cycle that transforms heat from the combustion process into mechanical work. The measured pressure profile is used to calculate the IMEP for each cycle (Equation 5.1), and thus the mean is obtained over N consecutive cycles (300 cycles in this work) for each case.

$$IMEP = \frac{\int pdV}{V_d} \quad (5.1)$$

where V_d is the displaced volume. Work delivered to the piston over the entire cycle is obtained using the trapezoid rule. Cyclic variability is presented using the coefficient of variation in indicated mean effective pressure, COV_{imep} . It defines the cyclic variability in terms of indicated work per cycle. This is obtained using Equation 5.2, where σ is the standard deviation.

$$COV_{imep} = \frac{\sigma_{imep}}{IMEP} \times 100 \quad (5.2)$$

5.3.1 Mass fraction burned analysis

MFB is a measure of fraction of energy released, due to combustion of fuel inside an engine cylinder, with respect to the total energy released at the end of combustion during a cycle. Several methods have been suggested to evaluate the MFB in gasoline engines from the measured pressure data; see Section 1.2.2. This work utilizes the Rassweiler and Withrow method, denoted as Model 1, with a new linear model for polytropic index to evaluate the MFB curves. Start of combustion (SOC) and end of combustion (EOC) are uniquely determined from the logarithmic pressure indicator diagram using a least-square fit algorithm. Comparison is presented for another analysis model, denoted as Model 2, which utilizes the net pressure to evaluate the MFB curves as discussed in Section 5.3.1.2. Model 2 has an advantage that the data processing time is short enough to allow for online processing.

5.3.1.1 Model 1, Rassweiler and Withrow method

The implementation details of this method by Rassweiler and Withrow⁵¹ (1938) vary in literature. The data depicted in Figure 5.2 are provided for the measured pressure data in Test C2 with 100 % PFI-gasoline. In this figure, zero crank angle degree represents the piston position at top dead center. The initial state, i , and the final state, f , are the essential singularities of the combustion process which represent the start and end of combustion, respectively. The transition from i to f is referred to as the dynamic stage of combustion, Bitar et al.⁸⁸ (2006). In this model, it is assumed that for any crank angle interval, $\Delta\theta$, the actual pressure change, Δp , inside an engine cylinder is composed of a pressure rise due to combustion, Δp_c , and a pressure change due to the volume change, Δp_v , therefore $\Delta p = \Delta p_c + \Delta p_v$. The pressure change due to volume change can be obtained using a polytropic index. A constant index value was chosen originally by Rassweiler-Withrow where the magnitude was the average of the polytropic index before and after the combustion process. Brunt and Emtage⁵³ (1997) used the compression index, n_c , up to TDC and the expansion index, n_e , thereafter. A new linear model for polytropic index, n_d , during the combustion process is introduced in this work; however, the results are similar when the compression index, n_c , was used up to TDC and the expansion index, n_e , thereafter (Brunt and Emtage⁵³ (1997)); see Mittal et al.⁸⁹ (2009). Therefore the pressure change due to volume change in any interval, $\Delta\theta$, in the absence of combustion, can be obtained using Equation 5.3.

$$\Delta p_v = p_k - p_{k-1} = p_{k-1} \left[\left(\frac{V_{k-1}}{V_k} \right)^{n_{d_k}} - 1 \right] \quad (5.3)$$

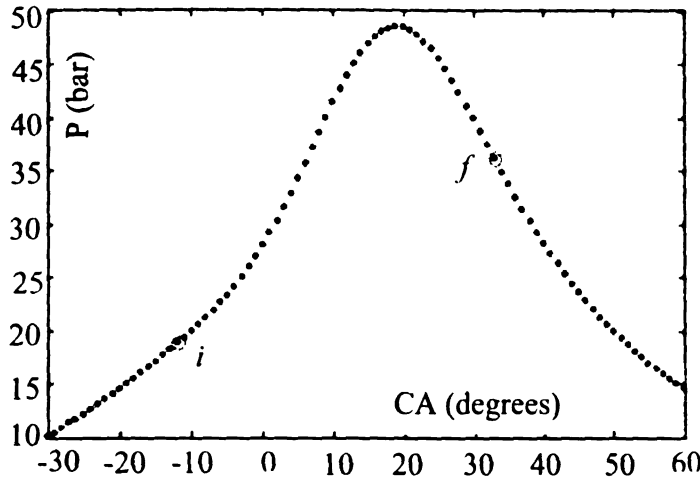


Figure 5-2. Measured pressure data, Test C2 (PFI-gasoline 100 %)

An indicator diagram in logarithmic scales, Figure 5.3, is used to evaluate the polytropic indexes, n_c and n_e . V_s in the figure represents the normalized volume with respect to the clearance volume. The two states, i and f , are identified by the departure of the curve from the state lines representing the compression and expansion processes using a least-square fit algorithm. Now, with the known $\Delta p_c = \Delta p - \Delta p_v$, and assuming that the mass of charge burned in the interval, $\Delta\theta$, is proportional to the pressure rise due to combustion, the MFB at the end of the k^{th} interval can be evaluated using Equation 5.4,

$$\frac{m_{b_k}}{m_{b_{total}}} = \frac{\sum_0^k \Delta p_c}{\sum_0^N \Delta p_c} \quad (5.4)$$

where N is the total number of crank angle intervals during the combustion process.

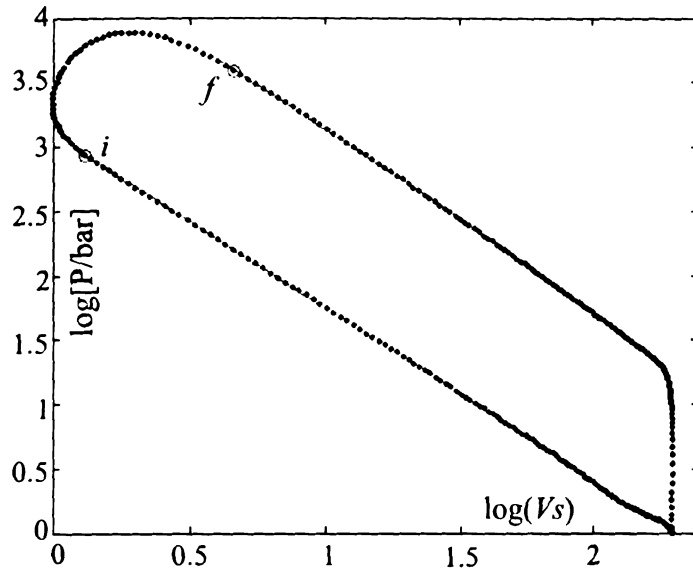


Figure 5-3. Indicator diagram in logarithmic scales, Test C2 (PFI-gasoline 100 %)

5.3.1.2 Model 2, Net Pressure method

This model evaluates the mass fraction burned by normalizing the net pressure with respect to the overall net pressure increase at the end of combustion, Zhu et al.⁹⁰

(2003). The net pressure change, $\Delta p(k)$, between the two crank angles is:

$$\Delta p(k) = \left\{ p(k+1) - p(k) \left[\frac{V(k)}{V(k+1)} \right]^{n=1.3} \right\} \left[\frac{V(k)}{V_{Ig}} \right] \quad (5.5)$$

and the net pressure at each crank angle is

$$p_{NET}(k) = p_{NET}(k-1) + \Delta p(k) \quad (5.6)$$

where p is the pressure, V is the volume, and V_{Ig} is the chamber volume at the ignition point. The simplicity of Model 2 is apparent from Equations 5.5 and 5.6. It is computationally efficient and due to the short data processing time, it can be used for online processing.

5.4 Experimental Results

Combustion characteristics of an ethanol-gasoline dual fueled injection system in a single cylinder SI engine are presented. Figure 5.4 shows the mean IMEP (top) and COV_{imep} (bottom) for the various test data. As shown in the figure, the mean IMEP is almost constant for DI-E85 and PFI-gasoline system for different cases with the decrease in DI-E85 (or increase in PFI-gasoline); however, it increases with the increase in PFI-E85 for PFI-E85 and DI-gasoline system at similar load conditions. The mean IMEP is about 7.5 bar for PFI-E85 (100 %) and DI-gasoline (0 %) system when engine is operated at 1500 rpm with WOT. At similar operating conditions, the mean IMEP for DI-E85 and PFI-gasoline is about 9 bar. At 2500 rpm engine speed with WOT, the mean IMEP increases from about 10 to 10.92 bar with the increase in E85 percentage (0 to 100) for PFI-E85 and DI- gasoline system. The COV of IMEP decreases with the increase in PFI percent (beyond 50 %) for each test point (Tests A and B in Table 5.2). The cyclic variability has the peak either at 30 or 50 % of PFI. 100 % PFI shows the minimum cyclic variability for each test, and the COV of IMEP is even less than 1 for the PFI-E85 and DI-gasoline system when the engine is operated at 1500 rpm with WOT condition.

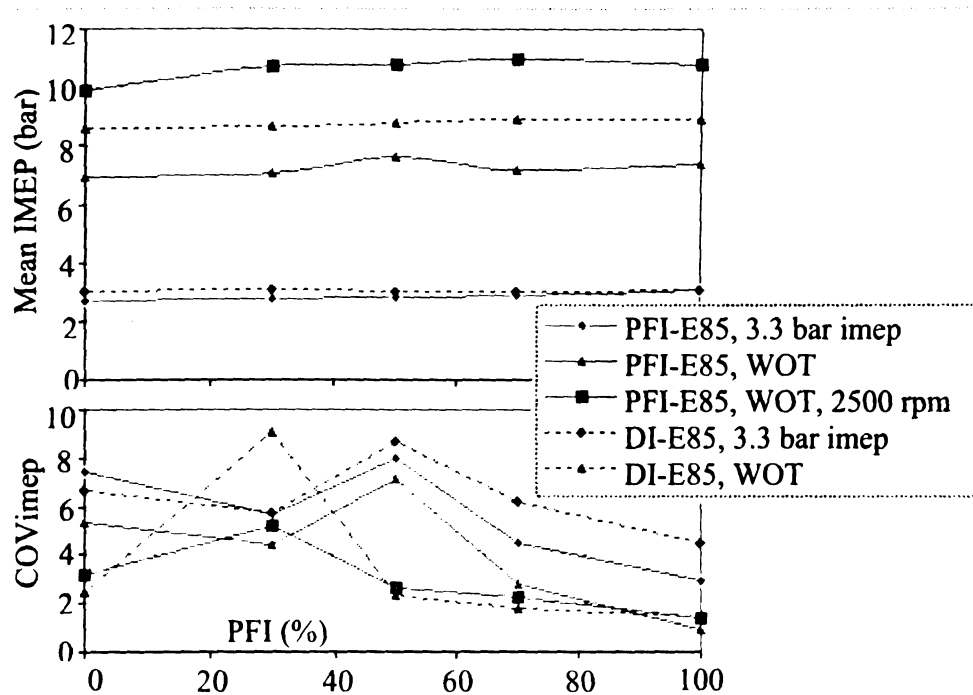


Figure 5-4. Mean IMEP (top) and COV_{imep} (bottom) for PFI-E85 and DI-gasoline, and DI-E85 and PFI-gasoline systems

5.4.1 PFI-E85 and DI-Gasoline system

This section describes the combustion characteristics of an ethanol-gasoline, dual fueled injection system in a single cylinder SI engine where PFI system is used for E85 injection and DI system is used for gasoline injection (PFI-E85 and DI-gasoline). Tests A1, A2 and A3 in Table 5.2 represent these measurements at 3.3 bar IMEP and WOT load conditions with engine speeds of 1500 and 2500 rpm. Five different cases are considered for each test with PFI E85 percentages of 100, 70, 50, 30, and 0. The percentage of DI gasoline is correspondingly increased to maintain a constant relative air-to-fuel ratio (λ) for each case.

Figure 5.5 shows the averaged pressure profiles (top) and MFB curves (bottom) for Test A1 (3.3 bar IMEP, 1500 rpm). Three different cases are shown with PFI-E85

percentages of 0, 70 and 100. As shown in the figure, the peak pressure increases with the increase in PFI-E85. This is expected due to lower combustion gas temperature with ethanol than with gasoline. Based on this, it can be assumed that the cooling heat loss from the combustion chamber decreases with ethanol. Similarly, the burn duration decreases with the increase in PFI-E85. Ethanol has an advantage of high combustion speed for SI engines, Brinkman⁸³ (1981). The combustion process starts at about -20 CADs for all the cases. There is no significant difference in 10 % burn durations; however, 50 % and 90 % burn durations are much faster with 100 % PFI-E85 when compared to the other cases. The burn duration is about 51 CADs for 100 % PFI-E85 and increases with the decrease in PFI-E85. The difference of Model 2 results when compared to Model 1 is presented using vertical bars in the figure. The vertical bars in the downward direction indicate that Model 2 predicts slower combustion when compared to Model 1 and the difference increases with the decrease in PFI percentage. It was found that the proper selection of polytropic index (n) and the determination of end of combustion are the important parameters for calculating the MFB curves using Model 2. Model 2 determination of EOC is significantly later than the actual CAD value, at this light load condition, and therefore it predicts slower combustion compared to Model 1.

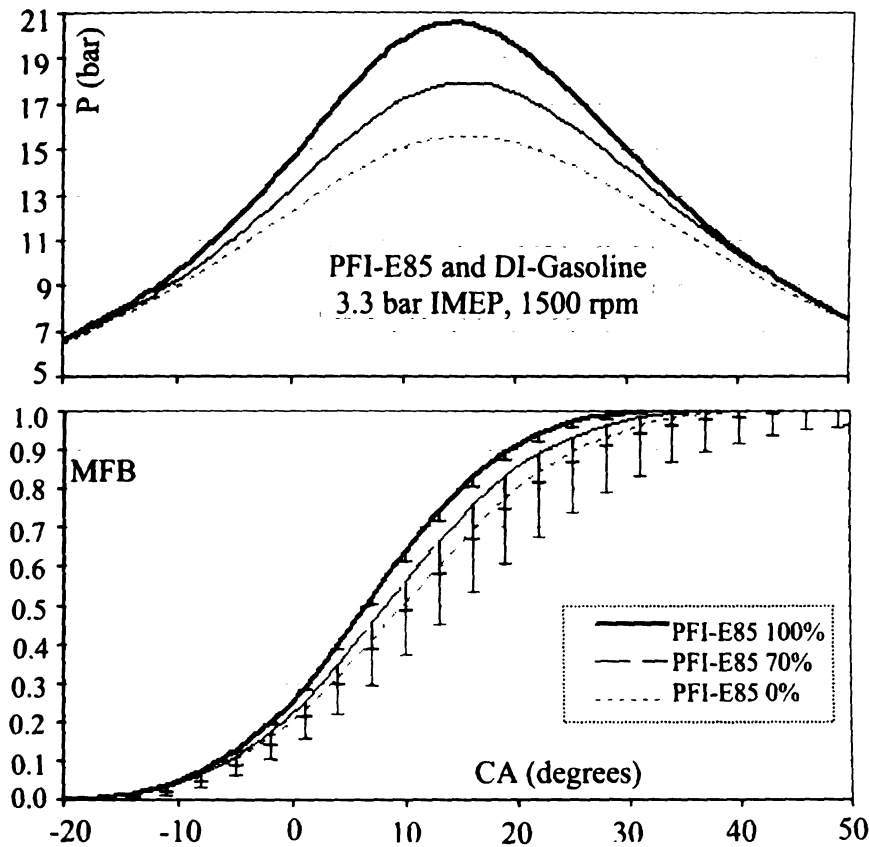


Figure 5-5. Averaged Pressure (top) and MFB curves (bottom) for PFI-E85 and DI-gasoline system at 3.3 bar IMEP and 1500 rpm

Figure 5.6 shows the averaged pressure profiles (top) and MFB curves (bottom) for Test A2 (WOT, 1500 rpm) with PFI E85 percentages of 0, 70 and 100. Similar to Test A1 results, the peak pressure increases with the increase in PFI E85. It is interesting to note that the peak pressure is about 44.5 bar with 100 % PFI-E85 and then decreases sharply with the decrease in PFI-E85. Also, there is some phase shift in the peak pressure locations (CADs) due to fixed spark timing considered for the test data. As expected, the burn duration increases with the decrease in PFI-E85. At this load condition, combustion starts at about -12 CADs for all the cases and significant difference can be observed even at earlier stages (10 % burn) with much faster combustion for 100 % PFI-E85. Similarly,

50 % and 90 % burn durations are also less for 100 % PFI-E85 when compared to the other cases. The burn duration is about 39 CADs for 100 % PFI-E85 and increases with the decrease in PFI E85. Model 2, at 100 % PFI-E85, predicts slightly faster combustion than Model 1. It is in good agreement when PFI-E85 is 70 % and assumes slightly slower combustion when PFI-E85 is 0 %. Overall, Model 2 is in good agreement with Model 1 at this higher load condition.

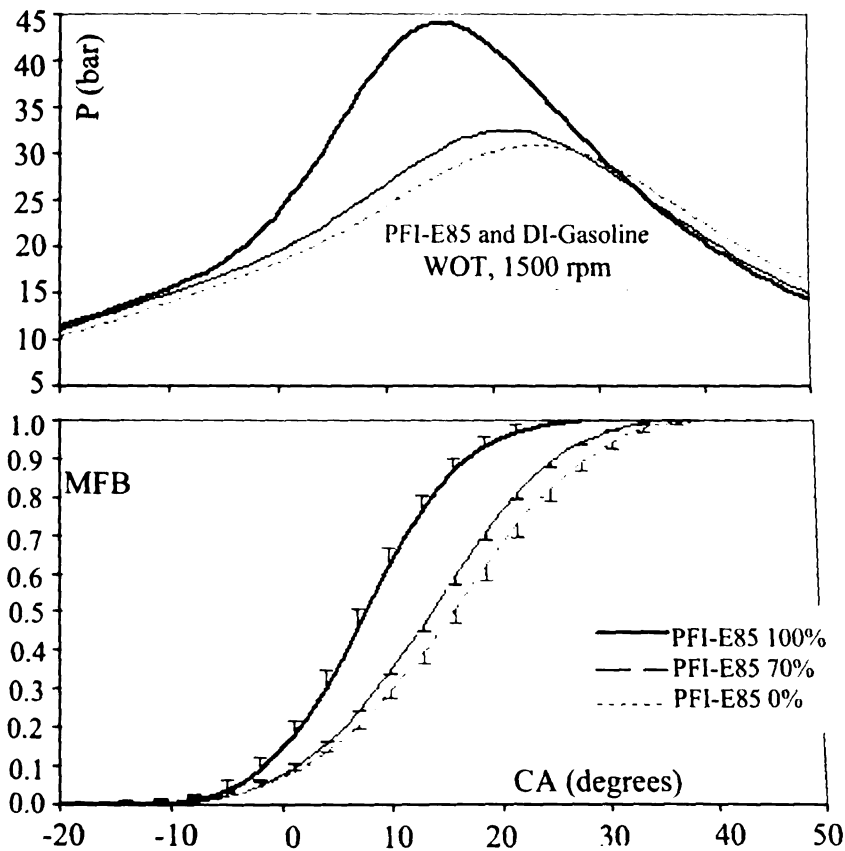


Figure 5-6. Averaged Pressure (top) and MFB curves (bottom) for PFI-E85 and DI-gasoline system at WOT and 1500 rpm

Figure 5.7 shows the averaged pressure profiles (top) and MFB curves (bottom) for Test A3 (WOT, 2500 rpm) with PFI E85 percentages of 0, 70 and 100. Similar to Tests A1 and A2, the peak pressure increases with the increase in PFI, and it is as high as

55 bar with 100 % PFI-E85. The burn duration is about 37 CADs for 100 % PFI. It increases with the decrease in PFI-E85; however, no significant difference can be observed when PFI-E85 is 70 and 0 %. Also, Model 2 shows good agreement with Model 1 at this high load condition and higher engine speed.

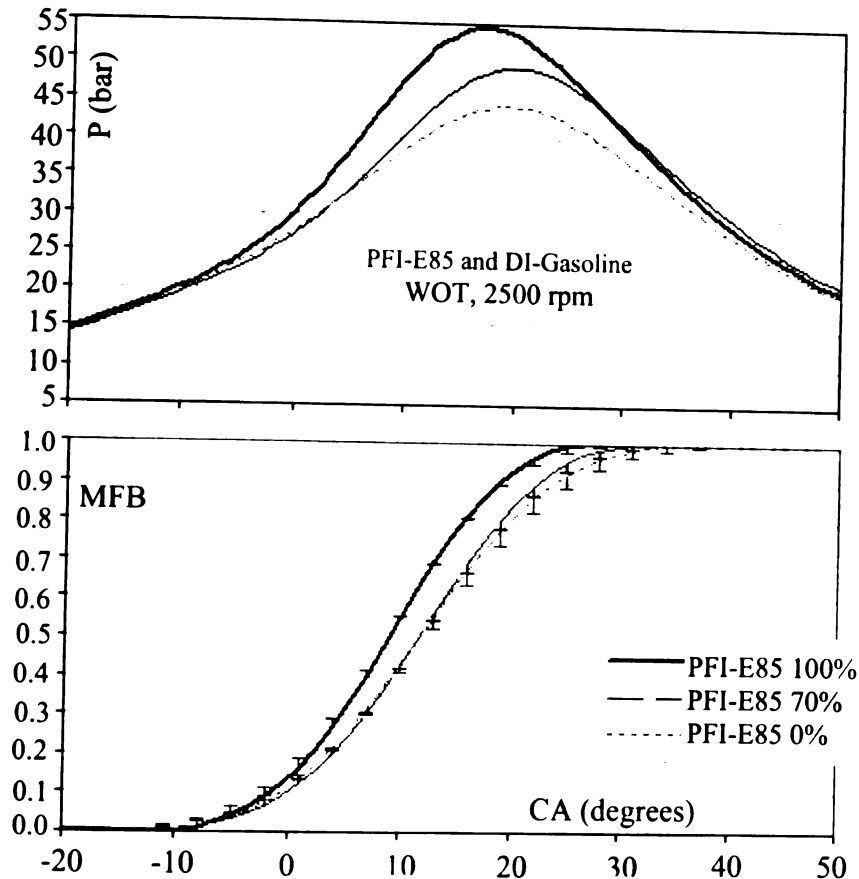


Figure 5-7. Averaged Pressure (top) and MFB curves (bottom) for PFI-E85 and DI-gasoline system at WOT and 2500 rpm

5.4.2 DI-E85 and PFI-Gasoline system

This section describes the combustion characteristics of an ethanol-gasoline, dual fueled injection system in a single cylinder SI engine where a DI system is used for E85 injection and a PFI system is used for gasoline injection, (DI-E85 and PFI-gasoline). Tests B1 and B2 represent these measurements at 3.3 bar IMEP and WOT load

conditions, respectively. Five different cases are considered for each test with PFI gasoline percentages of 100, 70, 50, 30, and 0. The percentage of DI E85 is correspondingly increased to maintain a constant relative air-to-fuel ratio for each case.

Figure 5.8 shows the averaged pressure profiles (top) and MFB curves (bottom) for Test B1 (3.3 bar IMEP, 1500 rpm). Only two cases with DI E85 percentages of 0 and 100 are shown due to less variation in measured pressure and MFB curves. As shown in the figure, there is no significant difference in measured pressure profiles at this part load condition; however, it is interesting to note that the peak pressure increases slightly with the decrease in DI-E85. Similar to the pressure profiles, no significant difference is observed in burn durations. The burn duration is about 58 CADs for 0 % DI-E85 and increases only slightly with the increase in DI-E85. Similar to the results shown in Figure 5.5 (PFI-E85 and DI-gasoline system with part load condition), Model 2 predicts slower combustion and the difference with respect to Model 1 increases with the decrease in PFI percentage.

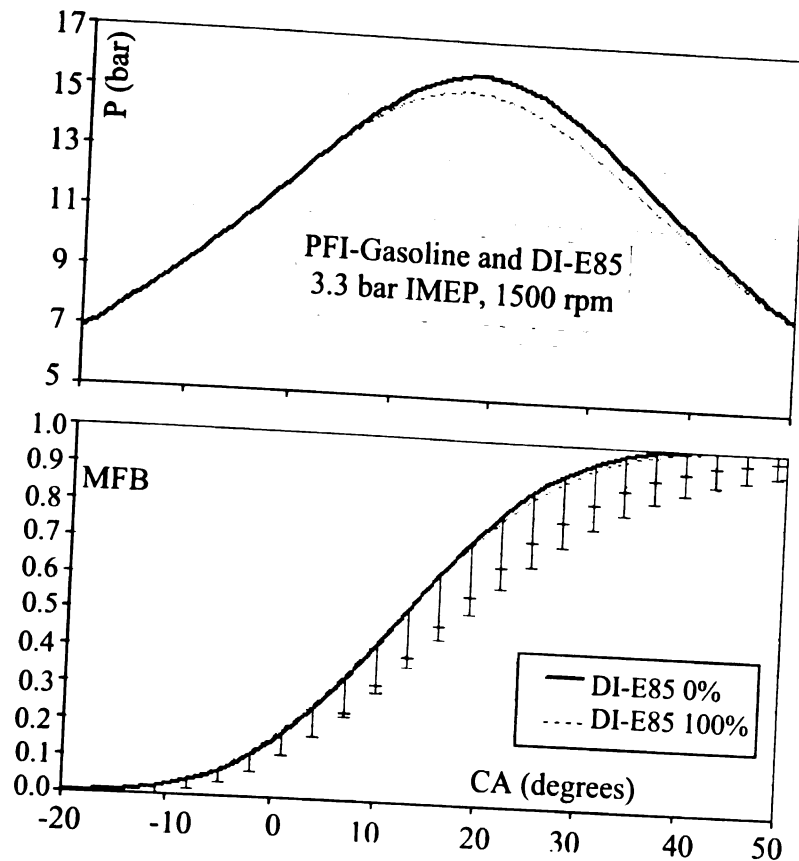


Figure 5-8. Averaged Pressure (top) and MFB curves (bottom) for DI-E85 and PFI-gasoline system at 3.3 bar IMEP and 1500 rpm

Figure 5.9 shows the averaged pressure profiles (top) and MFB curves (bottom) for Test B2 (WOT, 1500 rpm) with DI-E85 percentages of 0 and 100. This figure can be compared with Figure 5.6 (PFI-E85 and DI-gasoline system) with similar load conditions. The peak pressure is slightly higher for 0 % DI-E85, and it is as high as 46 bar. Similar to the part load condition, Figure 5.8, there is no significant difference in burn durations, and it is about 40 CADs for 0 % DI-E85. Model 2 results at this high load condition are in good agreement with Model 1 due to accurate determination of EOC.

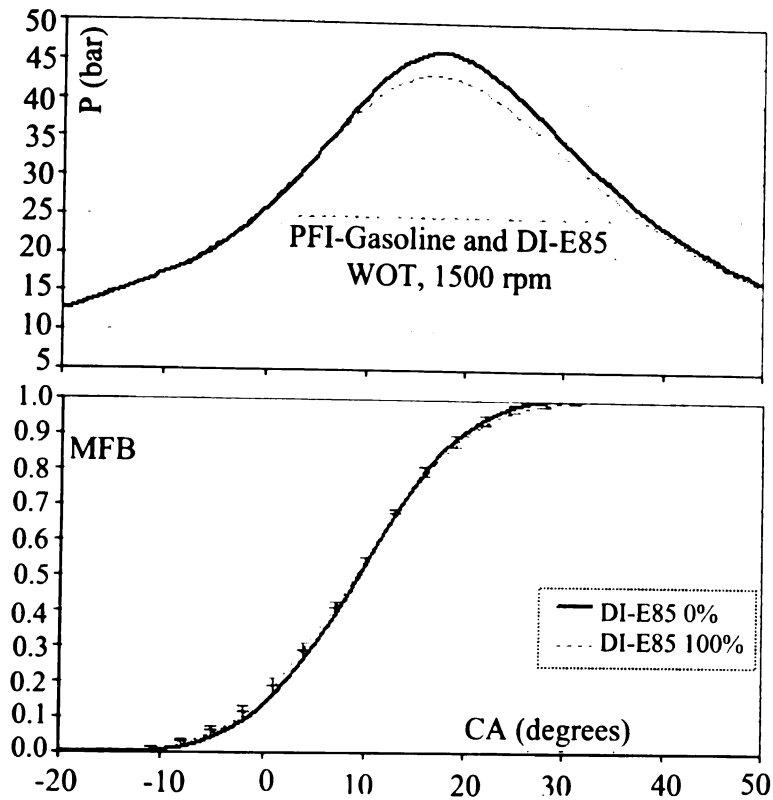


Figure 5-9. Averaged Pressure (top) and MFB curves (bottom) for DI-E85 and PFI-gasoline system at WOT and 1500 rpm

5.4.3 PFI-Gasoline and DI-Gasoline system

This section describes the combustion characteristics of a dual injection system where gasoline is used for both PFI and DI. Tests C1 and C2 represent these measurements at 3.3 bar IMEP and WOT load conditions, respectively. Five different cases are considered for each test with PFI gasoline percentages of 100, 70, 50, 30, and 0. The percentage of DI gasoline is correspondingly increased to maintain a constant relative air-to-fuel ratio for each case.

Figure 5.10 shows the averaged pressure profiles (top) and MFB curves (bottom) for Test C1 (3.3 bar IMEP, 1500 rpm). Three different cases with PFI gasoline percentages of 0, 50 and 100 are shown in the figure. The peak pressure increases with the increase in

PFI percentage, and it is about 15 bar for 100 % PFI. However, no significant difference can be observed in burn durations. The combustion process starts at about -18 CADs (all cases) and the burn durations are 61, 63 and 65 CADs for 100, 50 and 0 % PFI-gasoline, respectively. As seen earlier, Model 2 has slower combustion, compared to Model 1, when engine is operated at 3.3 bar IMEP.

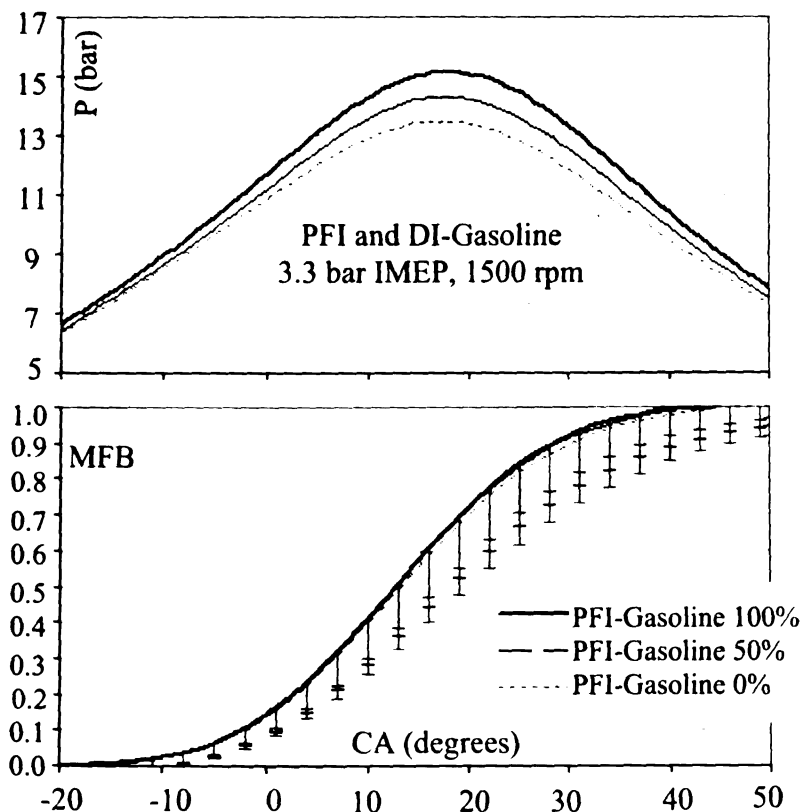


Figure 5-10. Averaged Pressure (top) and MFB curves (bottom) for PFI and DI-gasoline system at 3.3 bar IMEP and 1500 rpm

Figure 5.11 shows the averaged pressure profiles (top) and MFB curves (bottom) for Test C2 (WOT, 1500 rpm) with PFI gasoline percentages of 0, 50 and 100. Similar to Test C1, the peak pressure increases with the increase in PFI, and it is as high as 48 bar with 100 % PFI. The burn duration is slightly shorter, and about 45 CADs for 100 % PFI.

No significant difference is observed in further cases with the decrease in PFI percentage. Again, Model 2 shows good agreement with Model 1 when the engine is operated at wide open throttle.

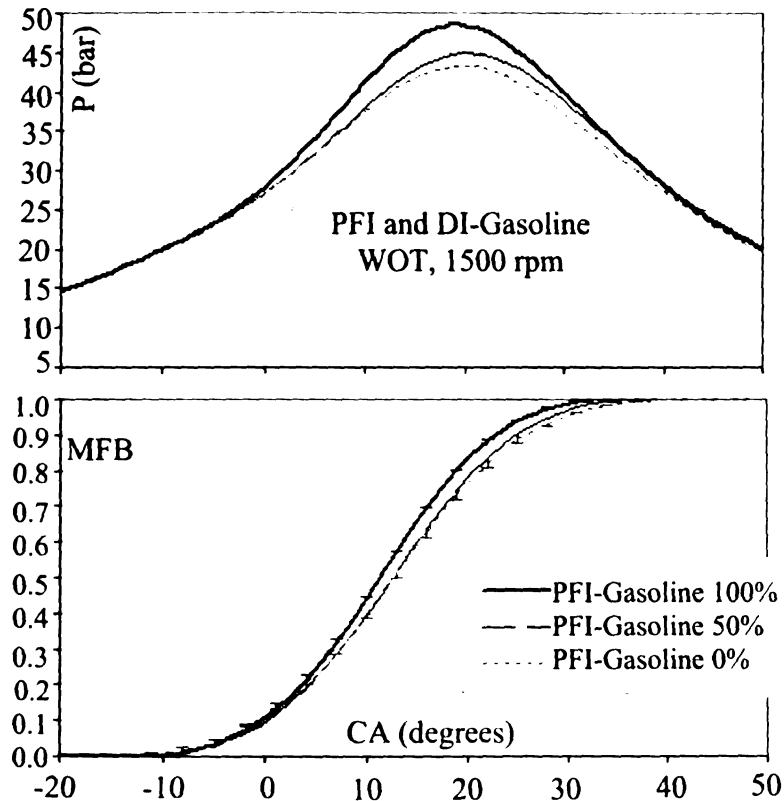


Figure 5-11. Averaged Pressure (top) and MFB curves (bottom) for PFI and DI-gasoline system at WOT and 1500 rpm

5.5 Improving the MFB calculation using net pressure method

Combustion characteristics of an ethanol-gasoline, dual fueled, single cylinder SI engine are presented in Section 5.4. The results of mass fraction burned calculation, using the net pressure method (Model 2), are compared with the well established Rassweiler and Withrow method (Model 1). Both the methods showed good agreement at high load conditions; however, the net pressure method showed slower combustion than that of the

Rassweiler and Withrow method at part load conditions. Model 2 has an advantage that the data processing time is short enough to allow for online processing. Therefore, further investigation is performed to improve Model 2 calculations to evaluate the mass fraction burned at light load conditions. In-cylinder pressure data is considered for the PFI-gasoline and DI-gasoline system with 100 % PFI. It is found that the proper selection of polytropic index, n , and the determination of end of combustion are the important parameters for calculating the MFB curves using Model 2, Mittal et al.⁸⁹ (2009). The EOC in Model 1 is determined accurately using a least-square fit algorithm; however, in Model 2, it is determined by locating the peak of the net pressure. At high load conditions, Model 2 determines the EOC with a reasonable accuracy, and therefore the results are in close agreement with Model 1. At part load conditions, this method (Model 2) is less ideal to determine the EOC than that at high loads. It predicts EOC significantly later than the actual crank angle value, and therefore Model 2 has slower combustion compared to Model 1. The accurate determination of EOC in Model 2 is affected by selection of polytropic index, n . Note that the constant polytropic index, $n = 1.3$, is used in Equation 5.5. The effect of the polytropic index on the EOC determination, and therefore its influence on the MFB calculation, at part load conditions, is shown in Figure 5.12 (upper graph). The difference in calculating the MFB (using Model 2) reduces compared to Model 1 when the index value $n = n_e = 1.20$ is used in Equation 5.5. This is due to the determination of the EOC with improved accuracy; however, some slight differences can still be observed with this index value ($n = n_e$). The index value $n = n_c = 1.165$, in Equation 5.5, determines the EOC with reasonable accuracy compared to Model

1 determination using a least-square fit algorithm. Therefore the MFB profile also shows good agreement with Model 1 when $n = n_c$ is used in Equation 5.5. The model 2 MFB calculation, with $n = n_c$, also shows good agreement with model 1 results at the WOT load condition (lower graph). Note that the polytropic index of expansion (n_e), SOC and EOC determinations using a least-square fit algorithm make Model 1 computationally more expensive than that of Model 2. Therefore, Model 2 is simple to implement, and the data processing time is short enough to allow for real-time applications. Mittal et al.⁸⁹ (2009) discussed the robustness of the net pressure method at different engine speeds and also with the variation in PFI and DI percentages of the dual fuel system in SI engine.

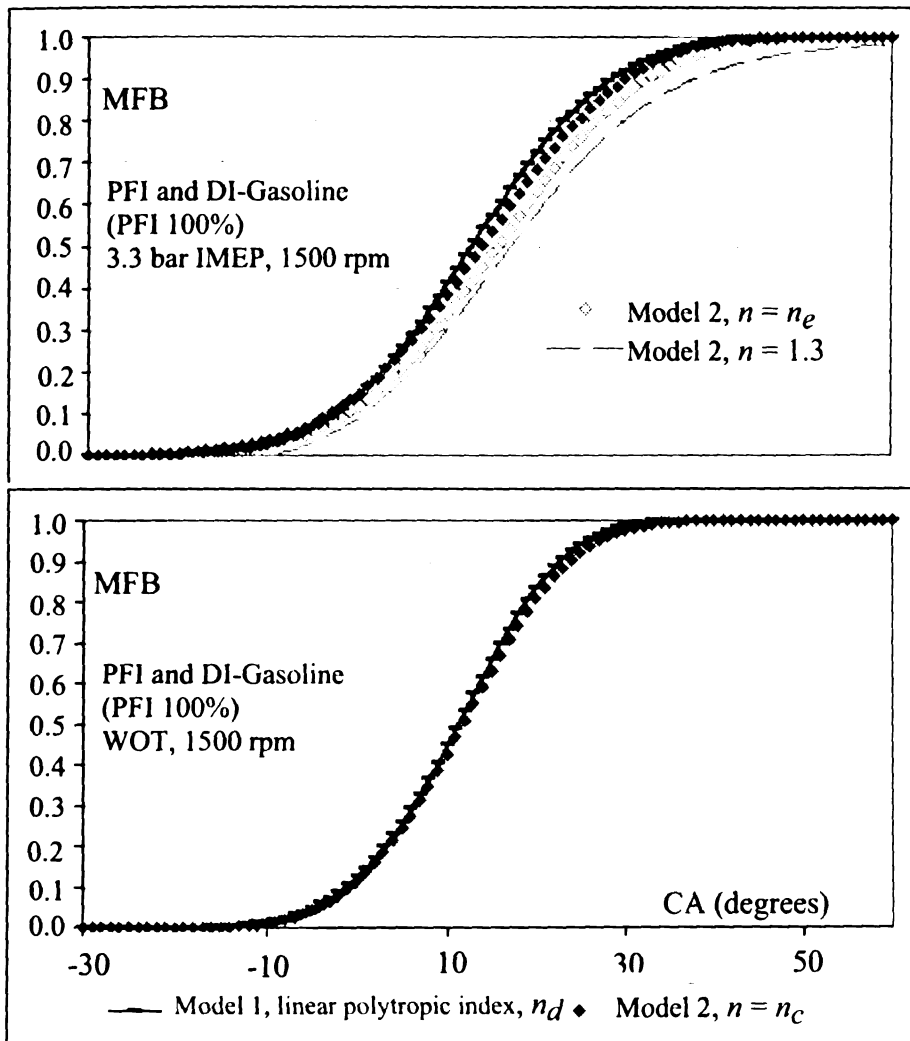


Figure 5-12. MFBs for PFI-gasoline and DI-gasoline system at 3.3 bar IMEP (top) and WOT (bottom)

5.6 Summary

Combustion characteristics of a dual fuel injection system in a single cylinder SI engine are presented. Variations including PFI-E85 and DI-gasoline, PFI-gasoline and DI-E85, and PFI and DI-gasoline systems are compared at different load conditions. In each test study, the percentage of DI system is varied from 0 to 100 %. The cycle-to-

cycle variability is presented using COV in IMEP. MFB and burn angles are determined from the analysis of measured in-cylinder pressure data.

- PFI-E85 and DI-gasoline: Results show that mean IMEP increases with the increase in PFI-E85 due to reduced charge cooling effect and fast ethanol combustion. Similarly, the combustion is faster with the increase in ethanol percentage (reduced DI charge cooling). The burn durations are 51, 39 and 37 CADs with 100 % PFI-E85 when the engine is operated at 3.3 bar IMEP (with 1500 rpm), WOT (1500 rpm) and WOT (2500 rpm) load conditions, respectively.
- PFI-gasoline and DI-E85: Results show that there is no significant difference in the mean IMEP with the increase in DI-E85. The effects of fast ethanol combustion due to increase in DI-E85 are compensated by the increase in DI charge cooling effects. Similarly, combustion duration decreases only slightly with the decrease in DI-E85. The burn durations with 0 % DI-E85 are 58 and 40 CADs when engine is operated at 3.3 bar IMEP and WOT load conditions, respectively.
- PFI and DI-gasoline: At part load condition, there is no significant difference in burn durations with the variation in PFI; however, at WOT it decreases only slightly with the increase in PFI. The burn durations with 100 % PFI are 61 and 45 CADs when engine is operated at 3.3 bar IMEP and WOT load conditions, respectively.

The comparison to evaluate the mass fraction burned from Model 2 (Net Pressure method) is presented with respect to Model 1 (Rassweiler and Withrow method with a new linear model for polytropic index). Results show that Model 2 is in good agreement with Model 1 at high load conditions; however, it predicts slower combustion at light load conditions. It is found that the net pressure method determines the EOC with

reasonable accuracy at WOT; however, its prediction of EOC at part load condition is significantly later than the actual value. The proposed modification of the net pressure method using a compression polytropic index ($n = n_c$) provides good agreement with the Rassweiler and Withrow method at part- and full- load conditions for calculating the mass fraction burned.

CHAPTER-6

FINAL REMARKS

In the studies of gaseous highly transient and three-dimensional flows that developed inside an IC engine, the MTV-based flow technique is superior to other non-intrusive measurement techniques, i.e. PIV, due to the ability of laser-tagged phosphorescent molecules that follow the flow perfectly. In this dissertation, MTV is used to obtain the multiple point measurement of an instantaneous velocity field. The effects of charge motion control on flow measurement inside an engine cylinder are studied. It is found that charge motion control has a profound effect on fuel-air mixing; however, its influence is not as significant during the late compression. In-cylinder engine flow measurements are extended to obtain an instantaneous three-component velocity field using stereoscopic MTV. The image-processing technique, implemented to obtain the velocity data, is computationally less expensive and eliminates the need to specify the geometric details, as in the earlier works, to obtain the three-components of velocity. Preliminary results show that cycle-to-cycle variations are more prominent in the velocity component perpendicular to the tumble plane, as opposed to the in-plane components. This type of experimental information will be valuable in the development of numerical simulations and advanced combustion systems under development. This work can be utilized as a tool for engine developers where only the logistics of operation need to be described.

In order to meet strict exhaust emissions and fuel efficiency standards, improved numerical simulations, supported by this type of experimental studies with experimentally proven boundary conditions, are desirable. Note that experimental measurements provide useful information of the flow fields inside the engine cylinder; however, it is multi-dimensional numerical simulations that offer the potential of significant time and cost savings to design the engine with improved performance. Real-time boundary conditions are necessary to perform more accurate multi-dimensional numerical simulations of complex in-cylinder flows. Therefore, velocity and pressure measurements are performed inside the intake manifold of an engine assembly that can provide the necessary boundary conditions for more accurate multi-dimensional numerical simulations. The geometry of the intake manifold is simplified for this purpose. A hot-wire anemometer and piezoresistive type absolute pressure transducers are used to measure the velocity and pressure, respectively. In-cylinder flow measurements are also performed to validate the modeling efforts. Stereoscopic molecular tagging velocimetry is used for this purpose.

In the second part of this work, combustion characteristics of an ethanol-gasoline, dual fueled, single cylinder spark ignition engine are investigated. The cycle-to-cycle variability is presented using the coefficient of variation in indicated mean effective pressure. Mass fraction burned and burn duration are determined from the analysis of measured in-cylinder pressure data. The well known Rassweiler and Withrow method (Model 1), with a new linear model for the polytropic index, is used to obtain the MFB curves. The differences are presented for the net pressure method (Model 2) to evaluate the burn rates. Model 2 showed good agreement with Model 1 at high load conditions;

however, it predicts slower combustion at light load conditions. Model 2 has an advantage that the data processing time is short enough to allow for online processing. Therefore, further investigation is performed to improve Model 2 calculations to evaluate the mass fraction burned at light load conditions.

In the future, experimental results of in-cylinder flow measurements will be compared with multi-dimensional numerical simulations. Also, in the future, measurements of a highly transient three-component velocity field will be taken at different crank angle positions inside the cylinder of Mahle 4-valve engine. The cycle-to-cycle flow variations will then be studied to develop a correlation for mass fraction burned during combustion process. The results will be compared with the calculated MFB curves using Rassweiler and Withrow method at the same load and engine speeds.

REFERENCES

REFERENCES

1. Heywood, J.B. (1987) "Fluid motion within the cylinder of internal combustion engines – The 1986 Freeman Scholar Lecture," *Journal of Fluids Engineering*, 109, pp. 3-35.
2. Heywood, J.B. (1988) *Internal combustion engine fundamentals*, McGraw – Hill Book Company, ISBN 0-07-028637-X.
3. Shen, Y. (2003) *Development of a basis for control of combustion in an internal combustion engine*, PhD Thesis, Michigan State University, East Lansing, MI.
4. Farrell, P.V. (2007) "Examples of in-cylinder velocity measurements for internal combustion engines," *Proceedings of the Institution of Mechanical Engineers. Part D, Journal of automobile engineering*, 221, pp. 675-697.
5. Hassan, H., and Dent, J.C. (1971) "The measurement of air velocity in a motored internal combustion engine using a hot-wire anemometer," *Proc. Instn. Mech. Engrs. (IMechE)*, 185, pp. 583-591
6. Bahram, K., Tahry, S.H., and Kuziak, W.R. (1986) "Measured steady flow velocity distributions around a valve/seat annulus," SAE Paper No. 860462.
7. Witze, P.O. (1980) "A critical comparison of hot-wire anemometry and laser doppler velocimetry for IC engine applications," SAE Paper No. 800132.
8. Morse, A.P., and Whitelaw, J.H. (1981) "Measurements of the in-cylinder flow of a motored four-stroke reciprocating engine," *Proceedings of the Royal Society of London. Series A, Mathematical and Physical Sciences*, 377, pp. 309-329.
9. Bicen, A.F., Vafidis, C., and Whitelaw, J.H. (1985) "Steady and unsteady airflow through the intake valve of a reciprocating engine," *Journal of Fluids Engineering*, 107, pp. 413-420.
10. Hall, M.J., and Bracco, F.V. (1987) "A study of velocities and turbulence intensities measured in firing and motored engines," SAE Paper No. 870453.
11. Kent, J.C., Haghgooie, M., Mikulec, A., Davis, G.C., and Tabaczynski, R.J. (1987) "Effects of intake port design and valve lift on in-cylinder flow and burnrate," SAE Paper No. 872153.
12. Fraser, R.A., and Bracco, F.V. (1989) "Cycle-resolved LDV integral length scale measurements investigating clearance height scaling, isotropy, and homogeneity in an IC engine," SAE Paper No. 890615.

13. Lee, K., Yoo, S.C., Stuecken, T., McCarrick, D., Schock, H., Hamady, F., LaPointe, L.A., Keller, P., and Hartman, P. (1993) "An experimental study of in-cylinder air flow in a 3.5l four-valve SI engine by high speed flow visualization and two-component LDV measurement," SAE Paper No. 930478.
14. Yoo, S.C., Lee, K., Novak, M., Schock, H., and Keller, P. (1995) "3-D LDV measurement of in-cylinder air flow in a 3.5l four-valve SI engine," SAE Paper No. 950648.
15. Hascher, H.G., Jaffri, K., Novak, M., Lee, K., Schock, H., Bonne, M., and Keller, P. (1997) "An evaluation of turbulent kinetic energy for the in-cylinder flow of a four-valve 3.5l SI engine using 3-D LDV measurements," SAE Paper No. 970793.
16. Miles, P., Megerle, M., Nagel, Z., Reitz, R.D., Lai, M.C.D., and Sick, V. (2003) "An experimental assessment of turbulence production, Reynolds stress and length scale (dissipation) modeling in a swirl-supported DI diesel engine," *SAE transactions*, 112 (3): pp. 1470-1499.
17. Reuss, D.L., Adrian, R.J., Landreth, C.C., French, D.T., and Fansler, T.D. (1989) "Instantaneous planar measurements of velocity and large-scale vorticity and strain rate in an engine using particle image velocimetry," SAE Paper No. 890616.
18. Reuss, D.L. (2000) "Cyclic variability of large-scale turbulent structures in directed and undirected IC engine flows," SAE Paper No. 2000-01-0246.
19. Li, Y., Zhao, H., Peng, Z., and Ladommatos, N. (2001) "Analysis of tumble and swirl motions in a four-valve SI engine," SAE Paper No. 2001-01-3555.
20. Funk, C., Sick, V., Reuss, D.L., and Dahm, W.J.A. (2002) "Turbulence properties of high- and low-swirl in-cylinder flows," SAE Paper No. 2002-01-2841.
21. Bevan, K.E., and Ghandhi, J.B. (2004) "PIV measurements of in-cylinder flow in a four-stroke utility engine and correlation with steady flow results," SAE Paper No. 2004-32-0005.
22. Ghandhi, J.B., Herold, R.E., Shakal, J.S., and Strand, T.E. (2005) "Time-resolved particle image velocimetry measurements in an internal combustion engine," SAE Paper No. 2005-01-3868.
23. Towers, D.P., and Towers, C.E. (2004) "Cyclic variability measurements of in-cylinder engine flows using high-speed particle image velocimetry," *Meas. Sci. Technol.*, 15, pp. 1917-1925.
24. Jarvis, S., Justham, T., Clarke, A., Garner, C.P., Hargrave, G.K., and Richardson, D. (2006) "Motored SI IC engine in-cylinder flow field measurement using time

resolved digital PIV for characterization of cyclic variation,” SAE Paper No. 2006-01-1044.

25. Jarvis, S., Justham, T., Clarke, A., Garner, C.P., Hargrave, G.K., and Halliwell, N.A. (2006) “Time resolved digital PIV measurements of flow field cyclic variation in an optical IC engine,” *J. Phys. Conf. Ser.*, 45, pp. 38-45.
26. Stansfield, P., Wigley, G., Justham, T., Catto, J., and Pitcher, G. (2007) “PIV analysis of in-cylinder flow structures over a range of realistic engine speeds,” *Exp. Fluids*, 43, pp. 135–146.
27. Calendini, P.O., Duverger, T., Lecerf, A., and Trinite, M. (2000) “In-cylinder velocity measurements with stereoscopic particle image velocimetry in a SI engine,” SAE Paper No. 2000-01-1798.
28. Koochesfahani, M. M., Cohn, R. K., Gendrich, C. P., and Nocera, D. G. (1996) “Molecular tagging diagnostics for the study of kinematics and mixing in liquid phase flows,” *Proceedings of the Eighth International Symposium on Applications of Laser Techniques to Fluids Mechanics, July 8 - 11, 1996, Lisbon, Portugal, vol. I, 1.2.1-1.2.12*; Also in *Developments in Laser Techniques and Fluid Mechanics*, Chapter 2, section 1, p. 125, Eds. Adrian, Durao, Durst, Maeda, and Whitelaw; Springer-Verlag, Berlin, 1997.
29. Gendrich, C.P., and Koochesfahani, M.M. (1996) “A spatial correlation technique for estimating velocity fields using molecular tagging velocimetry (MTV),” *Exp. Fluids*, 22 (1), pp 67-77.
30. Hill, R.B., and Klewicki, J.C. (1996) “Data reduction methods for flow tagging velocity measurements,” *Exp. Fluids*, 20, pp 142-152.
31. Sadr, R., and Klewicki, J.C. (2003) “A spline-based technique for estimating flow velocities using two-camera multi-line MTV,” *Exp. Fluids*, 35, pp 257-261.
32. Koochesfahani, M. M. (1999) “Molecular tagging velocimetry (MTV): Progress and applications” AIAA Paper No. AIAA-1999-3786.
33. Bohl, D.G., Koochesfahani, M.M., and Olson B.J. (2001) “Development of stereoscopic molecular tagging velocimetry,” *Exp. Fluids*, 30, pp 302-308.
34. Koochesfahani, M.M., and Nocera, D.G. (2001) “Molecular tagging velocimetry maps fluid flows,” *Laser Focus World*, 37 (6), pp. 103-108.
35. Gendrich, C. P., Koochesfahani, M. M., and Nocera, D. G. (1997) “Molecular tagging velocimetry and other novel applications of a new phosphorescent supramolecule,” *Exp. Fluids*, 23 (5), pp. 361-372.

36. Lempert, W.R., Magee, K., Ronney, P., Gee, K.R., and Haughland, R.P. (1995) "Flow tagging velocimetry in incompressible flow using photo-activated nonintrusive tracking of molecular motion (PHANTOMM)," *Exp. Fluids*, 18, 249-257.
37. Lum, C., Koochesfahani, M. M., and McGrath, J. J. (2001) "Measurements of the velocity field with MTV during the solidification of an alloy analog with mushy region," ASME/IMECE2001 Paper No. HTD-24222.
38. Koochesfahani, M.M., Cohn, R., and MacKinnon, C. (2000) "Simultaneous whole-field measurements of velocity and concentration fields using combined MTV and LIF," *Meas. Sci. Technol.*, 11 (9), pp. 1289- 1300.
39. Stier, B., and Koochesfahani, M.M. (1998) "Whole field MTV measurements in a steady flow rig model of an IC engine," SAE Paper No. 980481.
40. Goh, A. C. H. (2001) *Active flow control for maximizing performance of spark-ignited stratified charge engines*, MS thesis, Michigan State University, East Lansing, MI.
41. Koochesfahani, M. M., Goh, A. C., and Schock, H. J. (2004) "Molecular tagging velocimetry (MTV) and its automotive applications," In *The Aerodynamics of Heavy Vehicles: Trucks, Busses, and Trains*, Lecture Notes in Applied and Computational Mechanics, 19, pp. 143-155, Eds. McCallen, R., Browand, F., and Ross, J. (Springer-Verlag).
42. Schock, H.J., Shen, Y., Timm, E., Stuecken, T., Fedewa, A.M., and Keller, P. (2003) "The measurement and control of cyclic variations of flow in a piston cylinder assembly," SAE Paper No. 2003-01-1357.
43. Ismailov, M.M., Schock, H.J., and Fedewa, A.M. (2006) "Gaseous flow measurements in an internal combustion engine assembly using molecular tagging velocimetry," *Exp. Fluids*, 41, pp 57-65.
44. Luo, M., Chen, G., and Ma, Y. (2003) "Three-dimensional transient numerical simulation for intake process in the engine intake port-valve-cylinder system," *Journal of Zhejiang University - Science*, 4 (3), pp. 309-316.
45. Shojaeefard, M.H., and Noorpoor, A.R. (2008) "Flow simulation in engine cylinder with spring mesh," *American Journal of Applied Sciences*, 5 (10): pp. 1336-1343.
46. Shen, Y., Schock, H.J., and Oppenheim, A.K. (2002) "Dynamic stage of combustion in a direct injection methanol fueled engine," SAE Paper No. 2002-01-0998.
47. Shen, Y., Schock, H.J., and Oppenheim, A.K. (2003) "Pressure diagnostics of closed system in a direct injection spark ignition engine," SAE Paper No. 2003-01-0723.

48. Oppenheim, A.K. (2004) *Combustion in piston engines*, Springer, ISBN 3-540-20104-1.
49. Burgdorf, K., and Denbratt, I. (1997) "Comparison of cylinder pressure based knock detection methods," SAE Paper No. 972932.
50. Mittal, M., Zhu, G., Stuecken, T., and Schock H.J. (2009) "Effects of pre-injection on combustion characteristics of a single-cylinder diesel engine," ASME International Mechanical Engineering Congress and Exposition, Paper No. IMECE2009-10493.
51. Rassweiler, G.M., and Withrow, L. (1938) "Motion pictures of engine flames correlated with pressure cards," *SAE Transactions*, 42, pp 185-204.
52. Stone, C.R., and Green-Armytage, D.I. (1987) "Comparison of methods for the calculation of mass fraction burnt from engine pressure-time diagrams," *Proc. of IMechE*, Vol. 201, No. D1, pp 61-67.
53. Brunt, M.F.J., and Emtage, A.L. (1997) "Evaluation of burn rate routines and analysis errors," SAE Paper No. 970037.
54. Shayler, P.J., Wiseman, M.W., and Ma, T. (1990) "Improving the determination of mass fraction burnt," SAE Paper 900351.
55. Clarke, J.R., and Stein, R.A. (1999) "Internal combustion engine with variable camshaft timing, charge motion control valve, and variable air/fuel ratio," US patent, US: 5957096.
56. Stein, R.A., Galietti, K.M., and Leone, T.G. (1995) "Dual equal VCT - A variable camshaft timing strategy for improved fuel economy and emissions," SAE Paper 950975.
57. Li, Y., Liu, S., Shi, S., and Xu, Z. (2000) "Effect of the swirl control valve on the in-cylinder air motion in a four-valve SI engine," SAE Paper 2000-01-2058.
58. Kim, H., Yoon, S., Xie, X.B., Lai, M.C., Quelhas, S., Boyd, R., Kumar, N., and Moran, C. (2005) "Effects of injection timings and intake port flow control on the in-cylinder wetted fuel footprints during PFI engine startup process," SAE Paper 2005-01-2082.
59. Lee, D., and Heywood, J.B. (2006) "Effects of charge motion control during cold start of SI engines," SAE Paper 2006-01-3399.
60. Mittal, M., and Schock, H.J. (2009) "A study of cycle-to-cycle variations and the influence of charge motion control on in-cylinder flow in an IC engine," submitted to *Journal of Fluids Engineering*.

61. Koochesfahani, M.M., and Nocera, D.G. (2007) "Molecular tagging velocimetry," *Handbook of Experimental Fluid Dynamics*, chapter 5.4, Editors: J. Foss, C. Tropea and A. Yarin, Springer-Verlag.
62. <http://msds.chem.ox.ac.uk/BU/2,3-butanedione.html>
63. Stier, B., and Koochesfahani, M.M. (1999) "Molecular tagging velocimetry (MTV) measurements in gas phase flows," *Exp. Fluids*, 26, pp 297-304.
64. Sidebottom, H.W., Badcock, C.C., Calvert, J.G., Rabe, B.R., and Damon, E.K. (1972) "Lifetime studies of the biacetyl excited singlet and triplet states in the gas phase at 25°," *J. Am. Chem. Soc.*, 94, pp 13-19.
65. Zheng, Q., and Klewicki, J.C. (2000) "A fast data reduction algorithm for molecular tagging velocimetry: the decoupled spatial correlation technique," *Meas. Sci. Technol.* 11, pp 1282-1288.
66. Cohn, R. K., and Koochesfahani, M. M. (2000) "The accuracy of remapping irregularly spaced velocity data onto a regular grid and the computation of vorticity," *Exp. Fluids*, 29(7), S061- S069.
67. Miles, P., Megerle, M., Nagel, Z., Reitz, R.D., Lai, M.C.D., and Sick, V. (2003) "An experimental assessment of turbulence production, Reynolds stress and length scale (dissipation) modeling in a swirl-supported DI diesel engine," *SAE transactions*, 112 (3): 1470-1499.
68. Mittal, M., Schock, H.J., and Sadr, R. (2008) "Evaluating the influence of charge motion control on in-cylinder flow using MTV," ASME International Mechanical Engineering Congress and Exposition, Paper No. IMECE2008-66490.
69. Joo, S.H., Srinivasan, K.K., Lee, K.C., and Bell, S.R. (2004) "The behavior of small- and large-scale variations of in-cylinder flow during intake and compression strokes in a motored four-valve spark ignition engine," *Int. Journal of Engine Research*, 5 (4): pp. 317-328.
70. Raffel, M., Willert, C., and Kompenhans, J. (1998) *Particle image velocimetry: A practical guide*, Springer, ISBN – 3540636838.
71. Arroyo, M.P., and Greated, C.A. (1991) "Stereoscopic particle image velocimetry," *Meas. Sci. Technol.*, 2, pp. 1181-1186.
72. Bohl, D.G. (2002) *Experimental study of the 2-D and 3-D structure of a concentrated line vortex array*, PhD Thesis, Michigan State University, East Lansing, MI.
73. Spath, H. (1996) "Least-squares fitting by circles," *Computing*, 57: 179–185.

74. Soloff, S.M., Adrian, R.J., and Liu, Z.C. (1997) "Distortion compensation for generalized stereoscopic particle image velocimetry," *Meas. Sci. Technol.* 8, pp 1441-1454.
75. Naqwi, A. (2000) "Distortion compensation for PIV systems," Proc. 10th International Symposium on Applications of Laser Techniques to Fluid Mechanics, Lisbon, paper 6.2.
76. Mittal, M., Sadr, R., Schock, H.J., Fedewa, A., and Naqwi, A. (2009) "In-cylinder engine flow measurement using stereoscopic molecular tagging velocimetry (SMTV)," *Exp. Fluids*, 46 (2), 277-284.
77. Sadr, R., Mittal, M., and Schock, H.J. (2008) "In-cylinder IC engine velocity measurements using stereoscopic molecular tagging velocimetry," 61st Annual Meeting of American Physical Society, Division of Fluid Dynamics, San Antonio, Texas.
78. Benedict, L.H., and Gould, R.D. (1996) "Towards better uncertainty estimates for turbulence statistics," *Exp. Fluids*, 22, pp. 129–136.
79. Zhang, L., Takahiro, U., Toshiaki, T., and Katsuhiko, Y. (1995) "A study of the cycle-to-cycle variation of in-cylinder flow in a motored engine through digital image processing of visualized images," SAE Paper 950727.
80. Parsi, M., and Daneshyar, H. (1989) "A study of cyclic variations in gas velocities in an engine cylinder," SAE Paper 892100.
81. Mittal, M., Zhu, G., Schock, H.J., Stuecken, T., and Hung, D.L.S. (2008) "Burn rate analysis of an ethanol-gasoline, dual fueled, spark ignition engine," ASME International Mechanical Engineering Congress and Exposition, Paper No. IMECE2008-66139.
82. Nakata, K., Utsumi, S., Ota, A., Kawatake, K., Kawai, T., and Tsunooka, T. (2006) "The effect of ethanol fuel on a spark ignition engine," SAE Paper 2006-01-3380.
83. Brinkman, N.D. (1981) "Ethanol Fuel – A single-cylinder study of efficiency and exhaust emissions," SAE Paper 810345.
84. Srivastava, S., Schock, H.J., Jaber, F., and Hung, D.L.S. (2009) "Numerical simulation of a direct-injection spark-ignition engine with different fuels," SAE paper 2009-01-0325.
85. Starkman, E.S., Newhall, H.K., and Sutton, R.D. (1964) "Comparative performance of alcohol and hydrocarbon fuels," SAE Paper 640649.

86. Salih, F.M., and Andrews, G.E. (1992) "The influence of gasoline/ethanol blends on emissions and fuel economy," SAE Paper 922378.
87. Bromberg, L., Cohn, D.R., and Heywood, J.B. (2006) "Optimized fuel management system for direct injection ethanol enhancement of gasoline engines," US patent, US: 26102136.
88. Bitar, E.Y., Oppenheim, A.K., and Schock, H.J. (2006) "Model for control of combustion in a piston engine," SAE Paper 2006-01-0401.
89. Mittal, M., Zhu, G., and Schock, H.J. (2008) "Fast mass fraction burned calculation using net pressure method for real-time applications," *Proc. IMechE, Part D: J. Automobile Engineering*, 2009, 223 (3), 389-394.
90. Zhu, G., Daniels, C.F., and Winkelman, J. (2003) "MBT timing detection and its closed-loop control using in-cylinder pressure signal," SAE Paper 2003-01-3266.

MICHIGAN STATE UNIVERSITY LIBRARIES



3 1293 03063 2289